

Characterization and Development of  
Submillimeter Wavelength Devices  
Incorporating Vanadium Dioxide Thin Films

---

A Dissertation

Presented to  
the faculty of the School of Engineering and Applied Science  
University of Virginia

---

in partial fulfillment  
of the requirements for the degree

Doctor of Philosophy

by

Rebecca Percy

December

2013

# APPROVAL SHEET

The dissertation  
is submitted in partial fulfillment of the requirements for the degree of  
Doctor of Philosophy

  
AUTHOR

The dissertation has been read and approved by the examining committee:

Robert M. Weikle, II

Advisor

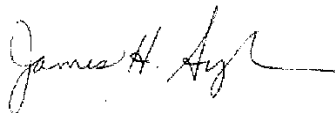
Arthur Lichtenberger

James Fitz-Gerald

Jiwei Lu

Mircea Stan

Accepted for the School of Engineering and Applied Science:



Dean, School of Engineering and Applied Science

December  
2013

## Abstract

Vanadium dioxide exhibits an insulator-to-metal transition (IMT) accompanied by a decrease in resistivity of several magnitudes and a large increase in reflectivity. The IMT can be triggered in multiple ways. The most common method is to heat a sample above 67°C causing it to go from a semiconducting to metallic phase. However, the transition can also be triggered using current injection, a change in electric field, or an optical pump. A diverse array of potential applications exploiting VO<sub>2</sub> including next generation CMOS, switches, thermal relays, intelligent window coatings, bolometers, filters, memory and logic devices, and reconfigurable circuit elements and antennas from dc to x-ray wavelengths have been proposed in the literature.

A better understanding of vanadium dioxide thin films and their properties is needed to develop new devices and technologies based on the material. One such property is the contact resistance. As devices become smaller, the contact interface will account for an increasing portion of the device function and have noticeable effect on its performance. The standard method for determining the contact resistance of planar metal-semiconductor interfaces involves measuring adjacent pairs of contacts with various separation lengths at a constant bias. This method relies on the resistivity of the semiconductor material remaining constant during measurement. However, the strong temperature dependence of the resistivity of VO<sub>2</sub> requires a modified approach that maintains a constant power density dissipated within the film to account for Joule heating. A new method for measuring contact resistance in semiconductors with a high thermal coefficient of resistivity is presented and results using this new method are compared with results using the standard technique.

As new device concepts are proposed and developed, VO<sub>2</sub> films are exposed to many standard chemicals used for semiconductor device processing, including etchants, organic solvents, and other reagents such as acetone, O<sub>2</sub> plasma, de-ionized water, and photolithography process. During fabrication of devices for this dissertation, physical changes to the appearance of VO<sub>2</sub> films were observed. It was hypothesized that some of the chemicals and processes used during device fabrication were etching or otherwise altering the VO<sub>2</sub> films. Changes in thickness,

stoichiometry, resistivity, and appearance of a VO<sub>2</sub> thin film as a result of several common reagents and photolithography were systematically investigated and the results are presented.

The recent development of on-wafer terahertz measurement systems permits direct in-situ characterization of planar devices at frequencies approaching 1 THz. Such measurements are critical for assessing new and emerging device technologies for high-frequency applications, including those based on vanadium oxide, and allow accurate circuit models to be derived for use in circuit design. Vanadium oxide switches are of interest for their potential use in realizing reconfigurable circuits at these frequencies.

A single element (one port) device consisting of a thin film VO<sub>2</sub> load at the terminus of a coplanar waveguide (CPW) transmission line and a two port switch consisting of two CPW transmission lines connected in series with a VO<sub>2</sub> load were designed and characterized in the WR-1.5 waveguide band (500-750 GHz). These results demonstrate that the voltage-induced IMT modulates reflection or transmission of a signal by about 10 dB. The metallic state impedance of the VO<sub>2</sub> film was calculated from the data obtained and shown to be primarily resistive making VO<sub>2</sub> attractive for broadband applications.



## Acknowledgements

I would like to thank my advisor, Bobby Weikle, for all of his assistance, teachings, guidance, and encouragement on this journey. I give thanks to my committee members, Prof. Art Lichtenberger, Jiwei Li, Mircea Stan, and Jim Fitz-gerald for their insight and advice along with Prof. Stu Wolf for sharing his ideas and guidance.

Thank you Salinporn (Lin) Kittiwatanakul for providing the VO<sub>2</sub> film and helping with the materials science diagnostics, Matt Bauwens for his help with the on-wafer terahertz measurements, and Lei Liu for getting me started on my own research while he was finishing his PhD.

Acknowledgement also goes to all my group mates, past and present, in the FIR lab for their valuable discussions and assistance throughout my research and those in UVML who taught me and assisted me with the processes and procedures necessary used in this research. I extend my gratitude to the FIR lab manager, Dr. Acar Isin, for his help with the experimental setups and earlier on with cryogenics and to those who work in UVML, Joe Beatrice, Alex Lobo, Harry Wade, Jian Zhang, and Jie Wang.

To my family and friends, I thank you for all of your support and encouragement.

And as always, I thank my parents for believing in me.

# Table of Contents

Chapter 1: Introduction.....	1
1.1 Goals of this research.....	1
1.2 Dissertation overview .....	3
Chapter 2: Background .....	5
2.1 Vanadium Oxide Species.....	10
2.2 VO <sub>2</sub> Growth .....	10
2.3 Microwave VO <sub>2</sub> Switches.....	12
2.4 Quasioptical Terahertz Switches Utilizing the VO <sub>2</sub> IMT .....	13
Chapter 3: The Effects of Common Fabrication Processes and Reagents on VO <sub>2</sub> Thin Film .	19
3.1 Experimental Procedure.....	19
3.1.1 VO <sub>2</sub> Film Preparation .....	20
3.1.2 Fabrication Processes Considered in this Study .....	20
3.1.3 Diagnostic Tools .....	21
3.2 Process and Solutions Descriptions .....	22
3.2.1 Dicing Saw .....	23
3.2.2 Acetone .....	24
3.2.3 O <sub>2</sub> Plasma Clean .....	25
3.2.4 Deionized Water .....	29
3.2.5 Increased Temperature in Ambient Conditions .....	30
3.2.6 NMP and Propylene-Glycol Solution .....	32
3.2.7 N-Methyl-2-pyrrolidone (NMP) .....	33
3.2.8 Photolithography .....	34
3.3 Results Summary by Analysis Technique .....	35

3.3.1 Visual Results Summary .....	36
3.3.2 Resistance Measurements .....	37
3.3.3 VO <sub>2</sub> Film Thickness .....	39
3.3.4 XRD .....	39
3.4 Conclusions .....	40
Chapter 4: Characterization of Contact Resistance for Gold-VO <sub>2</sub> Thin Film Interfaces .....	43
4.1 Introduction .....	43
4.1.1 Common Method for Measuring Contact Resistance .....	44
4.1.2 Application to Vanadium Dioxide .....	47
4.2 VO <sub>2</sub> Film, Device Fabrication, and Measurement Procedure .....	48
4.2.1 Vanadium Dioxide Thin Film Deposition .....	48
4.2.2 Fabrication of Contact Resistance Test Structures .....	49
4.2.3 Pad Geometry and Characterization .....	50
4.2.4 DC Measurement System .....	50
4.3 Development of a Modified Method for Measuring Contact Resistance .....	52
4.3.1 Standard Method .....	52
4.3.2 Constant Power Density Method .....	54
4.3.3 Incorporation of the Transfer Length .....	57
4.3.4 Effective Volume Method .....	60
4.4 Contact Resistance Measurement Results .....	62
4.4.1 Resistivity as a function of power density .....	64
4.4.2 Contact Resistance as a Function of External Temperature .....	69
4.5 Conclusions .....	71
Chapter 5: Characterization of VO <sub>2</sub> Switching Elements at Submillimeter Wavelengths .....	73
5.1 Microwave Frequency Measurements .....	74

5.2 VO <sub>2</sub> Device Fabrication and Experimental Setup for Submillimeter On-Wafer Measurements .....	76
5.2.1 Fabrication Approach.....	76
5.3 One Port Device with VO <sub>2</sub> Load in Semiconducting and Metallic States.....	78
5.3.1 Design of a CPW Terminated with a VO <sub>2</sub> Load.....	78
5.3.2 Calibration for One-Port Measurements .....	80
5.3.3 One-port Measurement Results.....	82
5.3.4 Uniformity of Return Loss for Multiple Devices on a Single Wafer .....	87
5.3.5 Repeatability Characterization of a Single Device .....	89
5.3.6 Broadband Potential.....	92
5.3.7 Summary of One-Port Device Results .....	94
5.4 Two Port VO <sub>2</sub> On-Wafer Switch .....	95
5.4.1 Insertion Loss in the VO <sub>2</sub> Semiconducting and Metallic State.....	96
5.4.2 Repeatability of a Single Device over Multiple Switching Events.....	98
5.4.3 Calibration.....	100
5.5 Conclusion/summary .....	101
Chapter 6: Conclusion and Future Work .....	103
6.1 Review of Research Objectives .....	103
6.2 Accomplishments.....	104
6.3 Future Research .....	105
6.3.1 Reduce Contact Resistivity .....	105
6.3.2 Passivation Layer for VO <sub>2</sub> Thin Film .....	105
6.3.3 VO <sub>2</sub> Modulated Bowtie Antenna Array.....	106
6.4 Future Research Summary .....	109
Appendix A: Permanent Damage to VO <sub>2</sub> Devices.....	A-1

Appendix B:	MatLab Code for Calculating Contact Resistance .....	B-9
Appendix C:	Fabrication Recipe.....	C-19

## Table of Figures

Figure 2.1: The change in (a) resistivity and (b) terahertz transmission of a VO <sub>2</sub> thin film with increasing and decreasing temperature [6]. .....	5
Figure 2.2: Conductivity of VO <sub>2</sub> in addition to several other vanadium oxide species as a function of inverse temperature from the first published results showing the IMT for VO <sub>2</sub> [1]. ...	6
Figure 2.3: Lattice structures for VO <sub>2</sub> . (a) Monoclinic lattice seen below T <sub>c</sub> and (b) tetragonal lattice seen above the thermal transition temperature. ....	7
Figure 2.4: The (a) voltage induced and (b) current induced change in resistivity [4]. ....	7
Figure 2.5: Results from Zimmers et al. showing that the voltage induced transition is caused by Joule heating. (a) The particle-measured temperature as a function of increasing voltage bias. The shaded region indicates the transition temperature as determined using a traditional resistivity-temperature measurement. T <sub>set</sub> is the temperature from an external Peltier heater. (b) The resistance as a function of particle-measured temperature when the VO <sub>2</sub> is transitioned using an external temperature (equilibrium R(T)) and Joule heating (non-equilibrium R(T)) [12]. ....	8
Figure 2.6: The change in transmission of a VO <sub>2</sub> film at 800nm for five different doses of incident radiation [15]. ....	9
Figure 2.7: Typical characterization data for a VO <sub>2</sub> thin film used in this research. (a) Resistance-temperature measurement, (b) XRD result, and (c, d) AFM data. [Courtesy: Salinporn Kittiwatanakul] .....	11
Figure 2.8: The transmission of a series, CPW driven VO <sub>2</sub> switch in the metallic and semiconducting states when the IMT is induced using (a) external heating [23] and (b) a voltage bias [24]. ....	12
Figure 2.9: The VO <sub>2</sub> SRR device and results. (a) A sketch of the SRR gap overlaid on an sSNIM image taken at 342K. The green areas are metallic state VO <sub>2</sub> grains and the blue areas are	

semiconducting state  $\text{VO}_2$ . (b) The SRR device layout. (c) A single SRR device with the simulated electric field superimposed. (d) The transmission spectra of the hybrid SRR shows the decrease in resonance frequency with increasing temperature. (e) The center resonance frequency remains constant until metallic regions percolate in the  $\text{VO}_2$ . When the  $\text{VO}_2$  becomes metallic, no resonance is seen [26]. ..... 13

Figure 2.10: The transmission of the  $\text{VO}_2$  switched nano antennas when the  $\text{VO}_2$  is in the semiconducting (0, 350, 0V) and the metallic (500V) states [27]. ..... 14

Figure 3.1: Photograph of the dc probe test setup. The inset shows a close-up photograph of the tips themselves. .... 22

Figure 3.2: Voltage-current measurement at multiple locations on two different dicing saw samples. The solid line represents the linear regression results to the dataset, the slope of which is used to calculate the average resistance across the wafer. This dataset is used as the control set. .... 24

Figure 3.3: Voltage-current measurement at multiple locations across the acetone-exposed sample. The solid line represents the linear regression results to the dataset, the slope of which is used to calculate the average resistance across the wafer. (a) Using the same plot scale as the other plots in this chapter to provide a quick relative comparison of the slopes and (b) using a smaller y-axis scale. .... 25

Figure 3.4: A March PX50 plasma cleaning system [Courtesy: <http://kmf.pa.msu.edu/KMF/Equipment/equip11.asp>] ..... 26

Figure 3.5: Voltage-current measurement at multiple locations across the  $\text{O}_2$  plasma-exposed sample. The solid line represents the linear regression results to the dataset, the slope of which is used to calculate the average resistance across the wafer. .... 27

Figure 3.6: XRR data comparing a control sample with the sample exposed to  $\text{O}_2$  plasma. .... 28

Figure 3.7: Voltage-current measurements at multiple locations across the (a) 80 degree and (b) room temperature DI water exposed samples. The solid line represents the linear regression

results to the dataset, the slope of which is used to calculate the average resistance across the wafer. .... 30

Figure 3.8: Voltage-current measurement at multiple locations across the sample heated to (a) 110°C and (b) 160°C. The solid line represents the linear regression results to the dataset, the slope of which is used to calculate the average resistance across the wafer..... 31

Figure 3.9: The EDX results for the area (a) under the gold contact pad and (b) between the pads. A vanadium peak around 5 eV is seen underneath the pads but is missing in the area between the pads. The Au that appears in (b) is from overlap onto the pads and the O is from the  $\text{AlO}_2$  substrate. This indicates that the  $\text{VO}_2$  bridge has been removed after the gold was deposited. The inset shows approximately where each EDX measurement was performed. .... 32

Figure 3.10: Voltage-current measurement at multiple locations across the sample exposed to NMP and propylene-glycol mixture. The solid line represents the linear regression results to the dataset, the slope of which is used to calculate the average resistance across the wafer..... 33

Figure 3.11: Voltage-current measurement at multiple locations across the sample exposed to NMP. The solid line represents the linear regression results to the dataset, the slope of which is used to calculate the average resistance across the wafer..... 34

Figure 3.12: Voltage-current measurement at multiple locations across the sample exposed to nLOF2020 photolithography process. The solid line represents the linear regression results to the dataset, the slope of which is used to calculate the average resistance across the wafer..... 35

Figure 3.13: (a) An optical photograph of the samples. (b) The average color for each sample. The color swatches are placed in the corresponding location from (a). The labels indicate the process or reagent to which a given sample was exposed. .... 37

Figure 3.14: The mean and standard deviation of five current measurements across each sample. Each line indicates a different sample. The heavy, black, dashed line indicates the measurements made prior to dicing the wafer and performing the experiment. .... 38



- Figure 3.15: The thickness of each sample after exposure. The solid and dashed lines show the mean and one standard deviation of the mean for the control/dicing samples. The red square atop the O<sub>2</sub> plasma sample shows the vanadium oxide film grown from the VO<sub>2</sub> film. .... 39
- Figure 3.16: XRD for the VO<sub>2</sub> samples that exhibited a visual change. “Original” is the data taken directly after the film growth. [Courtesy: Salinporn Kittiwatanakul] ..... 40
- Figure 4.1: The contact measurement geometry. (a) A top view image shows a series of gold contact pads with varying spacing. (b) An oblique view sketch of a single contact gap. .... 44
- Figure 4.2: The measured resistance between adjacent contact pads is plotted as a function of the length between the pads and a line is fit to the data. .... 45
- Figure 4.3 A circuit model corresponding to the geometry in Figure 4.2b.  $R_i$  is the interfacial resistance,  $R_k$  is the resistance of the VO<sub>2</sub> under the contact, and  $R_{VO2}$  is the resistance between the contacts.  $R_c$  is the series combination of  $R_i$  and  $R_k$ . .... 46
- Figure 4.4: (a) Resistivity-temperature plot and (b) XRD of the VO<sub>2</sub> film. [Courtesy: Salinporn Kittiwatanakul] ..... 48
- Figure 4.5: (a) An optical image of a contact resistance measurement device. The six pads are separated by increasing lengths. The VO<sub>2</sub> extends past the ends of the device by 50  $\mu\text{m}$  on each side and is flush on the top and bottom of the contacts. (b) An SEM of two contact pads and the gap between them. The slightly oblique shape is an artifact of the SEM and not real. (c) A higher magnification of the gap used to inspect the quality of the contact pad edges. .... 49
- Figure 4.6: Measurement of the gap length using the pixel intensity along a drawn line on an SEM image to determine the edge of the contact pad. .... 50
- Figure 4.7: A sample contact resistance measurements dataset. The black, diagonal, dashed line connects the transition points for each gap length. .... 51
- Figure 4.8: (a) The raw IV data with superimposed lines of constant current. (b) A resistance-length plot from the constant current with points of interest highlighted. At least fifty different

current values are used for the calculations but only five are plotted for clarity. (c) The contact resistance and sheet resistance as calculated using the constant current method. .... 53

Figure 4.9: Midinfrared near field image showing the percolation of metallic regions with increasing temperature. The 341K image in the upper left is mostly in the insulating state (blue) while the 343.6K image in the lower right is mostly in the metallic state (green) [12]. .... 54

Figure 4.10: (a) The IV data with several superimposed lines of constant dissipated power density as calculated for the volume between the contact pads. (b) A resistance-length plot using the data from (a). At least fifty different power densities are used for the calculations but only five are plotted for clarity. (c) The contact resistance and sheet resistance. .... 56

Figure 4.11: (a) A diagram illustrating the definition of the end resistance. (b) A diagram showing the three measurements needed to calculate the end resistance [4]. .... 58

Figure 4.12: (a) The raw IV data with several superimposed lines of constant dissipated power density as calculated using the volume between the contacts and the volume under the contacts and within the transfer length. (b) A resistance-length plot using the data from (a). At least fifty different power densities are used for the calculations but only five are plotted for clarity. (c) The contact resistance and sheet resistance. .... 60

Figure 4.13: A sketch illustrating “effective  $x$ ”.  $L_n$  is the gap length,  $R_{sh}$  is the sheet resistance of the  $VO_2$  between the contacts, and  $R_c$  is the contact resistance, which includes the resistance of the  $VO_2$  under the pad (which is different from  $R_{sh}$ ) and the interfacial resistance. .... 60

Figure 4.14: A diagram showing the process used to determine the effective length,  $x$ . (1) An array of  $x$ -values is stepped through. (2) The resistance-length data for a given  $x$  value is extracted from the raw data using the modified dissipated power density. (3) A linear fit to the R-L data is performed for each power density. (4) The range of the y-intercepts in (3) is calculated. After the range of intercepts for each  $x$  value has been calculated, the value with the smallest range of resistance axis intercepts is chosen as the “best” ..... 61

Figure 4.15: (a) The raw IV data with several superimposed lines of constant dissipated power density as calculated using the volume between the contacts and the volume under the contacts

and within the calculated “effective  $x$ ” value. (b) A resistance-length plot using the data from (a). At least fifty different power densities are used for the calculations but only five are plotted for clarity. (c) The resulting contact resistance and sheet resistance. (d) The mean y-intercept and one standard deviation plotted for each “effective  $x$ ” value. .... 64

Figure 4.16: The resistivity of the  $\text{VO}_2$  between the contact pads for each gap length (a) versus current without contact resistance removed, (b) versus current with the contact resistance removed, (c) versus power density without contact resistance removed, and (d) versus power density with contact resistance removed..... 67

Figure 4.17: The (a) sheet resistance, (b) specific contact resistivity, and (c) effective volume at 26 °C, 43 °C, 55 °C, and 65 °C. The specific contact resistivity error is based on the range of y-intercept values. The sheet resistance is based on the best fit equation for the sheet resistance as a function of power density when power density is extrapolated to 0 (the y-intercept of the best fit line). .... 70

Figure 5.1: (a) A photograph of the DUT indicating the probe location. (b) A higher magnification photo showing geometry of the  $\text{VO}_2$  in a similar device..... 74

Figure 5.2: A Smith Chart showing measured and simulated return loss from 0.050 to 20 GHz. 75

Figure 5.3: The equivalent circuit model for the Hall Bar structure. The transmission line represents the gold lines between the probe and the  $\text{VO}_2$ . The  $\text{VO}_2$  results are given for the semiconducting (0 mA) and metallic (14 mA) states. .... 75

Figure 5.4: The equivalent circuit model results for the microwave device after the transmission line portion has been removed. Notice that both the semiconductor and metallic state regions lie on lines of constant conductance. .... 76

Figure 5.5: (a) A photograph of the THz probe state in one-port configuration. (b) A photograph of the WR-1.5 probe contacting the DUT..... 78

Figure 5.6: A sketch of the structure of CPW. The center conductor has a width,  $w$ , and center conductor to ground distance,  $s$ . The direction of wave propagation is into or out of the page. .. 79

Figure 5.7: An (a) optical image and a (b) SEM image of a one-port, CPW fed, VO<sub>2</sub> device. .... 80

Figure 5.8: The calibration standards as re-measured after calibration. (a) A Smith Chart representation shows that some measurements lie outside the  $\Gamma = 1$  circle. (b) A magnitude plot shows that the open and parts of the short have return loss greater than 0dB. .... 81

Figure 5.9: The open calibration standard re-measured twice after calibration. .... 82

Figure 5.10: Electrically inducted IMT transition for the DUT. After the VO<sub>2</sub> undergoes the IMT, the SMU is limited by its compliance at 10 mA. The inset shows the semiconducting portion of the data with the linear regression used to find the mean dc resistance. .... 83

Figure 5.11: The results for a typical one-port VO<sub>2</sub> switch in the semiconducting and metallic state. (a) A Smith chart representation of the data. (b) The magnitude and (c) phase in the semiconducting and metallic states. .... 85

Figure 5.12: The resistance and reactance of the VO<sub>2</sub> film in the metallic state. .... 86

Figure 5.13: The results for five different one-port VO<sub>2</sub> switches on a single wafer. (a) A Smith chart representation of the data. (b) The magnitude and (c) phase in the semiconducting and metallic states. .... 88

Figure 5.14: The results for nine back-to-back sweeps on a single device. (a) A Smith chart representation of the data. (b) The magnitude and (c) phase of the reflection in the semiconducting and metallic states. The sweep order starts at green (grayscale lightest) through red then black (grayscale darkest). .... 90

Figure 5.15: The bias voltage and resulting dc current for nine consecutive sweeps. The arrows indicate increasing or decreasing voltage and the hysteretic nature of the VO<sub>2</sub>. The voltage step size was 2V so there are likely smaller changes in critical voltage between sweeps. The final sweep (black) had a much larger hysteresis. .... 91

Figure 5.16: SEM image of two different devices that were (a) permanently damaged and (b) destroyed during measurements. The device in (a) shows the damage similar to that expected

after the ninth sweep and (b) shows the destruction of a device similar to that caused by the tenth sweep..... 92

Figure 5.17: The average change in phase with the mean (red solid line) and standard deviation (red dashed line) indicated. .... 93

Figure 5.18: HFSS simulation structure. Note that there is no VO<sub>2</sub> present in this simulation.... 93

Figure 5.19: The phase of the VO<sub>2</sub> device in the semiconducting state (blue solid) and the phase of the simulated structure without the VO<sub>2</sub> film (red dashed). .... 94

Figure 5.20: Optical images of the two-port device configurations. (a) The smaller device, design “C”. (b) The large device, design “E” ..... 95

Figure 5.21: The “on” (metallic) and “off” (semiconducting) transmission for the “C” and “E” design two-port switches. (a) A Smith chart representation of the data. (b) The magnitude and (c) phase of each design in each state..... 97

Figure 5.22: A single design “C” device switched measured nine times. (a) A Smith chart representation of the data. (b) The magnitude and (c) phase in each state. .... 99

Figure 5.23: The thru and line calibration standards as measured after calibration. (a) The Smith Chart representation of the data shows that the magnitude of the transmission sometimes exceeds one indicating error in the calibration. (b) The magnitude of the thru and line transmission is  $\pm 2$  dB. Ideally, these measurements should be 0 dB..... 101

Figure 6.1: A VO<sub>2</sub> – bowtie antenna array. (a) A 20x20  $\mu\text{m}$  array showing the large gold contact pads on either side. (b) A higher magnification view of a portion of the array showing the bowties antennas and how they are connected. The dashed line square shows a defect in the mask. The solid line square indicates a single bowtie antenna. (c) A higher magnification image of a single bowtie and VO<sub>2</sub> feed. (d) A single antenna and feed for testing the bowties. The four pads are for four point probe measurements. .... 107

Figure 6.2: An Ansoft HFSS simulation of the transmission of the bowtie antenna array when the VO<sub>2</sub> is in the semiconducting (red solid) and metallic (blue dashes) states. .... 107

Figure 6.3: Experimental setup for measuring the VO<sub>2</sub> – bowtie antenna array. The incident signal will be generated at port 1, focused onto the array and either reflected or transmitted depending on the state of the VO<sub>2</sub>. The transmitted signal will be detected at port 2. The VO<sub>2</sub> IMT will be induced by a heat lamp or an optical laser signal. .... 109

Figure A.1: Permanent filament formation in a VO<sub>2</sub> film. (a) the region before measurements and (b) the same region after measurement. ....A-1

Figure A.2: (a) Post-measurement SEM showing permanent and destructive filament formation. (b) The corresponding IV measurement. The further past transition bias a given separation distance is measured, the more destruction to the material. The 4.67  $\mu\text{m}$  device had a visible contact edge irregularity and was discounted from the measurements. ....A-2

Figure A.3: Damage to VO<sub>2</sub> films during measurement – post-mortem SEM images. (a) The VO<sub>2</sub> film appears rippled and like it may be starting to delaminate from the film. (b) Destruction of the VO<sub>2</sub> film and the gold at the contact pad edges. ....A-4

Figure A.4: Another type of damage to the VO<sub>2</sub>. (a) An optical microstrip showing a dark brown stripe parallel to the contact pad. (b) An optical profilometer indicating changes in height (or index of refraction) on the VO<sub>2</sub> surface. (c) In-lens and (d) SE2 SEM images showing what appears to be VO<sub>2</sub> peeling and curling. ....A-4

Figure A.5: (a) A low magnification version of a completely destroyed device. For scale, each contact pad is 500 x 500  $\mu\text{m}$ . (b) The film morphology and gold droplets after the destruction of the device. The white lines indicate the edges of the contact pad. On the far right, the contact pad can be seen with some damage. Moving toward the left, some VO<sub>2</sub> appears fractures then there is a region that may or may not still contain VO<sub>2</sub>. Finally on the far left, condensed droplets can be seen where the edge of the contact pad should be located..... A-6

Figure A.6: Destruction caused by a fabrication flaw, in this case a chipped off piece of gold on the edge of the contact pad..... A-7

Figure A.7: Training a VO<sub>2</sub> device. A device was swept 25 times in a row without lifting the probes or changing the sweep parameters using (a) a pulsed linear stair current source and (b) a continuous linear stair current source. It can be seen that both devices changed after the first sweep. In the case of (a), it only took one sweep to train the device while (b) took about 10 sweeps and was still inconsistent after 25..... A-8

## Table of Tables

Table 3.1: The thickness, resistance, and appearance of each sample after exposure.....	36
Table 5.1: The average magnitude and phase of five devices in the semiconducting and metallic state. ....	87
Table 5.2: The magnitude and phase in the semiconducting and metallic state for nine sweeps of the same devices. ....	89

## Chapter 1: Introduction

Vanadium dioxide ( $\text{VO}_2$ ) experiences an abrupt insulator-to-metal transition (IMT) accompanied by a large change in resistivity and reflectivity. The most common method for initiating this transition is through an increase in temperature above about  $67^\circ\text{C}$ ; however, the  $\text{VO}_2$  IMT can also be triggered electrically via current injection or optically via photoinduction. The large change in resistivity and reflectivity accompanying all three transition methods make  $\text{VO}_2$  an appealing material for a diverse array of applications from dc to x-ray frequencies. Applications include next generation CMOS technology [1], optical switches [2], thermistors [2], thermal relays [2], variable reflectivity mirrors [2], bolometers [3], modulators [4], variable filters [4], field-effect transistors [5], memory and logic devices [1], intelligent window coatings [6], and reconfigurable circuit elements or antennas [7].

### 1.1 Goals of this research

The ultimate goal of this research is the development and demonstration of an on-wafer terahertz switch. The recent development of on-wafer terahertz measurement systems permits direct, in-situ characterization of planar devices up to a frequency of 1.1 THz. Such measurements are critical for assessing new and emerging device technologies for high-frequency applications, including those based on  $\text{VO}_2$ , and they allow accurate circuit models to be derived for use in circuit design. Vanadium oxide switches are of interest as very broadband devices and for potential use in realizing reconfigurable circuits at THz frequencies. Moreover,  $\text{VO}_2$  could be used for designing tunable circuit elements such as matching networks and filters. The large current- or voltage- induced change in resistivity associated with  $\text{VO}_2$  makes it appealing for such applications.

While developing this device, many observations were made regarding behavior of the vanadium dioxide thin films in different situations. Two such observations were changes to the



VO<sub>2</sub> film while fabricating the devices and the inadequacy of the standard contact resistance measurement method.

During fabrication of devices for this dissertation, unexpected changes to the VO<sub>2</sub> films were observed. It was hypothesized that some of the chemicals and processes used during device fabrication were etching or otherwise altering the VO<sub>2</sub> films. During processing the films are exposed to some common chemicals and processes include propylene glycol, deionized water, acetone, and photolithography. As new device concepts are proposed and developed, VO<sub>2</sub> films will be exposed to many standard chemicals used for semiconductor device processing, including etchants, organic solvents, and other reagents. The effects of these reagents and several others used when making terahertz switches were investigated and the results are presented.

Contact resistance plays a major role when designing a semiconductor device. As devices become smaller, the contact interface accounts for an increasing portion of the device function [8] and have noticeable effect on its performance. Methods for measuring and quantifying the resistance between a metallic contact and semiconductor were developed in the 1960's to characterize these interfaces and are necessary for understanding and potentially reducing the contribution of the interface to device resistance. A widely-used method of determining contact resistance between a metallic contact pad and a semiconductor material is the transmission-line model (tln) [9]. When using this method, it was seen that the contact resistance was a function of the bias current and that the resistivity of the VO<sub>2</sub> was dependent on the length of the device. It was suspected that these observed trends were caused by resistive heating within the VO<sub>2</sub> film. In the past, modifications to the common tln method have been made to address observations seen in measurements such as including the resistance of the contact pad in the model [10] and allowing for the sheet resistance of the semiconductor to be different beneath the contacts than between the contacts [11]. In this research, the common contact resistance measurement method is modified to address materials with high thermal coefficients of resistance (TCR), such as VO<sub>2</sub>.

## 1.2 Dissertation overview

Chapter 2 presents background information regarding vanadium dioxide films that is useful in understanding the research presented in this dissertation. Chapter 3 describes the effects of several chemicals and processes used when fabricating devices. Chapter 4 develops a new method for measuring the contact resistance in films with high thermal coefficients of resistance. A VO<sub>2</sub> based variable load and a VO<sub>2</sub> based two port switch at WR-1.5 are presented in chapter 5. Several conclusions and a few ideas for future works are summarized in chapter 6. Appendix A shows several devices that were permanently altered or destroyed during measurement and appendices B provides the MatLab code used to calculate contact resistance. Appendix C provides the fabrication recipe for the devices fabricated during this research.

- [1] K. West, J. Lu, J. Yu, D. Kirkwood, W. Chen, Y. Pei, J. Claassen, and S. A. Wolf, "Growth and characterization of vanadium dioxide thin films prepared by reactive-biased target ion beam deposition," *Journal of Vacuum Science Technology A: Vacuum, Surfaces, and Films*, vol. 26, no. 1, pp. 133–139, 2008.
- [2] H. Jerominek, D. Vincent, and F. Picard, "Vanadium oxide films for optical switching and detection," *Optical Engineering*, vol. 32, no. 9, pp. 2092–2099, 1993.
- [3] L. A. L. de Almeida, G. S. Deep, A. M. N. Lima, I. A. Khrebtov, V. G. Malyarov, and H. Neff, "Modeling and performance of vanadium–oxide transition edge microbolometers," *Applied Physics Letters*, vol. 85, no. 16, pp. 3605–3607, 2004.
- [4] J. C. C. Fan, H. R. Fetterman, F. J. Bachner, P. M. Zavracky, and C. D. Parker, "Thin-film VO<sub>2</sub> submillimeter-wave modulators and polarizers," *Applied Physics Letters*, vol. 31, no. 1, pp. 11–13, 1977.
- [5] S. Sengupta, K. Wang, K. Liu, A. K. Bhat, S. Dhara, J. Wu, and M. M. Deshmukh, "Field-effect modulation of conductance in VO<sub>2</sub> nanobeam transistors with HfO<sub>2</sub> as the gate dielectric," *Applied Physics Letters*, vol. 99, no. 6, p. 062114, 2011.

- [6] T. D. Manning, I. P. Parkin, R. J. H. Clark, D. Sheel, M. E. Pemble, and D. Vernadou, "Intelligent window coatings: atmospheric pressure chemical vapor deposition of vanadium oxides," *J. Mater. Chem.*, vol. 12, pp. 2936–2939, 2002.
- [7] A. Crunteanu, F. Dumas-Bouchiat, C. Champeaux, A. Catherinot, A. Pothier, and P. Blondy, "Microwave switching functions using reversible metal-insulator transition (MIT) in VO<sub>2</sub> thin films," in *Microwave Conference, 2007. European*, 2007, pp. 12–15.
- [8] Editorial, "The interface is still the device," *Nature Materials*, p. 11, Feb. 2012.
- [9] H. Berger, "Models for contacts to planar devices," *Solid-State Electron.*, vol. 15, no. 2, pp. 145 – 158, 1972.
- [10] G. S. Marlow and M. B. Das, "The effects of contact size and non-zero metal resistance on the determination of specific contact resistance," *Solid-State Electronics*, vol. 25, no. 2, pp. 91 – 94, 1982.
- [11] G. Reeves and H. B. Harrison, "Obtaining the specific contact resistance from transmission line model measurements," *Electron Device Letters, IEEE*, vol. 3, no. 5, pp. 111–113, 1982.

## Chapter 2: Background

Vanadium dioxide has long been understood to undergo a thermally-induced insulator-metal (IMT) transition at approximately 341 K (67 °C), characterized by an abrupt, reversible change in resistivity [1]. Even prior to the abrupt transition, the resistivity is highly dependent on temperature, decreasing by an order of magnitude between 300K and 330K. Furthermore, it has been demonstrated that the IMT in VO<sub>2</sub> can be electrically induced using current injection or an applied electric field [2], or an infrared or optical pump [3].

The IMT in VO<sub>2</sub> is accompanied by a change in the resistivity and a change in the reflectivity of the film. The change in resistivity varies from about one-half order of magnitude to 5 orders of magnitude depending on the transition method and film parameters [4]. A change in transmission of more than 40% is reported between the semiconducting and metallic state at terahertz, infrared, and optical frequencies [2, 3, 5].

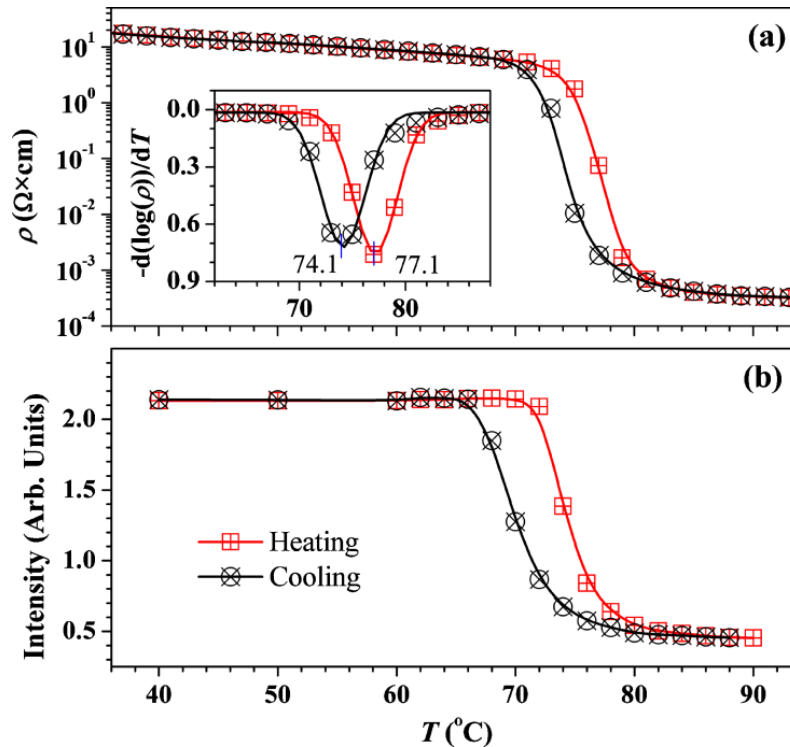


Figure 2.1: The change in (a) resistivity and (b) terahertz transmission of a VO<sub>2</sub> thin film with increasing and decreasing temperature [6].

Vanadium dioxide was first shown to experience a thermally driven transition from an insulating state to a metallic state in 1959 (Figure 2.2) when a change of more than 2 orders of

magnitude was observed at temperatures around 343 K. The resistivity was observed to return to its original state at a slightly lower temperature, about 332 K, creating a hysteric loop [1]. Improved  $\text{VO}_2$  growth methods have increased the change in resistivity to more than five orders of magnitude during a thermally driven IMT [7].

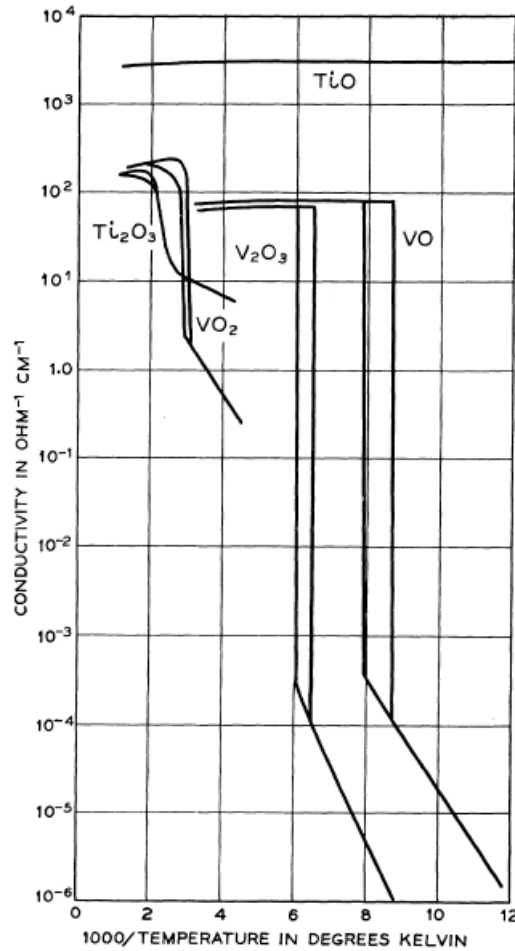


Figure 2.2: Conductivity of  $\text{VO}_2$  in addition to several other vanadium oxide species as a function of inverse temperature from the first published results showing the IMT for  $\text{VO}_2$  [1].

A phase transformation from a monoclinic structure at room temperature to a tetragonal structure above the critical temperature (Figure 2.3) is responsible for the IMT in thermally transitioned  $\text{VO}_2$ , including devices heated externally or through internal resistive heating [8]. There are indicators that the phase transition can also be initiated at higher speeds through non-thermal means such as photoexcitation [9] and that a change in reflectivity can be induced without the phase transformation [10].

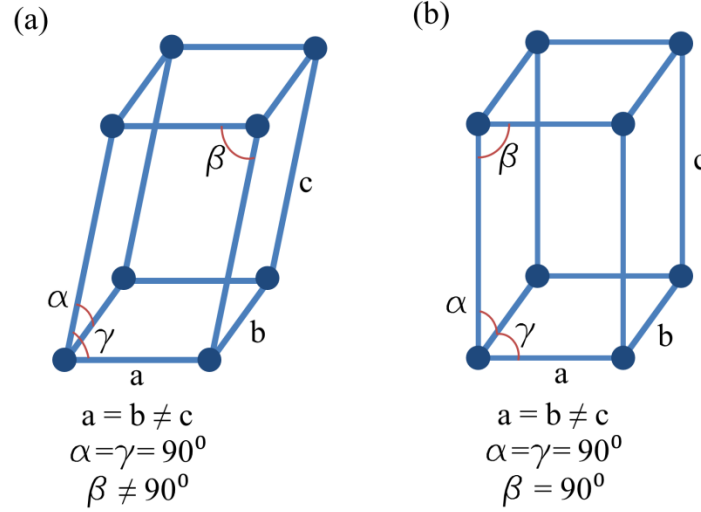


Figure 2.3: Lattice structures for VO<sub>2</sub>. (a) Monoclinic lattice seen below T<sub>c</sub> and (b) tetragonal lattice seen above the thermal transition temperature.

The IMT in VO<sub>2</sub> can also be triggered using a change in electric field (Figure 2.4a) or current injection (Figure 2.4b) [11]. The change in resistivity for VO<sub>2</sub> when triggered in this manner is about one half to one magnitude, which is much smaller than when changed using an external change in temperature [4]. As with the thermally induced transition, the current and voltage induced transitions also show a hysteresis in which the critical independent variable (temperature, voltage, or current) is lower when decreasing than when increasing [4].

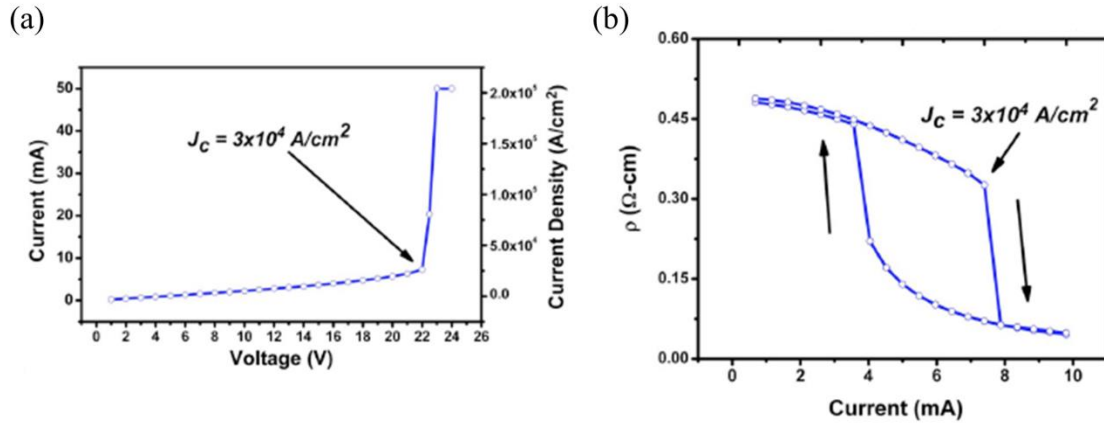


Figure 2.4: The (a) voltage induced and (b) current induced change in resistivity [4].

The cause of the current- and voltage- induced transition is under debate. There is evidence that it may be electronic [10] and/or thermal [12]. It may be that both mechanisms are possible but on very different timescales (pico- versus nano- seconds) or the device structure and size are critical in determining the mechanism. The two primary methods under consideration are

Joule heating [12] and a Mott-Hubbard type electronic transition [10]. It is believed that the IMT in the structures used in this research are driven by Joule heating (see appendix A).

Joule heating plays a major role in dc current-induced IMT. While there is no global temperature change, a localized increase in temperature within the film resulting from increasing current has been observed [12]. Zimmers et al. [12] used the fluorescence spectra of a rare-earth doped, micron sized particle to measure the local temperature of the  $\text{VO}_2$  in a channel between two gold contacts during a current and a voltage sweep measurement. It was shown that the local temperature in the channel at transition was equivalent to the transition temperature when the transition was induced using an external Peltier heater (Figure 2.5a). Additionally, it was shown that the critical bias value is lower when the external temperature is higher (Figure 2.5a). Lastly, the resistance as a function of the temperature of the  $\text{VO}_2$  film using the external Peltier heater (as measured using the fluorescing particle) and the local current driven Joule heating are superimposed indicating that thermal heating is responsible for the transition in both cases (Figure 2.5b) [12].

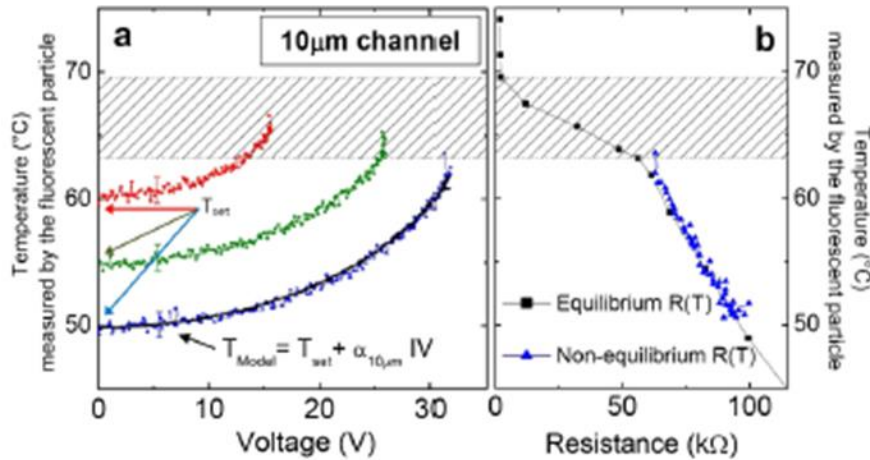


Figure 2.5: Results from Zimmers et al. showing that the voltage induced transition is caused by Joule heating. (a) The particle-measured temperature as a function of increasing voltage bias. The shaded region indicates the transition temperature as determined using a traditional resistivity-temperature measurement.  $T_{\text{set}}$  is the temperature from an external Peltier heater. (b) The resistance as a function of particle-measured temperature when the  $\text{VO}_2$  is transitioned using an external temperature (equilibrium  $R(T)$ ) and Joule heating (non-equilibrium  $R(T)$ ) [12].

The current-injection and electric field induced IMT may also be attributed to non-thermal effects. Stefanovich et al. measured the delay time of the phase transition after a rectangular voltage pulse. When compared to the time delay or switching time calculated using the heat balance equation, the measured time delay was about three orders of magnitude faster.

Refining the model cannot account for this large of a discrepancy. A second experiment investigated the effects of a current pulse or carrier injection on a voltage biased device. The delay after the injection and the recovery time were measured. It was found that a fast current pulse could trigger a transition even when the bias voltage was below the critical value. A critical electron density is required to initiate the transition without heating the lattice indicating that the material undergoes an electronic transition of the Mott-Hubbard type. It is also noted that based on these experiments the limiting speed for VO<sub>2</sub> electronic switches is on the order of 1 ps or 1 THz [10].

The IMT in VO<sub>2</sub> can also be induced using a terahertz [13], infrared [14], or optical signal [15]. Nakajima et al. used optical-pump terahertz-probe spectroscopy with a center wavelength of 800 nm to induce a transition in a VO<sub>2</sub> thin film. A decrease in terahertz transmission of approximately 40% corresponded to a change in electrical resistivity of over one magnitude. The change in transmission is attributed to an IMT phase change from the monoclinic to the tetragonal states; however, the transition occurs on a sub-picosecond timescale indicating that it is not a thermal process but rather photoinduced [15].

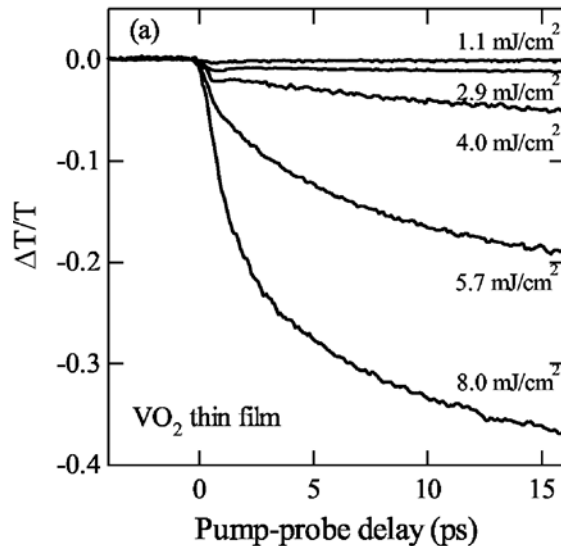


Figure 2.6: The change in transmission of a VO<sub>2</sub> film at 800nm for five different doses of incident radiation [15].



## 2.1 Vanadium Oxide Species

Many different species of vanadium oxide have been demonstrated using different growth techniques or variations of the same technique including  $V_2O_3$ ,  $V_2O_5$ ,  $VO$ ,  $VO_2$ ,  $V_6O_{13}$ , etc. [16]. Each species has its own set of properties, including different transition temperatures and magnitude of the change in resistivity (Figure 2.2). Mixed phase oxides can be tailored to obtain a desired property such as transition temperature [3]. Alternatively, small changes in the growth conditions or exposure to certain processes during fabrication can introduce unwanted variations.  $VO_2$  is chosen for this study because of the proximity of its transition temperature to room temperature.

## 2.2 $VO_2$ Growth

Vanadium dioxide thin films are grown/deposited using many different techniques such as sputtering [3], atomic layer deposition [17], reactive e-beam evaporation [18], sol-gel [19], metal-oxide chemical vapor deposition [20], pulsed laser deposition [21], and oxidation of vanadium thin films [22]. The  $VO_2$  used in this research was deposited at the University of Virginia nanoSTAR Institute Department of Materials Science.

Reactive Bias Target Ion Beam Deposition (RBTIBD) was used to deposit the  $VO_2$  thin film onto a c-plane sapphire substrate. For more details on this system, see [4]. For the films used in this study, the main chamber was pumped down to a base pressure of  $5 \times 10^{-8}$  Torr. The stage heater was set to 400-500 °C and allowed to stabilize for 45 min. The substrate surface was cleaned using Ar ions and the vanadium target was sputter-cleaned by applying a 35 V pulsed dc bias. Vanadium was sputtered in an 80/20 mixture of Ar and  $O_2$  at a flow rate of 5.0 to 6.0 sccm which results in a pressure of approximately 1 mTorr. The deposition time was approximately 2 hours producing a film thickness of about 100 nm.

The thin films were characterized after deposition but before device fabrication using a resistance-temperature measurement (Figure 2.7a), x-ray reflectometry (XRR), x-ray diffraction

(XRD) (Figure 2.7b), and atomic force microscopy (AFM) (Figure 2.7c, d). The XRR measures the film thickness, the XRD ensures that the film is single phase  $\text{VO}_2$ , the AFM is used to measure surface roughness and grain size, and the resistance-temperature measurement is used to find the critical transition temperature. A change in the transition temperature could be indicative of contamination, stress, or other flaws in the film.

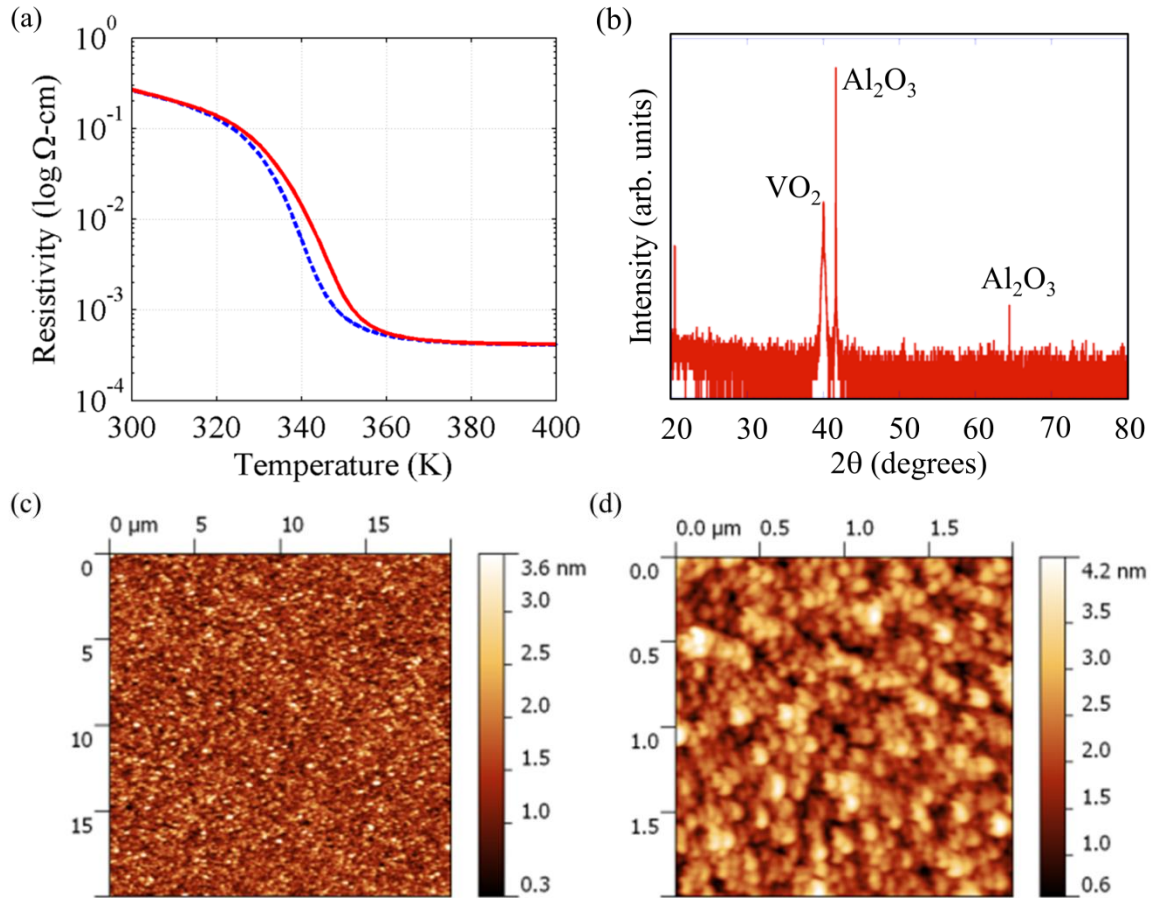


Figure 2.7: Typical characterization data for a  $\text{VO}_2$  thin film used in this research. (a) Resistance-temperature measurement, (b) XRD result, and (c, d) AFM data. [Courtesy: Salinporn Kittiwatanakul]

The  $\text{VO}_2$  thin films used in this research were nominally 100 nm thick, exhibited a room temperature resistivity of about  $0.3 \Omega\text{-cm}$ , a transition temperature of 340K, a thermal coefficient of resistance of about 3%/K, and an rms surface roughness under 1 nm. Small variations on the growth parameters and film characteristics were present between different wafers. Each task in this research used a different wafer, but a single wafer was used for the entirety of any specific task.

## 2.3 Microwave VO<sub>2</sub> Switches

In 2007, Crunteanu et al. demonstrated a coplanar waveguide fed, VO<sub>2</sub> microwave switch operating in the 5-35 GHz range and exploiting the IMT of VO<sub>2</sub>. This switch was shown to have a change in transmission (insertion loss) of over 20 dB using both the thermally triggered (Figure 2.8a) [23] and electrically triggered IMT (Figure 2.8b) [24]. The large change in insertion loss is useful for reconfigurable devices such as switched antenna arrays, communication networks, and tunable circuit components. Additionally, the speed of the electrically triggered transition is on the scale of several hundreds of nanoseconds which is much slower than electronic-based transition (picoseconds) and thus supports Joule heating as the mechanism driving the IMT [23].

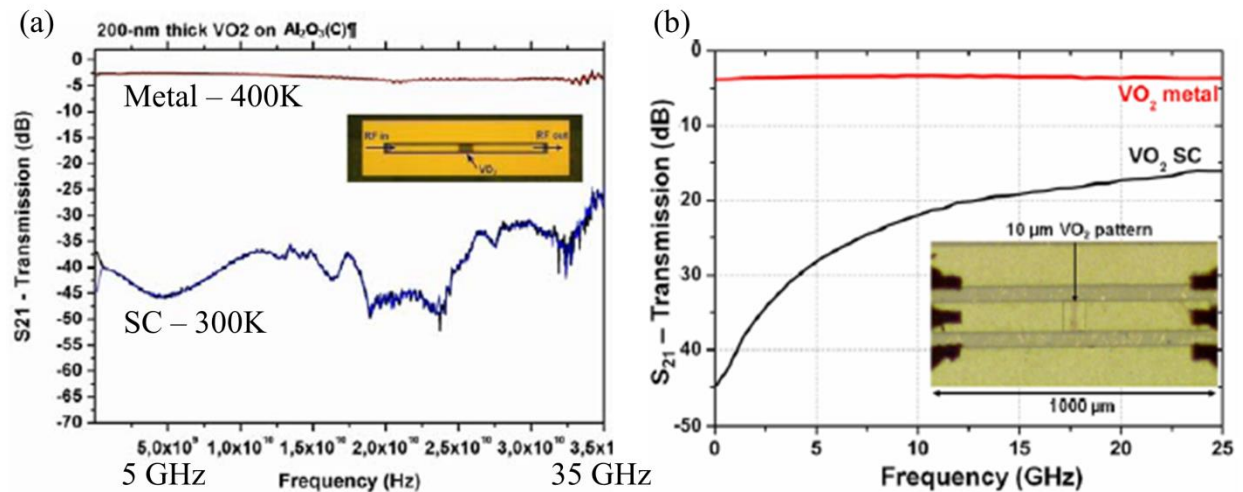


Figure 2.8: The transmission of a series, CPW driven VO<sub>2</sub> switch in the metallic and semiconducting states when the IMT is induced using (a) external heating [23] and (b) a voltage bias [24].

An electrically activated switch is preferable to the thermal switch because it is easier to implement and integrate into circuits. The change in insertion loss is greater than 15 dB for both voltage and current driven IMTs. However, the current driven transition has a much longer lifetime than the voltage driven device surviving more than 260 million cycles for the current device versus 16.25 million cycles for the voltage driven device. [24]. A similar device operating at 1 to 10 GHz was demonstrated by Dragoman et al. in 2006 [25].

## 2.4 Quasioptical Terahertz Switches Utilizing the VO<sub>2</sub> IMT

Quasioptical terahertz switches that use the VO<sub>2</sub> transition to tune the properties of an antenna or resonator have been previously realized. One such device is a hybrid Split Ring Resonator (SRR) VO<sub>2</sub> device (Figure 2.9a-c) [26]. The resonance frequency of a SRR is very sensitive to the dielectric properties of any materials, such as VO<sub>2</sub>, near a gap in the ring. Driscoll et al. (2008) demonstrated that the resonance frequency of the SRR can be tuned by carefully specifying the device temperature, and therefore the dielectric properties of the VO<sub>2</sub>, through the thermally driven transition. As the temperature and therefore the permittivity of the VO<sub>2</sub> increases, the SRR resonance frequency decreases (Figure 2.9d, e). When the VO<sub>2</sub> becomes fully metallic or the percolation of metallic islands combine to connect the two ends of the SRR, the SRR is shorted and effectively turned off [26].

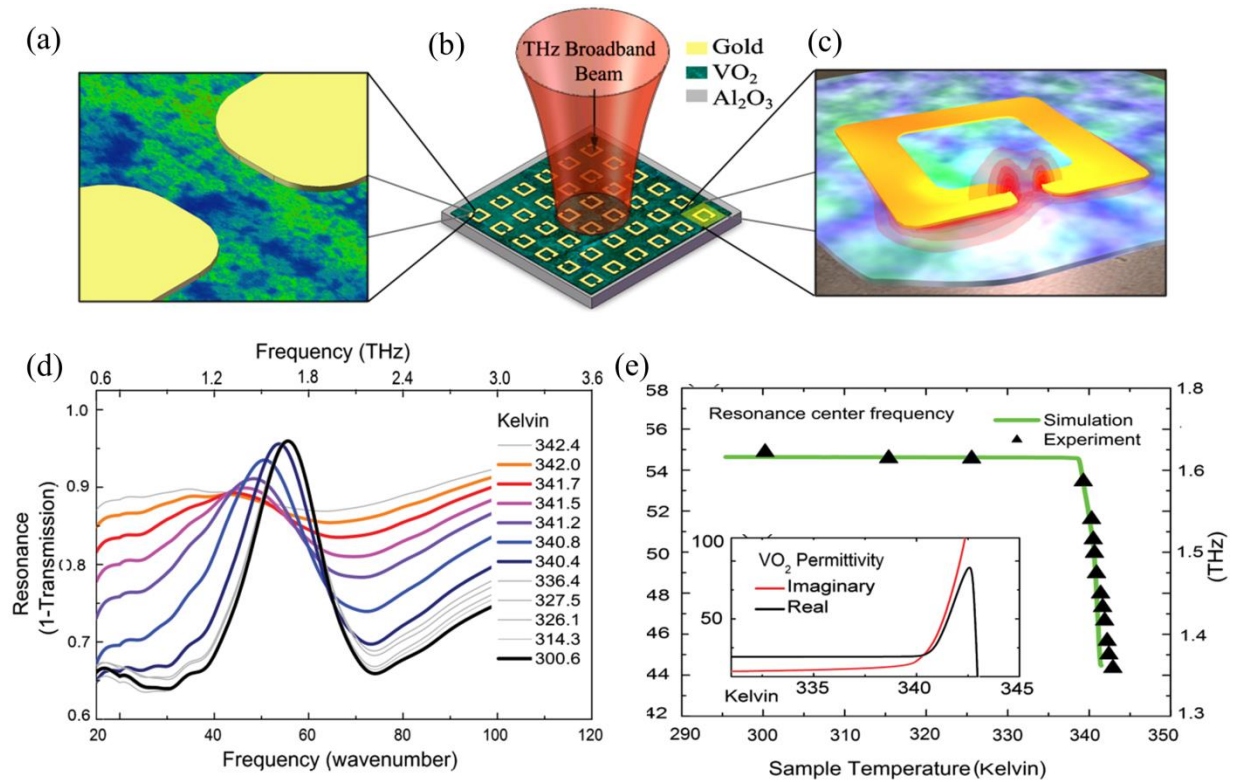


Figure 2.9: The VO<sub>2</sub> SRR device and results. (a) A sketch of the SRR gap overlaid on an sSNIM image taken at 342K. The green areas are metallic state VO<sub>2</sub> grains and the blue areas are semiconducting state VO<sub>2</sub>. (b) The SRR device layout. (c) A single SRR device with the simulated electric field superimposed. (d) The transmission spectra of the hybrid SRR shows the decrease in resonance frequency with increasing temperature. (e) The center resonance frequency remains constant until metallic regions percolate in the VO<sub>2</sub>. When the VO<sub>2</sub> becomes metallic, no resonance is seen [26].

VO<sub>2</sub> has also been demonstrated as an effective switching element in nanoantennas by Jeong et al. in 2011 [27]. In the insulating state, the nanoantennas transmit 0.3 to 1.0 THz radiation. When the VO<sub>2</sub> is transitioned to the metallic state using a dc-bias voltage, the antenna is shorted and the transmission is reduced to nearly 0. The peak in the transmission at 500 GHz is a result of the resonance frequency of the antenna and is not intrinsic to the VO<sub>2</sub> (**Error! Reference source not found.**) [27]. Similar experiments have demonstrated the change in transmission loss of these nano antennas using a thermally induced VO<sub>2</sub> transition [28] and optically induced VO<sub>2</sub> transition [29].

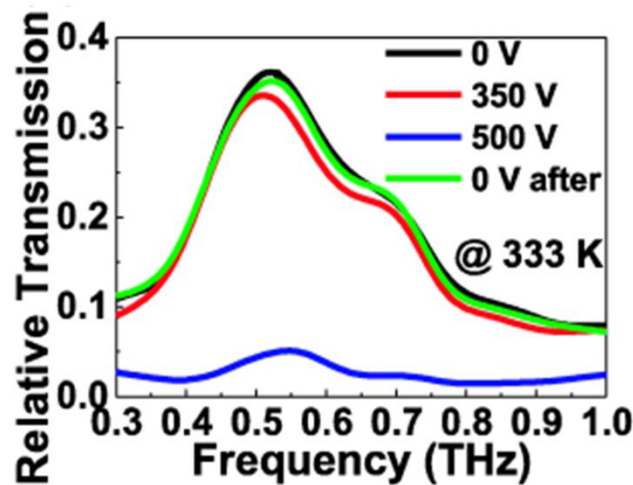


Figure 2.10: The transmission of the VO<sub>2</sub> switched nano antennas when the VO<sub>2</sub> is in the semiconducting (0, 350, 0V) and the metallic (500V) states [27].

The terahertz switches summarized both used quasioptical elements such as an antenna to switch the device. A change in the impedance of the feed point as a result of the IMT caused a change in the devices' resonant frequency and therefore a change in the device transmission. No references were found demonstrating on-wafer terahertz switches similar to the on-wafer microwave switch using VO<sub>2</sub> discussed in section 2.3.

- [1] F. J. Morin, "Oxides which show a metal-to-insulator transition at the Neel temperature," *Phys. Rev. Lett.*, vol. 3, pp. 34–36, Jul 1959.
- [2] W.-T. Liu, J. Cao, W. Fan, Z. Hao, M. C. Martin, Y. R. Shen, J. Wu, and F. Wang, "Intrinsic optical properties of vanadium dioxide near the insulator-metal transition," *Nano Letters*, vol. 11, no. 2, pp. 466–470, 2011.
- [3] H. Jerominek, D. Vincent, and F. Picard, "Vanadium oxide films for optical switching and detection," *Optical Engineering*, vol. 32, no. 9, pp. 2092–2099, 1993.
- [4] K. West, J. Lu, J. Yu, D. Kirkwood, W. Chen, Y. Pei, J. Claassen, and S. A. Wolf, "Growth and characterization of vanadium dioxide thin films prepared by reactive-biased target ion beam deposition," *Journal of Vacuum Science Technology A: Vacuum, Surfaces, and Films*, vol. 26, no. 1, pp. 133–139, 2008.
- [5] J. C. C. Fan, H. R. Fetterman, F. J. Bachner, P. M. Zavracky, and C. D. Parker, "Thin-film VO<sub>2</sub> submillimeter-wave modulators and polarizers," *Applied Physics Letters*, vol. 31, no. 1, pp. 11–13, 1977.
- [6] C. Chen, Y. Zhu, Y. Zhao, J. H. Lee, H. Wang, A. Bernussi, M. Holtz, and Z. Fan, "VO<sub>2</sub> multidomain heteroepitaxial growth and terahertz transmission modulation," *Applied Physics Letters*, vol. 97, no. 21, p. 211905, 2010.
- [7] J. MacChesney and H. Guggenheim, "Growth and electrical properties of vanadium dioxide single crystals containing selected impurity ions," *Journal of Physics and Chemistry of Solids*, vol. 30, no. 2, pp. 225 – 234, 1969.
- [8] W. Yin, K. G. West, J. W. Lu, Y. Pei, S. A. Wolf, P. Reinke, and Y. Sun, "The metal-insulator transition in vanadium dioxide: a view at bulk and surface contributions for thin films and the effect of annealing," *Journal of Applied Physics*, vol. 105, no. 11, p. 114322, 2009.
- [9] A. Cavalleri, C. Tóth, C. W. Siders, J. A. Squier, F. Ráksi, P. Forget, and J. C. Kieffer, "Femtosecond structural dynamics in VO<sub>2</sub> during an ultrafast solid-solid phase transition," *Phys. Rev. Lett.*, vol. 87, p. 237401, Nov 2001.

- [10] G. Stefanovich, A. Pergament, and D. Stefanovich, “Electrical switching and Mott transition in VO<sub>2</sub>,” *Journal of Physics: Condensed Matter*, vol. 12, no. 41, p. 8837, 2000.
- [11] C. Berglund, “Thermal filaments in vanadium dioxide,” *Electron Devices, IEEE Transactions on*, vol. 16, no. 5, pp. 432–437, 1969.
- [12] A. Zimmers, L. Aigouy, M. Mortier, A. Sharoni, S. Wang, K. G. West, J. G. Ramirez, and I. K. Schuller, “Role of thermal heating on the voltage induced insulator-metal transition in VO<sub>2</sub>,” *Phys. Rev. Lett.*, vol. 110, p. 056601, Jan 2013.
- [13] M. Liu, H. Y. Hwang, H. Tao, A. C. Strikwerda, K. Fan, G. R. Keiser, A. J. Sternbach, K. G. West, S. Kittiwatanakul, J. Lu, S. A. Wolf, F. G. Omenetto, X. Zhang, K. A. Nelson, and R. D. Averitt, “Terahertz-field-induced insulator-to-metal transition in vanadium dioxide metamaterial,” *Nature*, vol. 487, pp. 345–348, July 2012.
- [14] F. Cilento, C. Giannetti, G. Ferrini, S. D. Conte, T. Sala, G. Coslovich, M. Rini, A. Cavalleri, and F. Parmigiani, “Ultrafast insulator-to-metal phase transition as a switch to measure the spectrogram of a supercontinuum light pulse,” *Applied Physics Letters*, vol. 96, no. 2, p. 021102, 2010.
- [15] M. Nakajima, N. Takubo, Z. Hiroi, Y. Ueda, and T. Suemoto, “Photoinduced metallic state in VO<sub>2</sub> proved by the terahertz pump-probe spectroscopy,” *Applied Physics Letters*, vol. 92, no. 1, p. 011907, 2008.
- [16] T. Kozo, Z.-c. Li, Y.-q. Wang, J. Ni, Y. Hu, and Z.-j. Zhang, “Oxidation phase growth diagram of vanadium oxides film fabricated by rapid thermal annealing,” *English Frontiers of Materials Science in China*, vol. 3, no. 1, pp. 48–52, 2009.
- [17] P. Dagur, A. U. Mane, and S. Shivashankar, “Thin films of VO<sub>2</sub> on glass by atomic layer deposition: microstructure and electrical properties,” *Journal of Crystal Growth*, vol. 275, no. 12, pp. 1223 – 1228, 2005.
- [18] M.-H. Lee and M.-G. Kim, “RTA and stoichiometry effect on the thermochromism of VO<sub>2</sub> thin films,” *Thin Solid Films*, vol. 286, no. 12, pp. 219 – 222, 1996.

- [19] D. P. Partlow, S. R. Gurkovich, K. C. Radford, and L. J. Denes, "Switchable vanadium oxide films by a sol-gel process," *Journal of Applied Physics*, vol. 70, no. 1, pp. 443–452, 1991.
- [20] M. B. Sahana, G. N. Subbanna, and S. A. Shivashankar, "Phase transformation and semiconductor-metal transition in thin films of VO<sub>2</sub> deposited by low-pressure metal organic chemical vapor deposition," *Journal of Applied Physics*, vol. 92, no. 11, pp. 6495–6504, 2002.
- [21] D. H. Kim and H. S. Kwok, "Pulsed laser deposition of VO<sub>2</sub> thin films," *Applied Physics Letters*, vol. 65, no. 25, pp. 3188–3190, 1994.
- [22] K. Martens, I. P. Radu, S. Mertens, X. Shi, L. Nyns, S. Cosemans, P. Favia, H. Bender, T. Conard, M. Schaekers, S. De Gendt, V. Afanas'ev, J. A. Kittl, M. Heyns, and M. Jurczak, "The VO<sub>2</sub> interface, the metal-insulator transition tunnel junction, and the metal-insulator transition switch on-off resistance," *Journal of Applied Physics*, vol. 112, no. 12, p. 124501, 2012.
- [23] A. Crunteanu, F. Dumas-Bouchiat, C. Champeaux, A. Catherinot, A. Pothier, and P. Blondy, "Microwave switching functions using reversible metal-insulator transition (MIT) in VO<sub>2</sub> thin films," in *Microwave Conference, 2007. European*, 2007, pp. 12–15.
- [24] A. Crunteanu, J. Givernaud, J. Leroy, D. Mardivirin, C. Champeaux, J.-C. Orlianges, A. Catherinot, and P. Blondy, "Voltage- and current-activated metal-insulator transition in VO<sub>2</sub> -based electrical switches: a lifetime operation analysis," *Science and Technology of Advanced Materials*, vol. 11, no. 6, p. 065002, 2010.
- [25] M. Dragoman, A. Cismaru, H. Hartnagel, and R. Plana, "Reversible metal-semiconductor transitions for microwave switching applications," *Applied Physics Letters*, vol. 88, p. 073503, 2006.
- [26] T. Driscoll, S. Palit, M. M. Qazilbash, M. Brehm, F. Keilmann, B.-G. Chae, S.-J. Yun, H.-T. Kim, S. Y. Cho, N. M. Jokerst, D. R. Smith, and D. N. Basov, "Dynamic tuning of an infrared hybrid-metamaterial resonance using vanadium dioxide," *Applied Physics Letters*, vol. 93, no. 2, p. 024101, 2008.



- [27] Y.-G. Jeong, H. Bernien, J.-S. Kyoung, H.-R. Park, H. Kim, J.-W. Choi, B.-J. Kim, H.-T. Kim, K. J. Ahn, and D.-S. Kim, “Electrical control of terahertz nano antennas on VO<sub>2</sub> thin film,” *Opt. Express*, vol. 19, no. 22, pp. 21211–21215, Oct 2011.
- [28] M. Seo, J. Kyoung, H. Park, S. Koo, H.-s. Kim, H. Bernien, B. J. Kim, J. H. Choe, Y. H. Ahn, H.-T. Kim, N. Park, Q.-H. Park, K. Ahn, and D.-S. Kim, “Active terahertz nanoantennas based on VO<sub>2</sub> phase transition,” *Nano Letters*, vol. 10, no. 6, pp. 2064–2068, 2010.
- [29] J. Kyoung, M. Seo, H. Park, S. Koo, H. sun Kim, Y. Park, B.-J. Kim, K. Ahn, N. Park, H.-T. Kim, and D.-S. Kim, “Giant nonlinear response of terahertz nanoresonators on VO<sub>2</sub> thin film,” *Opt. Express*, vol. 18, no. 16, pp. 16452–16459, Aug 2010.

## **Chapter 3: The Effects of Common Fabrication Processes and Reagents on VO<sub>2</sub> Thin Film**

Over the past few years, vanadium dioxide films have received increased interest for their potential use in new electronic devices. As new device concepts are proposed and developed, VO<sub>2</sub> films are exposed to many standard chemicals used for semiconductor device processing, including etchants, organic solvents, and other reagents. During fabrication of devices for this dissertation, changes to the resistance and appearance of VO<sub>2</sub> films were observed. It was hypothesized that some of the chemicals and processes used during device fabrication were etching or otherwise altering the VO<sub>2</sub> films. Some common chemicals to which the films are exposed during processing include propylene glycol, deionized water, and acetone. The changes to VO<sub>2</sub> as a result of exposure to these reagents were observed through both changes in current-voltage characteristics as well as visual inspection. This chapter documents a study on the effects of several common reagents and processes used to fabricate VO<sub>2</sub> devices. A list of experimental procedures, processes, and diagnostics are introduced in section 3.1. The individual processes are discussed, the experimental parameters given, and the results presented in section 3.2. Section 3.3 reviews the results by analysis technique and discusses more general observations and conclusions. Finally, section 3.4 states some conclusions based on the results.

### **3.1 Experimental Procedure**

Vanadium dioxide films were methodically exposed to several common reagents and processes utilized to fabricate the VO<sub>2</sub> devices presented in this dissertation. These processes are discussed in section 3.1.2. The chemical concentrations, temperatures, and exposure times were chosen based on the fabrication recipes used to make the devices in this thesis. In the case of the oxygen plasma, water, and acetone, exaggerated times were investigated due to their prevalence in most fabrication procedures. Additionally, any changes to the film, such as etching, would be more pronounced and easier to detect. After exposure, each sample was visually inspected and a resistance measurement was performed to characterize changes in the resistivity of the film. Any

deviation from the control was further investigated and quantified using one or more of the diagnostic methods that are described in section 3.1.3.

### **3.1.1 VO<sub>2</sub> Film Preparation**

A two inch wafer of 116 nm VO<sub>2</sub> thin film deposited on gold that was evaporated onto a 2 inch c-Al<sub>2</sub>O<sub>3</sub> substrate was used for this experiment. A 10 nm titanium adhesion layer and a 100 nm gold layer were e-beam deposited onto a sapphire substrate using e-beam evaporation prior to depositing the VO<sub>2</sub>. The VO<sub>2</sub> film was deposited using RBTIBD at a stage temperature of 525 °C, an O<sub>2</sub> flow rate of 6 sccm, and a pressure of 1 mTorr for 3 hours.

An approximately 1 cm wide sample was removed from the side of the wafer by scribing. This sample served as the control for later XRD measurements on samples that had been processed. After removal from the RBTIBD system, the control sample was not exposed to any chemicals or processes other than ambient air and temperatures. The remaining portion of the wafer was affixed, face down, to a silicon carrier using black wax at 140 °C. The wafer was diced into nine 1 cm x 1 cm samples and 9 partial edge samples. Each sample was assigned a letter and labeled on the back side using a scribing pen. The letter was assigned to a process using a key; however, the key was not revealed during diagnostics. The samples were then removed from the carrier using a 140 °C hot plate. The black wax was removed by spraying each sample with trichloroethylene (TCE) then rinsing with methanol. The samples were dried using an N<sub>2</sub> air burst. With the exception of the control sample removed via scribing prior to dicing preparation, each of the samples was exposed to this dicing process.

### **3.1.2 Fabrication Processes Considered in this Study**

When processing vanadium dioxide devices, the film is typically subjected to a variety of different chemicals and environments. During fabrication of the initial devices discussed in this work, a lack of repeatability between batches and even across a given wafer was observed. It was

hypothesized that the film was being altered during the processing of the devices. After film deposition but prior to lithographic patterning, the VO<sub>2</sub> thin films are characterized, stored, and transported to the University of Virginia Microfabrication Lab (UVML). The surface is prepared using an isopropyl alcohol, d-limonene, and methanol spin clean, dried using an N<sub>2</sub> air gun, then placed in an O<sub>2</sub> plasma to remove any organic compounds present on the surface. Acetone is used to remove resist after etch step or in the event a lithography step needs to be repeated. Lithography exposes the film to photoresist, ultraviolet light (340 nm), resist developer, and DI water. Lift-off procedures expose it to acetone, N-Methyl-2-pyrrolidone (NMP), or an NMP and propylene-glycol mixture at elevated temperatures (80 or 120 °C). The wafer is also heated during lithography to cure the resist. Lastly, deionized water (DI water) is used to rinse the wafer and to dilute other solutions. Each of these chemicals and processes was considered in this study for its potential to etch or alter the VO<sub>2</sub> film.

### 3.1.3 Diagnostic Tools

There are many techniques and diagnostic tools available to characterize thin films. Three different tools housed at the University of Virginia were used to characterize the VO<sub>2</sub> films and any changes to the sample. Each sample was initially inspected visually with an unaided eye. The small-signal resistance was measured using a fixed probe setup. The VO<sub>2</sub> thickness was measured to a resolution of 1 nm using x-ray reflectometry (XRR). If any of these methods indicated a change to the sample, an x-ray diffraction (XRD) measurement was made to identify any new vanadium oxide species that may have been introduced during the fabrication process.

The resistance of the film was measured using a Keithley 236 source-measure unit attached to a fixed probe setup (Figure 3.1). A vacuum holds the sample on a ceramic holder inlaid in the stage. The stage is controlled by a computer operated microcontroller. The vertical motion is automated so the force of the probe tips on the sample is consistent for all samples at approximately 10 mN. The probes are in a ground-signal-ground configuration for WR-2.0 coplanar waveguide measurements; however, in this experiment they are placed directly on the VO<sub>2</sub> film and used only at dc. The spacing between the ground and signal lines is 45 μm. The

film was biased through the probe tips. Each measurement was voltage swept with a step size of 10 mV until the sensed current reached the compliance level of 10  $\mu\text{A}$ , indicating that the  $\text{VO}_2$  had transitioned to the metallic state. The voltage was then swept back to 0V in -10 mV steps while the current was measured. The measurement was repeated five times at five different locations on each wafer to account for inhomogeneity in the film. The resistance was calculated by taking the inverse of the slope as found using least-squares linear regression on the measurement set.

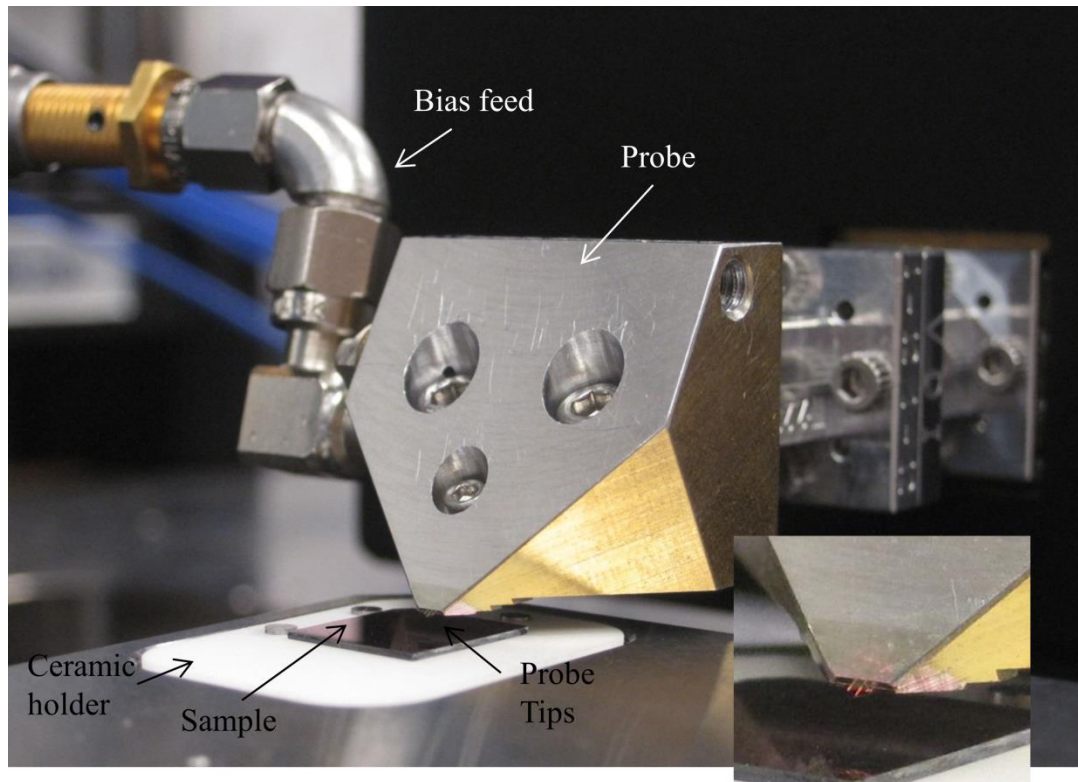


Figure 3.1: Photograph of the dc probe test setup. The inset shows a close-up photograph of the tips themselves.

### 3.2 Process and Solutions Descriptions

In this section, the processes listed in section 3.1.2 are presented in more detail. A brief description of each process and its purpose is given. Any early evidence of alteration to the  $\text{VO}_2$  by the process including in the literature are presented. The details such as time and temperature of the process or solution are given. Finally, the results for each of the processes are presented.

### 3.2.1 Dicing Saw

A DISCO dicing saw is used to separate die from a wafer with high precision. In this experiment, it is used to cut the wafer into uniform 1 cm x 1 cm pieces. The wafer is attached face down to a silicon carrier using black wax. It is then diced into individual samples using an automated program. After dicing, the wafer is removed from the carrier on a hot plate and rinsed using TCE and methanol.

There were no indications that the black wax or the cleaning reagents altered the VO<sub>2</sub> thin film; however, the dicing process had to be modified for the sapphire substrate. With most silicon wafer based devices, the wafer is completely cut through with a dicing saw using a single pass at each location. When the sapphire was cut through completely using a single pass, several problems arose. The most common problem was the blade breaking. Special blades are available for dicing hard materials such as sapphire; however, they are expensive and do not perform much better when used for a small number of cuts over several different sessions. It was instead recommended to use a thicker blade (DISCO NBC - ZH-2 05 O - SE 27HE EE) and multiple passes per cut. This reduced blade breakage but still led to other issues. The VO<sub>2</sub> thin film would sometimes delaminate from the sapphire substrate around the edges of the diced sample or diced samples would detach from the carrier causing the sample to be ruined or loss or cause blade breakage. These issues were prevented by only dicing about ½ to ¾ of the way through the 400 µm thick sapphire substrate. The wafer was then removed from the carrier and placed face down on a slightly concave surface. Gentle pressure was applied to the wafer using a fingertip causing the wafer to break into smaller samples along the dicing saw cuts. The process of applying gentle pressure was repeated until all samples were separated.

This modified method was used to dice a wafer into 1 cm x 1 cm samples. The VO<sub>2</sub> thin film on a 400 µm sapphire substrate was affixed face down to a silicon carrier using black wax at 140 °C. The sapphire wafer was diced to a depth of 200 µm with a diamond blade under a jet of cooling water. It was removed from the carrier using a 140 °C hot plate. The wafer generally broke into rows during removal from the carrier. Any samples that had not yet separated were placed face down on a concave surface and pressed gently in the center which caused the samples to break along the diced lines. The black wax was removed by spraying each sample

with TCE then rinsing with methanol. The samples were dried using an N<sub>2</sub> air burst. When analyzing the results, there was no change in appearance, thickness, or resistance compared to the sample removed prior to dicing.

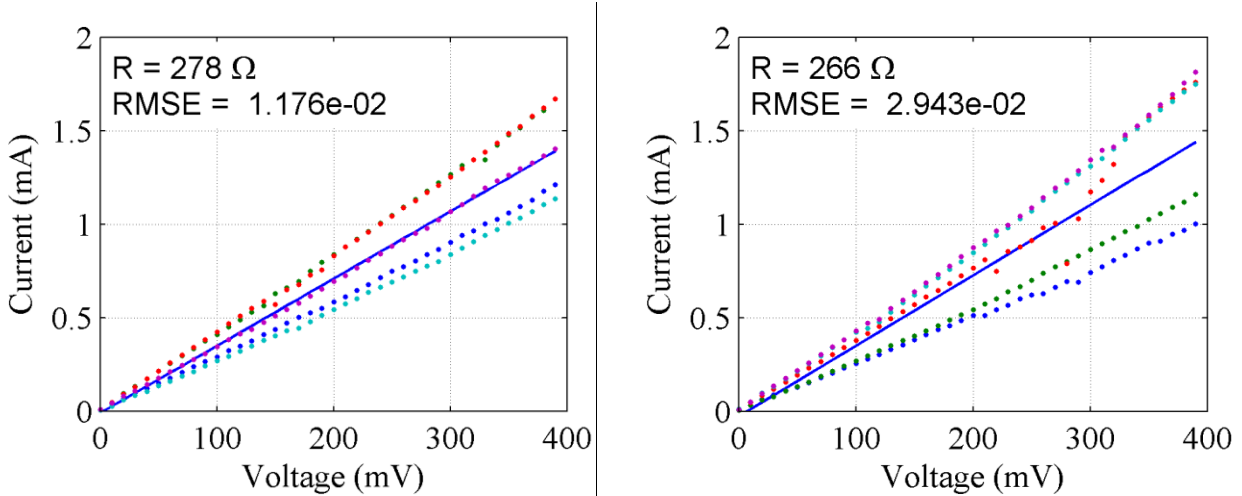


Figure 3.2: Voltage-current measurement at multiple locations on two different dicing saw samples. The solid line represents the linear regression results to the dataset, the slope of which is used to calculate the average resistance across the wafer. This dataset is used as the control set.

### 3.2.2 Acetone

Acetone is a common reagent used during fabrication. It is used to remove resist after failed lithography steps and is frequently used for the liftoff itself. To remove unexposed resist, a spin clean using acetone for approximately 30 seconds followed by a spin clean of methanol is used. For baked-on resist and liftoff, the wafer is submerged in acetone and agitated manually using tweezers or a beaker in which the sample is submerged in acetone is placed in an ultrasonic water bath for several minutes, depending on the process requirements.

The first evidence of acetone possibly affecting the material occurred after a failed lithography step. AZ4110 resist was removed using an acetone spin clean. Upon inspection, an imprint of the pattern could still be seen when the wafer was observed at certain angles. The pattern was not successfully imaged with the optical microscope and a change in height was not found using the Veeco Dektak-8, which has an ideal vertical resolution of 10 Å. An adhesion promoter, such as HMDS, was not applied prior to applying the photoresist so the film was not

caused by residue from such a layer. The wafer was placed in an  $O_2$  plasma clean overnight at 120 W but the pattern remained. While this observation is not definitive evidence that acetone produced the residual image, it indicated a need for further investigation.

To investigate the effect of acetone on a  $VO_2$  film, a  $VO_2$  sample was submerged in a room temperature, un-agitated beaker of acetone for 23.5 hours. In most processing recipes, acetone exposure would be on the order of one minute to one hour. The extended time was used to make any effects more evident. The wafer was removed from the acetone and rinsed briefly with methanol followed by an  $N_2$  dry.

There was no visible change to the sample exposed to acetone. The resistance of the sample, however, increased to 70 times that of the control sample even though the color and thickness of the  $VO_2$  film remained unchanged. These results indicate that the acetone may have altered the  $VO_2$ ; however, the nature of these changes was not determined in this investigation.

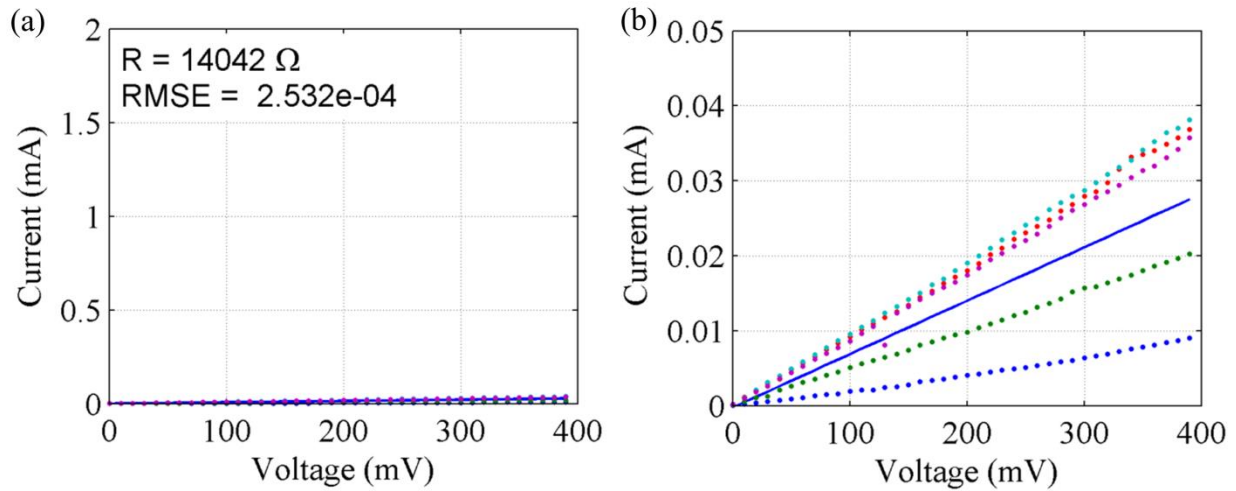


Figure 3.3: Voltage-current measurement at multiple locations across the acetone-exposed sample. The solid line represents the linear regression results to the dataset, the slope of which is used to calculate the average resistance across the wafer. (a) Using the same plot scale as the other plots in this chapter to provide a quick relative comparison of the slopes and (b) using a smaller y-axis scale.

### 3.2.3 $O_2$ Plasma Clean

A March PX250 plasma etcher (Figure 3.4) uses an oxygen plasma to ash or burn off photoresist and to remove organics from a wafer surface. The March system was operated with



an oxygen flow rate of 80 sccm, a pressure of approximately 800 mTorr, and a RF power of 120 W. The sample was placed on a house-water cooled aluminum plate to prevent heating. The system was used for three different purposes during the fabrication of these devices. After a spin clean, the wafer was placed in an O<sub>2</sub> plasma for 10 minutes to remove any residue or stray organics on the surface of the VO<sub>2</sub>. To improve liftoff quality, the March O<sub>2</sub> plasma was used for 10 minutes after developing the photoresist to remove any residual photoresist. A five hour O<sub>2</sub> plasma ash was used to remove the photoresist used to pattern the VO<sub>2</sub> for etching.

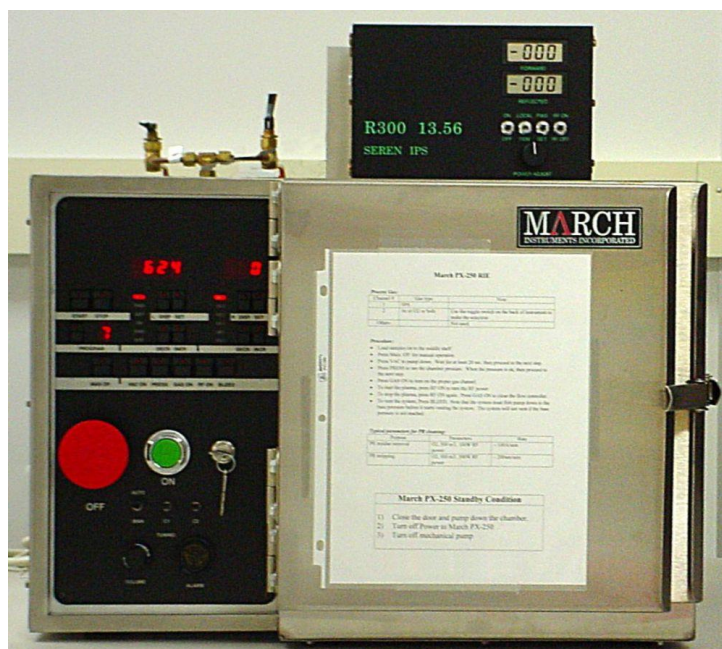


Figure 3.4: A March PX50 plasma cleaning system [Courtesy: <http://kmf.pa.msu.edu/KMF/Equipment/equip11.asp>]

There is concern that the O<sub>2</sub> plasma clean may enable the growth of other vanadium oxides on an exposed VO<sub>2</sub> film. The O<sub>2</sub> plasma could provide oxygen atoms with sufficient energy to further oxidize the VO<sub>2</sub>. V<sub>2</sub>O<sub>5</sub> nanowires have been grown in room temperature O<sub>2</sub> plasma from vanadium metal foils [1]. Additionally, vanadium oxide films are sometimes grown using an oxygen rich environment at elevated temperatures [2].

To test for the effects of the O<sub>2</sub> plasma clean, a single sample of the VO<sub>2</sub> wafer was placed in the March O<sub>2</sub> plasma for an extended amount of time. The oxygen flow rate was 80 sccm, the pressure was 840 mTorr, and the RF power was 120 W. The platen on which the wafer was placed was cooled to room temperature using the house water supply. The exposure time

was somewhere between 10 and 24 hours although the exact amount of time that the wafer was in the plasma is unknown.

The O<sub>2</sub> plasma exposed sample had a change in color from teal to emerald, an increase in resistance of 2500%, and the XRR indicated the presence of an amorphous VO film, possibly V<sub>2</sub>O<sub>5</sub>. XRD did not indicate the presence of a VO film side from VO<sub>2</sub>; however, an amorphous film would have a broad, shallow peak rather than the sharp peaks from the VO<sub>2</sub>, Al<sub>2</sub>O<sub>3</sub> substrate, and thin gold layer and may not be distinguishable from the other features (see section 3.3.4, Figure 3.16).

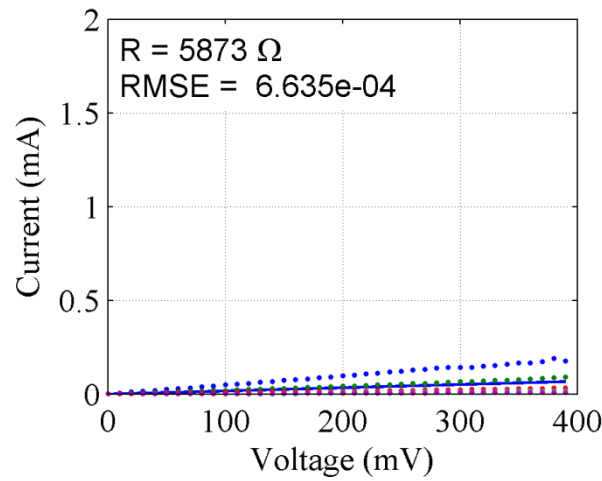


Figure 3.5: Voltage-current measurement at multiple locations across the O<sub>2</sub> plasma-exposed sample. The solid line represents the linear regression results to the dataset, the slope of which is used to calculate the average resistance across the wafer.

The March O<sub>2</sub> plasma cleaned wafer exhibited an extra feature during XRR measurements. XRR uses the interference pattern of a reflected x-ray signal to determine the thickness, density, and roughness of a thin film. The thickness is determined by the period of the oscillations of the reflected signal with decreasing incident angle. A model of the expected profile is input to the XRR analysis software package. The thickness, density, and roughness of the model are adjusted until the parameters provide the best match to the data. In the case of the O<sub>2</sub> plasma exposed sample, a model consisting of 100 nm VO<sub>2</sub> on 100 nm gold on sapphire model could not provide a reasonable fit to the data. The poor fit was most evident in an extra shoulder feature in the dataset at an incident angle of about 0.5° (Figure 3.6). An additional vanadium oxide layer in the model was necessary to obtain a reasonable fit to the data. In this case, a 26 nm layer of V<sub>2</sub>O<sub>5</sub> on 124 nm VO<sub>2</sub> resulted in the lowest residuals and the best fit to the

data. Without further analysis, it cannot be firmly concluded that  $V_2O_5$  specifically is present; however, based on visual and XRR results, it is concluded that the  $O_2$  plasma clean process caused the growth of an amorphous vanadium oxide film with a different oxidation state on the surface of the  $VO_2$  film.

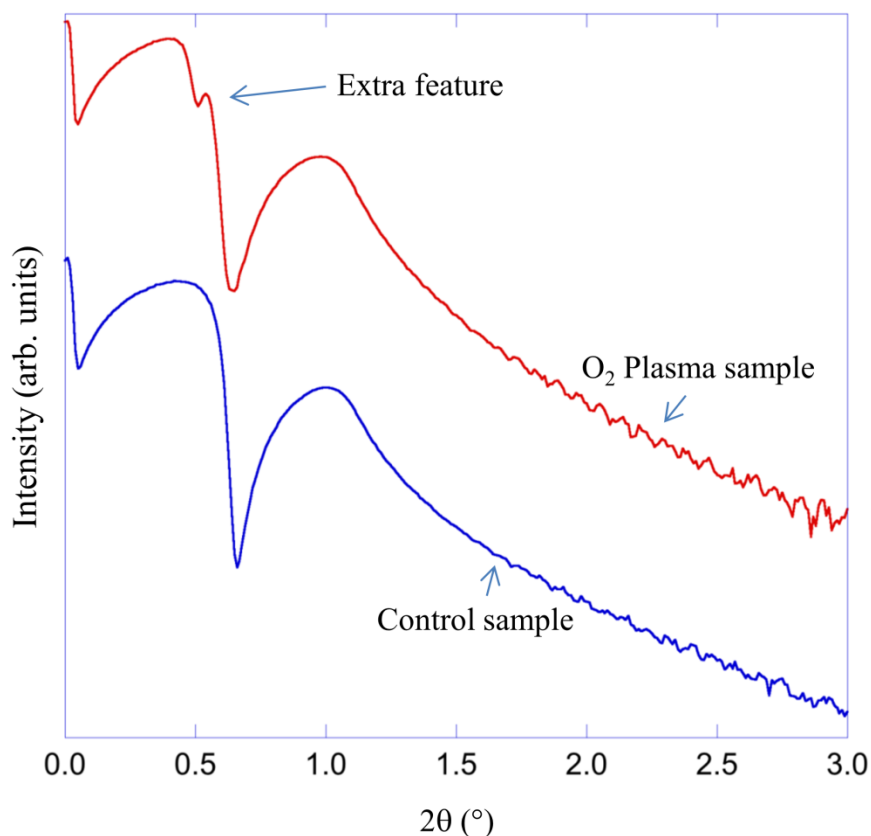


Figure 3.6: XRR data comparing a control sample with the sample exposed to  $O_2$  plasma.

$O_2$  plasma is not a recommended method for cleaning the wafer or removing residual and hardened resist. Even cooled to room temperature, the  $O_2$  plasma cleaning procedure caused the growth of a different stoichiometry vanadium oxide on the  $VO_2$  film. This can change many of the properties of the film including resistivity and critical transition values (e.g. temperature, current/voltage).

Exposure to  $O_2$  plasma can be reduced significantly. Instead of using the plasma to fully remove resist, it could be used for a short time to remove a top hardened layer followed by acetone or developer to remove the bulk of the resist. Alternatively, the plasma ash could be more carefully monitored so that the wafer is removed from the March as soon as the resist

removal is complete. The  $O_2$  plasma is not necessary to remove residual resist in liftoff procedure and can be skipped.

### 3.2.4 Deionized Water

Deionized (DI) water is used to rinse wafers after development or lift-off and to dilute other solutions such as developer.  $VO_{2+x}$  should not be removed in DI water; however,  $V_2O_5$  is known to dissolve in water, a property that is used to check for  $V_2O_5$  in a film [2]. A change in resistivity resulting from exposure to DI water may not be caused by dissolved or etched  $VO_2$  but rather the removal of other species that have formed during the fabrication process.

Some vanadium oxides are known to be soluble in water [3]. In an initial experiment, a sample of 94 nm thick  $VO_2$  on  $Al_2O_3$  was set in un-agitated, room temperature, de-ionized water for intervals of 30 minutes at which point the voltage was measured using a fixed four point probe and source currents of 10  $\mu A$  and 100  $\mu A$ . An increase in voltage represents an increase in resistivity and therefore a change in the intrinsic material properties or a thinning of the film. The exact resistivity is not calculated due to the non-uniform shape of the sample; however, an exact measurement is unnecessary. The critical measurement is the difference between the before and after measured values. After the sample was submerged in DI water for 3 hours, the measured voltage increased by more than 10% indicating that the DI water did alter the  $VO_2$  film. Using x-ray reflectivity, the film thickness was measured as 65 nm indicating an etch rate of about 10 nm per hour. The sample was returned to the water to soak overnight. In the morning, the  $VO_2$  had been completely removed and an open circuit was detected.

For consistency with the analysis in this chapter, this measurement was repeated. Two different samples of  $VO_2$  were exposed to DI water. One sample was placed in a beaker of un-agitated DI water at room temperature for 23.5 hours. The other sample was placed in a beaker of un-agitated DI water at 80 °C for one hour. These values were chosen to represent two different potential uses of DI water. A wafer is exposed to DI water multiple times in the fabrication process. It is used to rinse the wafer after developing the photoresist, rinse off NMP

after liftoff, and to dilute some reagents such as the AZ400k developer. The heated water is used in the event that the water affects the metallic state differently than the semiconducting state.

The two samples exposed to DI water had a violet hue when removed. The sample exposed to 80 °C water for one hour was etched 15 nm yielding an etch rate of about 2.5 Å/minute (15 nm/hr). The XRD and XRR measurements of the control sample did not show the presence of  $V_2O_5$  before or after exposure to DI water, indicating that the change in thickness is not a result of  $V_2O_5$  contaminants dissolving.

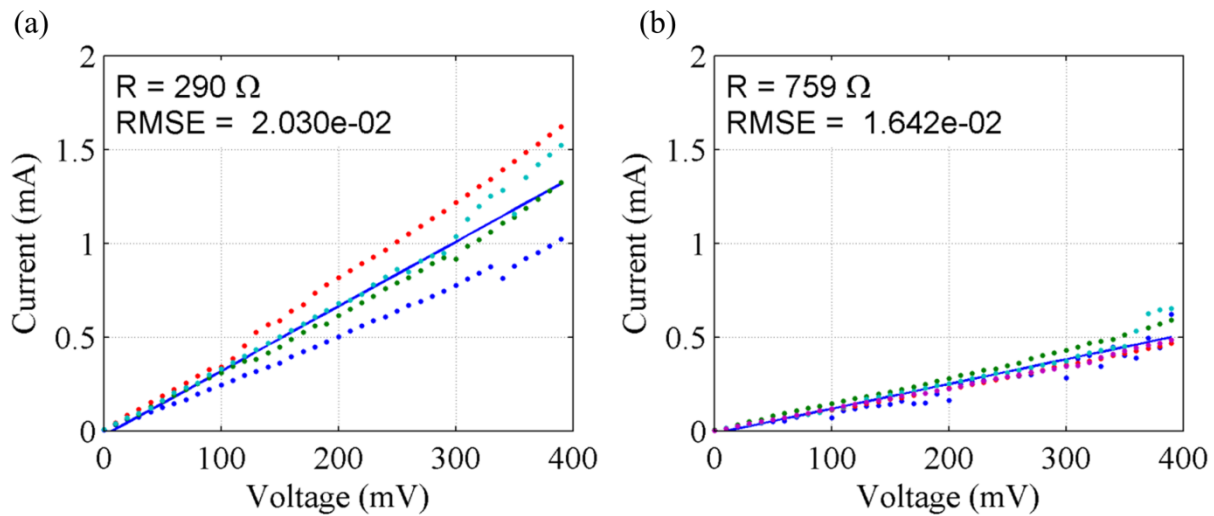


Figure 3.7: Voltage-current measurements at multiple locations across the (a) 80 degree and (b) room temperature DI water exposed samples. The solid line represents the linear regression results to the dataset, the slope of which is used to calculate the average resistance across the wafer.

### 3.2.5 Increased Temperature in Ambient Conditions

Hot plates in ambient conditions are frequently employed during device processing to dry wafers and cure resists. During fabrication, a wafer is heated to 110 °C for 5 minutes prior to photolithography to remove water adsorbed to its surface. During lithography, the resist was soft baked at 110 °C for one minute. In other photolithography processes available at UVML, temperatures of up to 160 °C are used for durations of several minutes.

It has been shown that temperatures above 300 °C in a vacuum cause the surface to undergo an irreversible IMT as a result of oxygen depletion on the surface of  $VO_2$  thin films [4]. Additionally, elevated temperatures in oxygen or water vapor rich environments are used to grow

or change the species of vanadium oxides [5]. While there were no initial indications that heating the  $\text{VO}_2$  to 110 °C or 160 °C in ambient conditions alters the film, the temperatures are included in this investigation for verification.

Two different samples were heated on hot plates in ambient conditions in the photolithography laboratory. One sample of the wafer was heated to 110 °C for 1 hour and the other sample was heated to 160 °C for 1 hour. The samples were cooled on a copper block immediately after being removed from the hot plates.

The transition from a transparent semiconductor to a reflective metallic state was observed at both temperatures when the samples were placed on the hot plates. The transition back to the semiconductor appearance was seen upon cooling. A permanent change in optical reflectivity was not visible. The XRR thickness measurements on the 110 ° hot plate were inconclusive; the thickness of the 160 ° sample was unchanged. The resistances of the samples were similar but about 2.5 times that of the control samples.

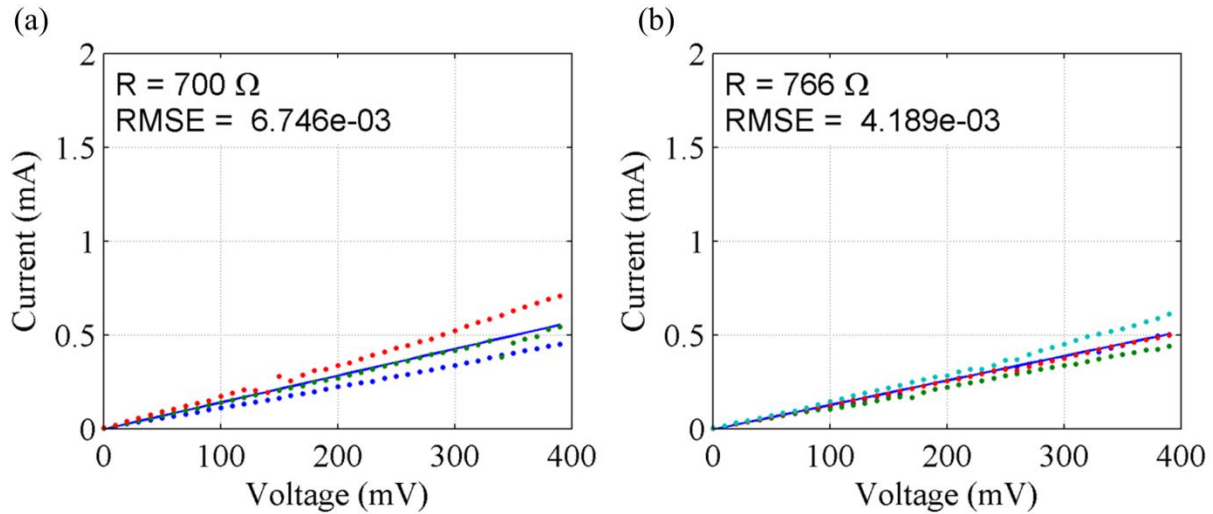


Figure 3.8: Voltage-current measurement at multiple locations across the sample heated to (a) 110°C and (b) 160°C. The solid line represents the linear regression results to the dataset, the slope of which is used to calculate the average resistance across the wafer.

### 3.2.6 NMP and Propylene-Glycol Solution

A lift-off process is frequently used to pattern gold contacts and transmission lines for VO<sub>2</sub> devices, such as those presented in this dissertation. During this procedure, the wafer is typically submerged in a beaker of 120°C NMP and propylene-glycol 1:1 solution. The NMP removes the nLOF2020 photoresist and any gold that was evaporated on top of it. The heightened temperature is necessary for removing cross-linked or hardened photoresist. Propylene-glycol is added to increase the flash point and the viscosity of the NMP.

Initial observations indicated the 120 °C NMP/propylene-glycol mixture was causing the VO<sub>2</sub> to chip off from or fully delaminate from the sapphire substrate. After processing initial test devices, all of the devices were found to be open circuits. Upon closer investigation, it appeared that no VO<sub>2</sub> remained after processing. Each step of the process was examined to determine the cause. The wafer was first imaged using SEM followed by EDX measurements. From these measurements, it was found that no VO<sub>2</sub> remained on the wafer where it had been exposed to NMP; however, there was VO<sub>2</sub> beneath the gold contact pads (Figure 3.9). This implies that the VO<sub>2</sub> was on the wafer when the processing began but was removed sometime after the gold deposition step.

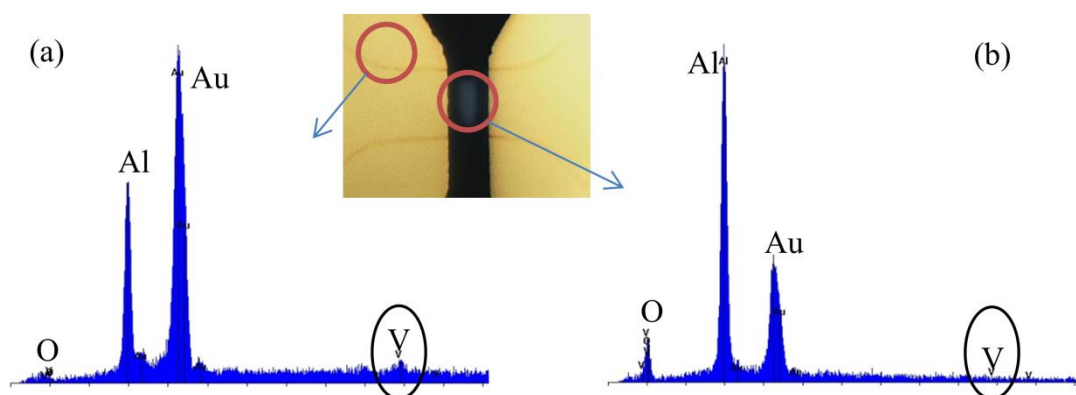


Figure 3.9: The EDX results for the area (a) under the gold contact pad and (b) between the pads. A vanadium peak around 5 eV is seen underneath the pads but is missing in the area between the pads. The Au that appears in (b) is from overlap onto the pads and the O is from the AlO<sub>2</sub> substrate. This indicates that the VO<sub>2</sub> bridge has been removed after the gold was deposited. The inset shows approximately where each EDX measurement was performed.

Using the experimental procedure described in section 3.2.4, an NMP/propylene-glycol mixture caused an 80% to 400% increase in voltage, depending on the specific sample and probe

location on the sample. The inconsistency in the change in resistivity indicates that the propylene-glycol or its combination with NMP is non-uniformly removing the  $\text{VO}_2$  from the sample.

The conditions to which the  $\text{VO}_2$  sample was exposed for this investigation are taken directly from the fabrication recipe with the exception of doubling the exposure time. A sample was placed in 1:1 NMP/propylene-glycol at 120 °C for one hour. The solution was agitated using a magnetic stirrer at 175 rpm. The film was then rinsed briefly under the faucet using DI water and dried with  $\text{N}_2$ .

The color of the sample changed from teal to pink. The sample thickness was 27 nm thinner than the control sample resulting in an etch rate of 4.5 Å/min (27 nm/hr). During liftoff procedure, the  $\text{VO}_2$  is exposed to the solution for 30-45 minutes which would etch the film 13 to 20 nm. The resistance of the  $\text{VO}_2$  film increased by tenfold. The NMP and propylene-glycol combination cannot be used with  $\text{VO}_2$  films.

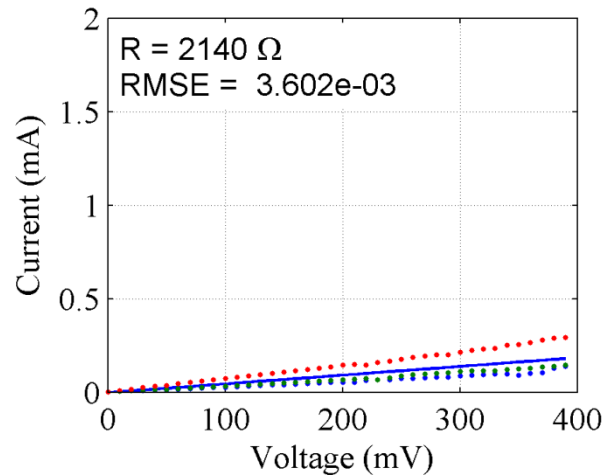


Figure 3.10: Voltage-current measurement at multiple locations across the sample exposed to NMP and propylene-glycol mixture. The solid line represents the linear regression results to the dataset, the slope of which is used to calculate the average resistance across the wafer.

### 3.2.7 N-Methyl-2-pyrrolidone (NMP)

NMP is the active ingredient in the NMP/propylene-glycol mixture. Straight NMP at 80 °C can be used as an alternative for liftoff procedure. In this process, the wafer is submerged in



agitated NMP for about 20 minutes then removed and swabbed with ethylene-glycol. The wafer is returned to the NMP for 10 minutes, followed by a second ethylene-glycol swab, returned to NMP for five more minutes, and subjected to a final swab. If the metal appears to have been completely lifted off, the wafer is rinsed under the faucet with DI water and dried with  $N_2$ . Initial measurements using the experiment discussed in the DI water section showed a repeatable 10% increase in voltage. For this investigation, the sample was placed in NMP at 80 °C for one hour. The solution was agitated using a magnetic stirrer at 175 rpm. It was rinsed under the faucet using DI water then dried with  $N_2$ .

The color of the NMP exposed sample became slightly less green than the control sample. The resistance and the thickness were not changed. The NMP without the propylene-glycol and at a lower temperature appears moderately acceptable as a solution for lift-off procedure, although exposure time should be limited.

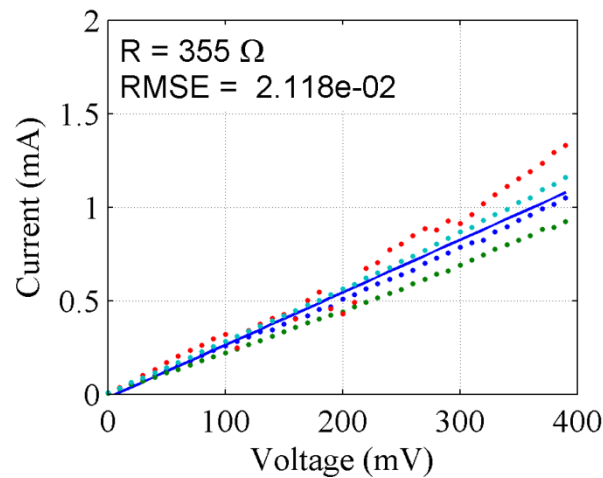


Figure 3.11: Voltage-current measurement at multiple locations across the sample exposed to NMP. The solid line represents the linear regression results to the dataset, the slope of which is used to calculate the average resistance across the wafer.

### 3.2.8 Photolithography

Photolithography is a multistep process used to pattern the device structure onto the wafer. The devices being fabricated are exposed to several different solutions and processes including the photoresist itself, elevated temperatures, ultraviolet light, developer, and DI water for rinsing. Each of these steps could potentially alter the  $VO_2$  film; however, changing any one

of the steps would involve changing the entire procedure thus they are included as a group in this investigation.

Many different photoresists and developers are commercially available. To test the effects of a typical photolithographic process on  $\text{VO}_2$ , a sample was processed using a procedure from the THz probe fabrication recipe (see appendix C). AZ nLOF2020 negative photoresist was spun onto the wafer at 4krpm for 30 seconds then baked at  $110^\circ\text{C}$  for one minute. The applied photoresist was flood exposed for 30 seconds at 320 nm and constant intensity of  $10.7 \mu\text{W}/\mu\text{m}^2$ . The nLOF2020 was developed using 300MIF for one minute at room temperature. The wafer was rinsed in two separate DI water beakers for 15 seconds each then dried with nitrogen.

The color of the processed sample was slightly more violet than the control samples. The thickness and the resistance were not changed significantly. Based on the visual results, it is possible that a step in the photolithography process and not the acetone was responsible for the preliminary results discussed in section 3.2.2.

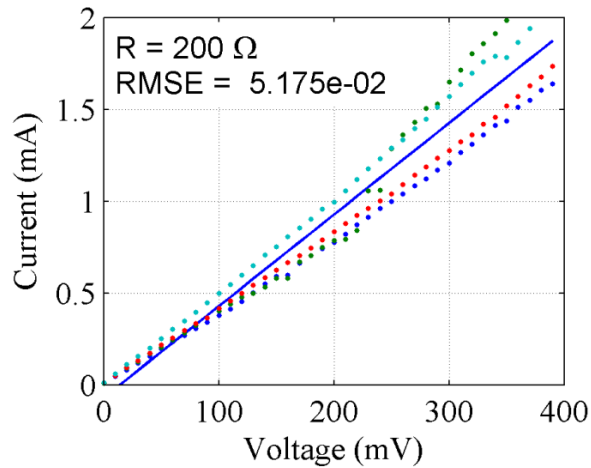


Figure 3.12: Voltage-current measurement at multiple locations across the sample exposed to nLOF2020 photolithography process. The solid line represents the linear regression results to the dataset, the slope of which is used to calculate the average resistance across the wafer.

### 3.3 Results Summary by Analysis Technique

The effect of the processes and reagents on the  $\text{VO}_2$  sample ranged from growing amorphous vanadium oxide to etching the film to not affecting the film. The thickness,

resistance, and appearance of each sample are described in Table 3.1. These results are expanded upon in the following sections.

Table 3.1: The thickness, resistance, and appearance of each sample after exposure.

Process	Thickness (nm)	Resistance ( $\Omega$ )	Appearance	Label
NMP+p-glycol	93	2140	Pink	K
DI H <sub>2</sub> O - 80 °C	106	290	Blue violet	M
Dicing	109	278	Teal	L
DI H <sub>2</sub> O - 21 °C	115	759	Blue violet	I
160°	115	766	Teal	H
nLOF2020 lith.	117	201	Blue violet	E
Dicing	118	266	Teal	R
NMP	123	356	Blue	F
Acetone	125	14043	Teal	C
O <sub>2</sub> Plasma Clean	125+27*	5873	Emerald	A
Dicing	119		Teal	G
Control	120		Teal	Control

\* This sample exhibits evidence of amorphous V<sub>2</sub>O<sub>5</sub> layer in XRR measurements.

### 3.3.1 Visual Results Summary

The first method for analyzing the results was visual observation. After processing, each 1 cm by 1 cm sample was arranged into a grid according to their pre-diced position in the wafer. Wafers exposed to NMP and propylene-glycol mixture and the O<sub>2</sub> plasma clean clearly changed color. When tilting the carrier, variations in the color of the other samples could be seen for the wafers exposed to DI water and to the lithography process. Figure 3.13a shows an optical photograph of the samples. The wafer was illuminated with a diffused light source at an approximately 45° angle while it was photographed using a Canon Powershot SD 1200 handheld digital camera held nearly perpendicular to the wafer in automatic mode. With the exception of the bottom row, the wafer colors in the photograph appear approximately the same color as when visually inspected. None of the samples from the bottom row were used in the experiment so their color swatches were not found. Figure 3.13b shows the average color for each sample. The color for each color swatch was found using the “color picker tool” in GIMP 2 (open source version of Adobe Photoshop). The spot size for selecting the color was chosen such that the

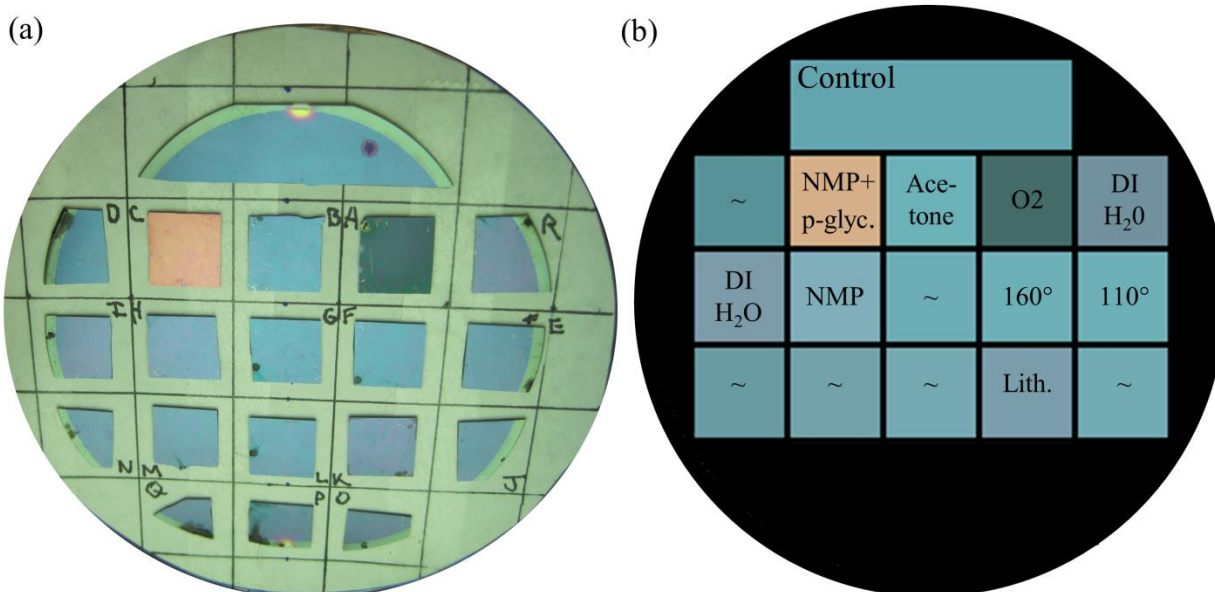


Figure 3.13: (a) An optical photograph of the samples. (b) The average color for each sample. The color swatches are placed in the corresponding location from (a). The labels indicate the process or reagent to which a given sample was exposed.

brush included 80% of a given sample. The brush size was adjusted slightly for the edge pieces to ensure that the brush included only the center portion of the sample. Using the biggest possible brush size ensures the “color picker tool” selects the average color over the entirety of a given sample. Unfortunately the iridescent appearance is lost in the photograph and particularly in the color swatches.

When comparing the color swatches, it can easily be seen that the NMP and propylene-glycol mixture turned the sample pink and the O<sub>2</sub> plasma clear turned the wafer a deep green color. The DI water and lithography process gave the samples a violet-hue while the other samples are more of a teal color. It was expected that the color would directly correspond to thickness, however, the thickness of the violet and teal samples were within error range from non-uniformity across the wafer (see section 0).

### 3.3.2 Resistance Measurements

The resistance of the samples varies from 201  $\Omega$  to 14 k $\Omega$  after exposure to the processes and reagents. Overall, the resistance does not appear to correlate with the thickness or the color

of the sample. The only exceptions are the samples exposed to NMP + propylene-glycol mixture and the  $O_2$  plasma clean. These wafers had an increase in resistance of more than one magnitude and had the most extreme change in appearance.

Variations in resistance across a wafer have been measured previously using a similar setup. The mean and standard deviation for the five measured currents at each voltage value were calculated. Additionally, the wafer used in this experiment was measured at seven locations prior to dicing and the mean and standard deviation calculated. These results are shown in Figure 3.14; the heavy, black, dashed line is the data from before dicing the wafer.

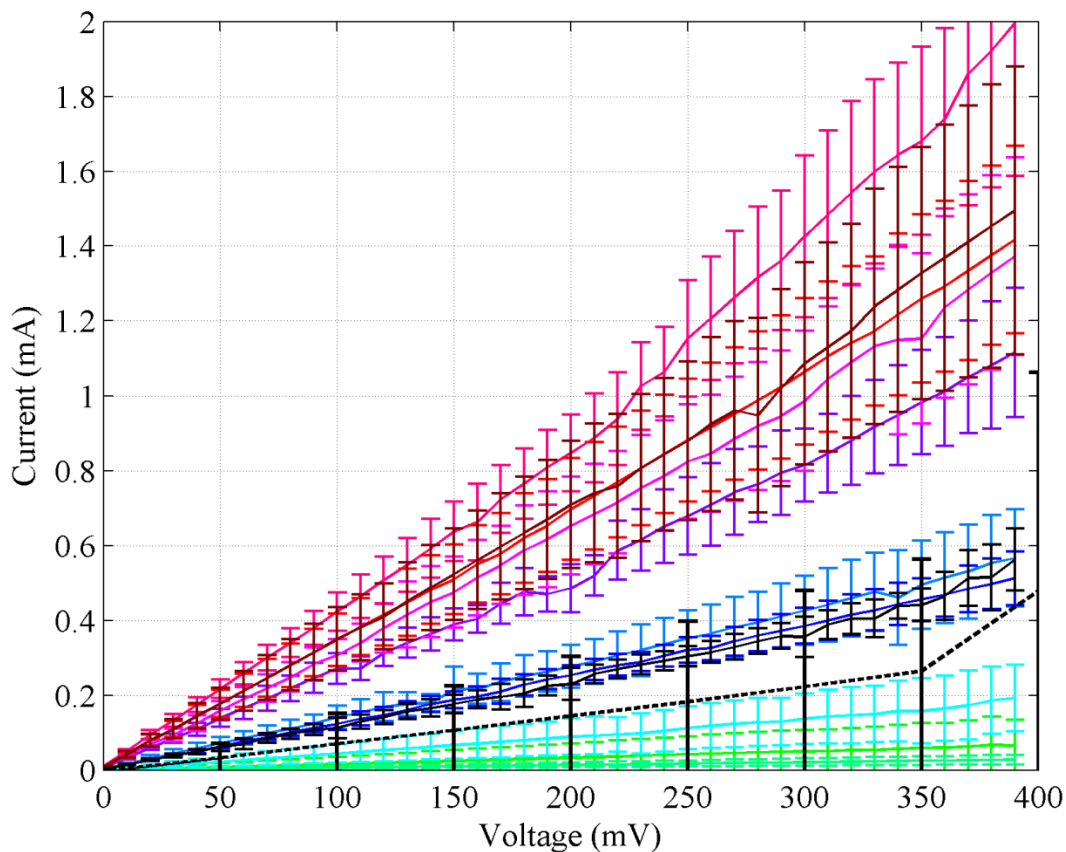


Figure 3.14: The mean and standard deviation of five current measurements across each sample. Each line indicates a different sample. The heavy, black, dashed line indicates the measurements made prior to dicing the wafer and performing the experiment.

### 3.3.3 VO<sub>2</sub> Film Thickness

After exposing each of the samples to a single fabrication process, the thicknesses of each sample and several control samples were measured (Table 3.1, Figure 3.15). The mean thickness for the three “dicing” samples and the “control” sample ( $n=4$ ) is  $116.5 \pm 5.1$  nm. The majority of the sample thicknesses lie within one standard deviation of the control mean. So, with the exception of the O<sub>2</sub> plasma cleaned sample, the NMP/propylene-glycol sample, and the 80 °C DI water sample, we cannot conclude that thickness of the VO<sub>2</sub> changed as a result of exposure to the various processes.

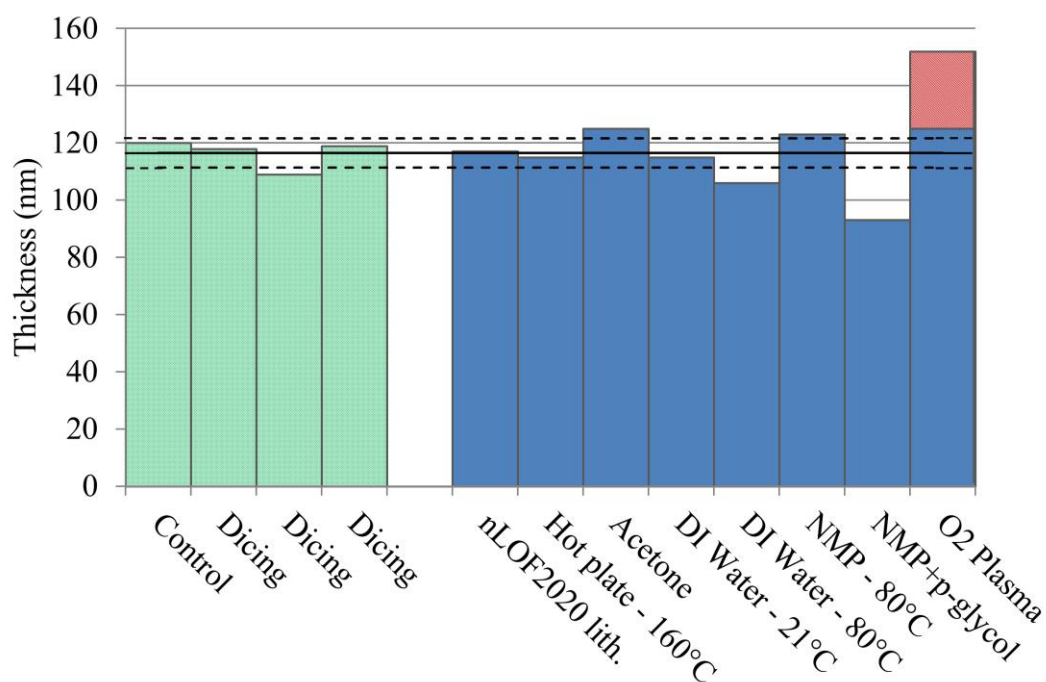


Figure 3.15: The thickness of each sample after exposure. The solid and dashed lines show the mean and one standard deviation of the mean for the control/dicing samples. The red square atop the O<sub>2</sub> plasma sample shows the vanadium oxide film grown from the VO<sub>2</sub> film.

### 3.3.4 XRD

XRD measurements (Figure 3.16) were performed on those samples that had a visible change in color along with two control samples (one pre-dicing, one post-dicing). The XRD results do not indicate the introduction of other strongly crystalline VO species, including the

sample exposed to the  $O_2$  plasma. However, this does not preclude the presence of the  $V_2O_5$  layer indicated in the thickness measurements. An amorphous film would have a broad peak as opposed to the sharper peaks seen in the results. Such a broad feature could be difficult to distinguish, particularly in the  $35$  to  $45^\circ$  range, and additional experiments would be needed to definitively conclude the presence of an amorphous vanadium oxide film.

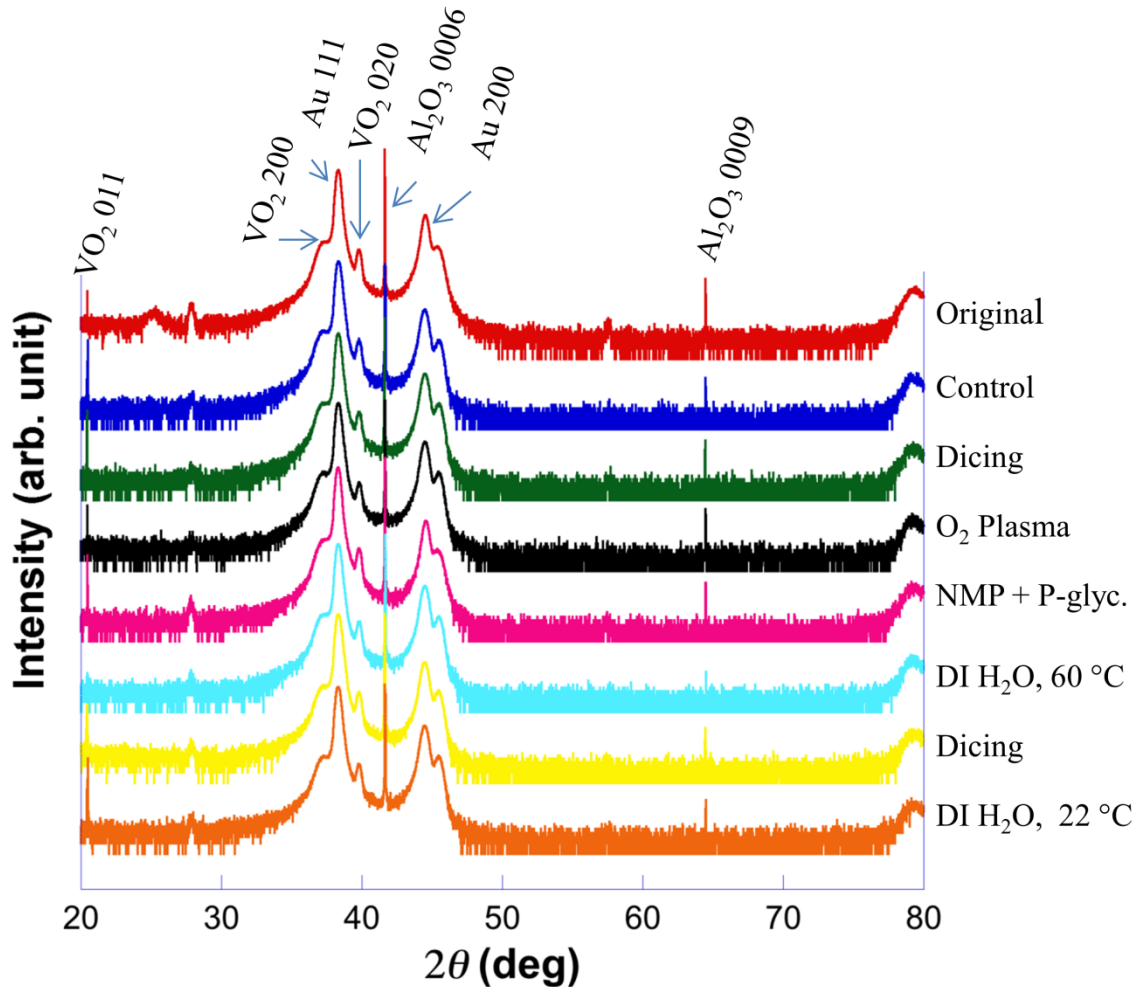


Figure 3.16: XRD for the  $VO_2$  samples that exhibited a visual change. “Original” is the data taken directly after the film growth. [Courtesy: Salinporn Kittiwatanakul]

### 3.4 Conclusions

The vanadium dioxide thin film is potentially etched or altered by several processes used during the fabrication of  $VO_2$ -based devices. Based on visual inspection, these processes include exposure to water and possibly photolithography. DI water at  $80^\circ C$  etched the  $VO_2$  film at a rate

of about 2.5 Å/min. NMP and propylene-glycol mixture etched the VO<sub>2</sub> film at a rate of about 4.5 Å/s. The O<sub>2</sub> plasma clean definitely changed the VO<sub>2</sub> film. XRD measurements did not reveal the growth of vanadium oxides aside from the VO<sub>2</sub> film; however XRR measurements suggest that an amorphous vanadium oxide film was grown during the O<sub>2</sub> plasma clean.

It is difficult to avoid some of the processes and reagents included in this experiment when fabricating a device. While developing a fabrication recipe, each process should be carefully considered even if it is commonly used. It is highly recommended that the VO<sub>2</sub> films be covered with an in-situ passivation layer prior to building the circuitry. If in-situ passivation is not available, the first fabrication step after the film growth should be a protective layer. Alternatively, the VO<sub>2</sub> could be deposited and patterned at the end of the fabrication procedure; however, this method would not protect it post-fabrication.

- [1] M. Mozetic, U. Cvelbar, M. K. Sunkara, and S. Vaddiraju, "A method for the rapid synthesis of large quantities of metal oxide nanowires at low temperatures," *Advanced Materials*, vol. 17, no. 17, pp. 2138–2142, 2005.
- [2] K. Martens, I. P. Radu, S. Mertens, X. Shi, L. Nyns, S. Cosemans, P. Favia, H. Bender, T. Conard, M. Schaekers, S. De Gendt, V. Afanas'ev, J. A. Kittl, M. Heyns, and M. Jurczak, "The VO<sub>2</sub> interface, the metal-insulator transition tunnel junction, and the metal-insulator transition switch on-off resistance," *Journal of Applied Physics*, vol. 112, no. 12, p. 124501, 2012.
- [3] I. E. Wachs and B. M. Weckhuysen, "Structure and reactivity of surface vanadium oxide species on oxide supports," *Applied Catalysis A: General*, vol. 157, no. 1–2, pp. 67 – 90, 1997.
- [4] W. Yin, K. G. West, J. W. Lu, Y. Pei, S. A. Wolf, P. Reinke, and Y. Sun, "The metal-insulator transition in vanadium dioxide: A view at bulk and surface contributions for thin films and the effect of annealing," *Journal of Applied Physics*, vol. 105, no. 11, p. 114322, 2009.



- [5] G. B. Stefanovich, A. L. Pergament, A. A. Velichko, and L. A. Stefanovich, "Anodic oxidation of vanadium and properties of vanadium oxide films," *Journal of Physics: Condensed Matter*, vol. 16, no. 23, p. 4013, 2004.

## Chapter 4: Characterization of Contact Resistance for Gold-VO<sub>2</sub> Thin Film Interfaces

Contact resistance plays a major role when designing a semiconductor device. As devices become smaller, the contact interface will account for an increasing portion of the device function [1] and have noticeable effect on its performance. Methods for measuring and quantifying the resistance between a metallic contact and a semiconductor material were developed in the 1960's to characterize these interfaces and are necessary for understanding and potentially reducing the contribution of the interface to device resistance. The method, known as the tlm, is widely used [2]; however, it is not always sufficient [3, 4]. In the past, tlm has been modified to address observations that were inconsistent with the assumptions in the model. In this chapter, one such observation regarding high TCR materials is presented, a modification to address this insufficiency presented, and results from the two methods are compared.

### 4.1 Introduction

Contact resistance refers to the interfacial resistance between a metal contact and the underlying semiconductor material; typically, contact resistance also includes contributions from the semiconductor region beneath the contact pads. In some devices, the contact resistance may be negligible while in other devices it may be a major contributor to the series resistance of the device. Methods for measuring the contact resistance are necessary for determining the extent to which this parameter influences device performance and for optimizing fabrication processes aimed at minimizing it. Understanding contact resistance is crucial in the design of high performance devices and measurement of this parameter can be used as a diagnostic to evaluate fabrication processes, as well as study material properties. Research into methods for reducing contact resistance has included studies of applying different contact metals or alloys [5], analyzing the effects of doping of the materials near the interface, or employing different fabrication processes, such as adding an ion clean prior to metal deposition. In this work, the most common approach for measuring contact resistance, known as the transmission line model

(tlm), was found to be unsuitable for characterizing the contact resistance in the vanadium dioxide – gold system. An underlying assumption of the tlm method is that the resistivity of the semiconducting material remains fixed during measurement. This is typically done using a fixed current bias and measuring the resulting voltage drop across pairs of contact pads. However, Joule heating of the material resulting from this bias current affects the temperature and resistivity of the film. Consequently, the resistivity varies with spacing of the contact pads. This issue is avoided by ensuring a fixed power density is dissipated within the material for all contact pad gap lengths. In this chapter, the tlm method is investigated, its shortcomings described, and a modification to the method based on dissipated power density is developed.

#### 4.1.1 Common Method for Measuring Contact Resistance

A method for measuring contact resistance and related quantities at the interface between a metal contact and a diffused layer in a silicon transistor was first described by Shockley in 1964 [6]. This analysis, known as the transmission line model (tlm), was later refined to characterize the ohmic contact resistance between metallic contact pads and semiconductor films (e.g. [7],[2]). In this chapter, the tlm is applied to evaluate the interface and contact resistance between a gold contact pad with a titanium adhesion layer and vanadium dioxide thin film grown on a sapphire substrate.

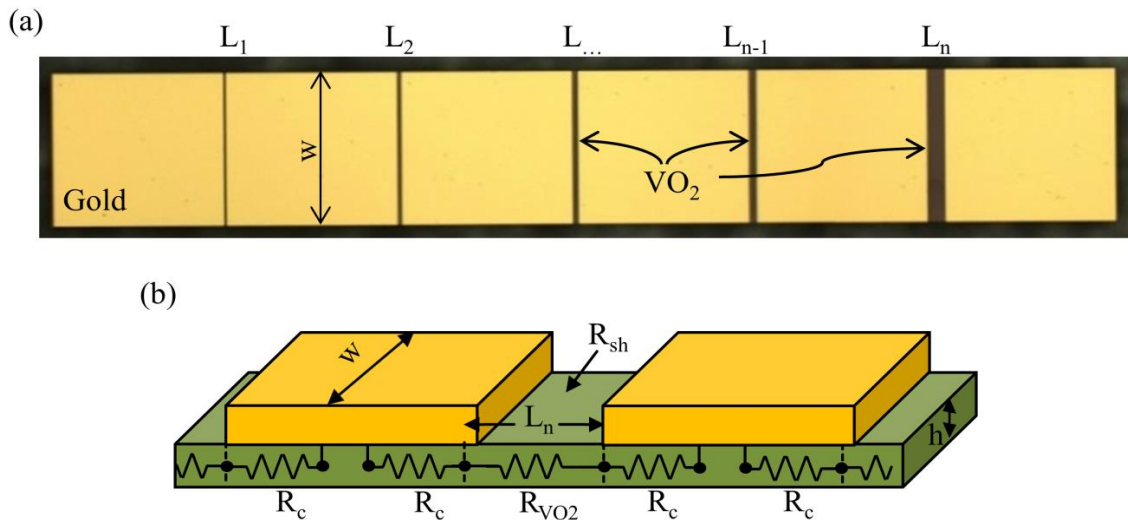


Figure 4.1: The contact measurement geometry. (a) A top view image shows a series of gold contact pads with varying spacing. (b) An oblique view sketch of a single contact gap.

Contact resistance and sheet resistance are directly calculated from a series of resistance measurements using a specific well-defined geometry. In the usual arrangement, a series of contact pads with increasing gap length are fabricated on a mesa of semiconducting material (Figure 4.1a, b). The resistance between each pair of adjacent contact pads is measured and plotted against the contact gap length (Figure 4.2). Contact resistance and semiconductor sheet resistance are directly calculated from the slope and y-intercept of a least-squares linear regression to the resistance-gap length data.

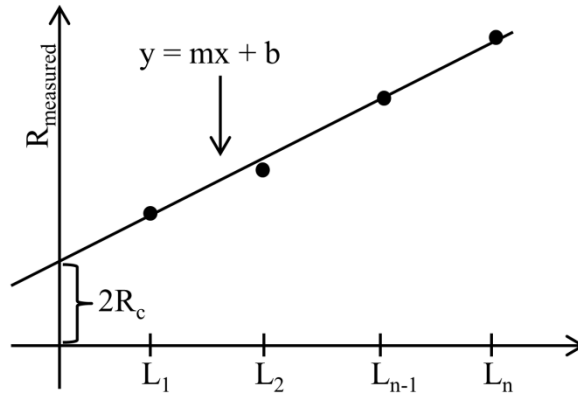


Figure 4.2: The measured resistance between adjacent contact pads is plotted as a function of the length between the pads and a line is fit to the data.

The measured resistance between two adjacent contact pads is composed of several factors: the interfacial resistance between the contact and the underlying  $\text{VO}_2$ ,  $R_i$ , the resistance of the  $\text{VO}_2$  underneath the contact,  $R_k$ , and the resistance due to the material between the pads,  $R_{\text{VO}_2}$  (Figure 4.3). The contact resistance,  $R_c$ , is the series combination of  $R_i$  and  $R_k$ .  $R_{\text{VO}_2}$  can be calculated from the sheet resistance,  $R_{\text{sh}}$ , of the  $\text{VO}_2$  between the pads with length,  $L$ , and width,  $w$  (Figure 4.3). The expression for the total measured resistance as a function of gap length,  $L$ , corresponds to the classic slope-intercept form of a line,  $y = mx + b$  (equation 4.1) [4].

$$R_m(L) = \frac{R_{\text{sh}}}{w} L + 2R_c \quad (4.1)$$

Using this relation, the sheet resistance of a  $\text{VO}_2$  film between contacts and the associated contact resistance can be experimentally determined [7].

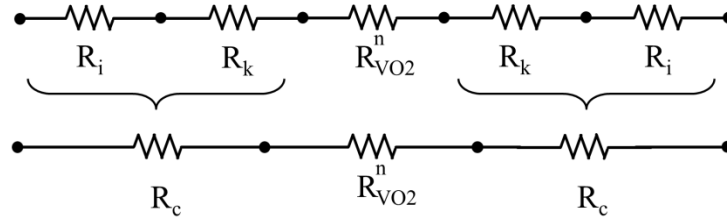


Figure 4.3 A circuit model corresponding to the geometry in Figure 4.2b.  $R_i$  is the interfacial resistance,  $R_k$  is the resistance of the VO<sub>2</sub> under the contact, and  $R_{VO2}$  is the resistance between the contacts.  $R_c$  is the series combination of  $R_i$  and  $R_k$ .

The volume of material between the contacts can be modeled as a slab of material with uniform resistivity,  $\rho$ , cross sectional area,  $A$ , and contact gap length,  $L$ . The expression to calculate the resistance of a rectangular slab of dielectric between two pieces of metal from the resistivity and the dimensions can be rearranged in terms of sheet resistance,  $R_{sh}$ , gap length,  $L$ , and width,  $w$  (equation 4.2). From the slope,  $m$ , of the linear fit to the resistance-gap length data, the sheet resistance can be calculated (equations 4.3a, b). In the limit that the gap length goes to zero, the contribution from the material between the contacts is removed and the remaining resistance is twice the contact resistance. Thus, the y-intercept,  $b$ , of the linear regression is directly proportional to the contact resistance (equations 4.3a, b) [6, 8].

$$R_{VO2} = \frac{\rho L}{A} = \frac{R_{sh}}{W} L \quad (4.2)$$

$$R_{sh} = m \cdot w, \quad R_c = \frac{b}{2} \quad (4.3a, b)$$

The specific contact resistance,  $\rho_c$ , is a normalization parameter that removes the dependence of the contact resistance on the size and shape of the contact pads (equation 4.4). It

$$\rho_c = \frac{(R_c w)^2}{R_{sh}} \quad (4.4)$$

is defined as the contact resistance in a unit area of current flow perpendicular to the contact and has units of  $\Omega\text{-cm}^2$  [8]. In the planar structure, the current is not uniform under the contacts. It decreases as distance from the contact edge is increased. A quantity known as the transfer length,  $L_T$ , (equation 4.5) is defined as the distance from the metallic edge to where the current drops by

$$L_T = \sqrt{\rho_c / R_{sh}} \quad (4.5)$$

$1/e$ , where  $e$  is Euler's number [6]. The specific contact resistance and transfer length as expressed in equations 4.4 and 4.5 are only valid if the sheet resistance of the VO<sub>2</sub> between the

contacts is equivalent to sheet resistance underneath the contacts [3]. An additional measurement is needed if the two sheet resistances are different (see section 4.3.3). The above analysis has several drawbacks. The contact resistance and sheet resistance depend on accurately measured contact spacing [8]. A change in spacing on the order of tenths of microns can change the calculated contact resistance result by tens of ohms or more. Moreover, the tlm as presented does not account for the possibility of the sheet resistance beneath the contact pads being different from that between the contacts [4]. Also, the resistance of the gold contact pads is integrated into the contact resistance value [3], the current may not be fully confined to or uniformly distributed within the area between the contact pads [3, 9], and the contact pad length is considered semi-infinite – a condition met only if the length of the pad is several times the transfer length [4]. The tlm has been modified in the past to address these shortcomings and a new modification is presented to better describe the vanadium dioxide - gold system.

#### **4.1.2 Application to Vanadium Dioxide**

Martens, et al. studied and characterized the  $\text{VO}_2$  interface [5]. They used a modified version of the tlm known as the circular transmission line model to measure the contact resistance between  $\text{VO}_2$  and several different metals (In, Ti, Al, Cr, Ni, Pd, and Au). Their  $\text{VO}_2$  was grown by oxidizing a vanadium layer and the metals were deposited with thermoresistive evaporation. Using the circular-tlm, their results showed that the specific contact resistivity or interfacial resistivity is dependent on the metal used to make the contact. Ti and Al have the best interfacial resistivity at  $10^{-6} \Omega\text{-cm}^2$  and Au and Pd have the worst values, approximately  $10^{-4} \Omega\text{-cm}^2$ . The results also showed that the interfacial resistivity is a function of the temperature of the material decreasing from  $3 \times 10^{-3} \Omega\text{-cm}^2$  at 223 K to  $4 \times 10^{-5} \Omega\text{-cm}^2$  as the structure is heated externally to the transition temperature (333 K) [5]. In their analysis, the temperature of the  $\text{VO}_2$  clearly affects the contact resistance.

## 4.2 VO<sub>2</sub> Film, Device Fabrication, and Measurement Procedure

### 4.2.1 Vanadium Dioxide Thin Film Deposition

Reactive Bias Target Ion Beam Deposition (RBTIBD) was used to deposit the VO<sub>2</sub> thin film onto a c-plane sapphire substrate [10]. For the film used in this study, the main chamber was pumped down to a base pressure of  $5 \times 10^{-8}$  Torr and the stage heater was ramped to 500 °C and allowed to stabilize for 45 min. The substrate was pre-cleaned using Ar ions and the vanadium target was sputter-cleaned by applying pulsed dc bias. Vanadium (99.99% purity) was sputtered in an 80/20 mixture of Ar and O<sub>2</sub> at a flow rate of 6.0 sccm, during which the pressure increased to approximately 1 mTorr. A deposition time of approximately 2 hours resulted in an 84 nm thick, single phase VO<sub>2</sub> film. The film was characterized after it was deposited but before the contact resistance structure was fabricated. The resistivity was measured as the temperature was increased from room temperature to 400K and back again (Figure 4.4a). The room temperature resistivity was 0.267  $\Omega$ -cm and the transition temperature was 340K. An XRD of the VO<sub>2</sub> film shows that it is single phase VO<sub>2</sub> (Figure 4.4b). The Al<sub>2</sub>O<sub>3</sub> in the XRD is the substrate.

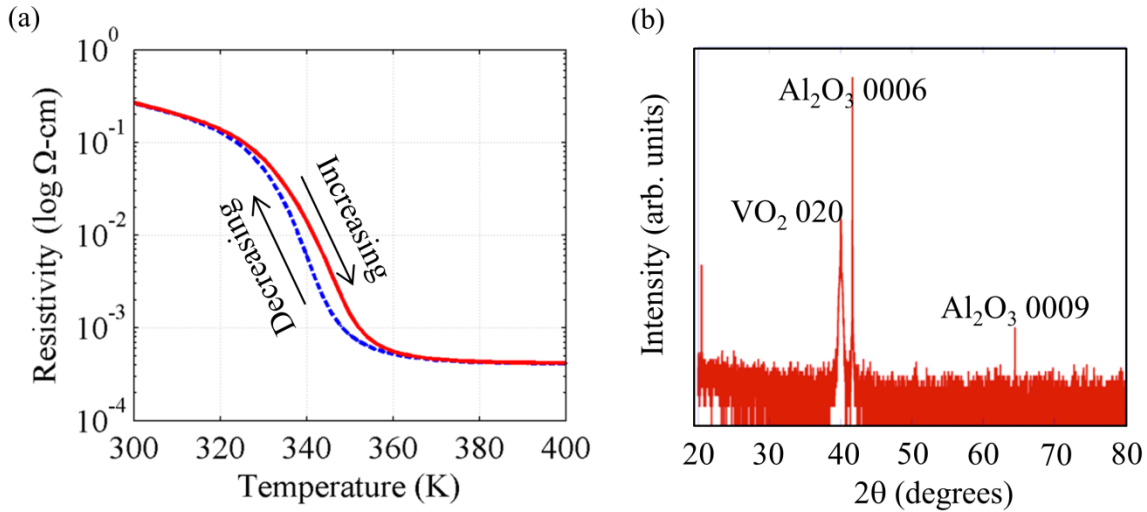


Figure 4.4: (a) Resistivity-temperature plot and (b) XRD of the VO<sub>2</sub> film. [Courtesy: Salinporn Kittiwatanakul]

### 4.2.2 Fabrication of Contact Resistance Test Structures

Structures for measuring contact resistance were fabricated in two lithographic steps. Contact pads were patterned using negative photoresist, nLOF2020, and UV lithography. After exposure, the device was developed in MIF300 and the residual resist was removed in an  $O_2$  plasma operating at 120W for 10 minutes. An electron-beam evaporation system was used to deposit a 10 nm thick titanium adhesion layer followed by an in-situ 150 nm thick gold layer. Liftoff was performed using an 80°C NMP soak followed by an ethylene-glycol swab forming the metallic contact pads. The  $VO_2$  mesa was patterned using positive photoresist, AZ4110, and developed in AZ400k:H<sub>2</sub>O 1:4. The  $VO_2$  was etched using a 4:40 sccm SF<sub>6</sub>:Ar RIE at 30 mTorr, 50W ICP, and 20W RIE for three minutes. The resist was removed with an  $O_2$  plasma clean at 120W for two hours. The device was inspected in an optical microscope and scanning electron microscope (SEM) for irregularities or inconsistencies (Figure 4.5).

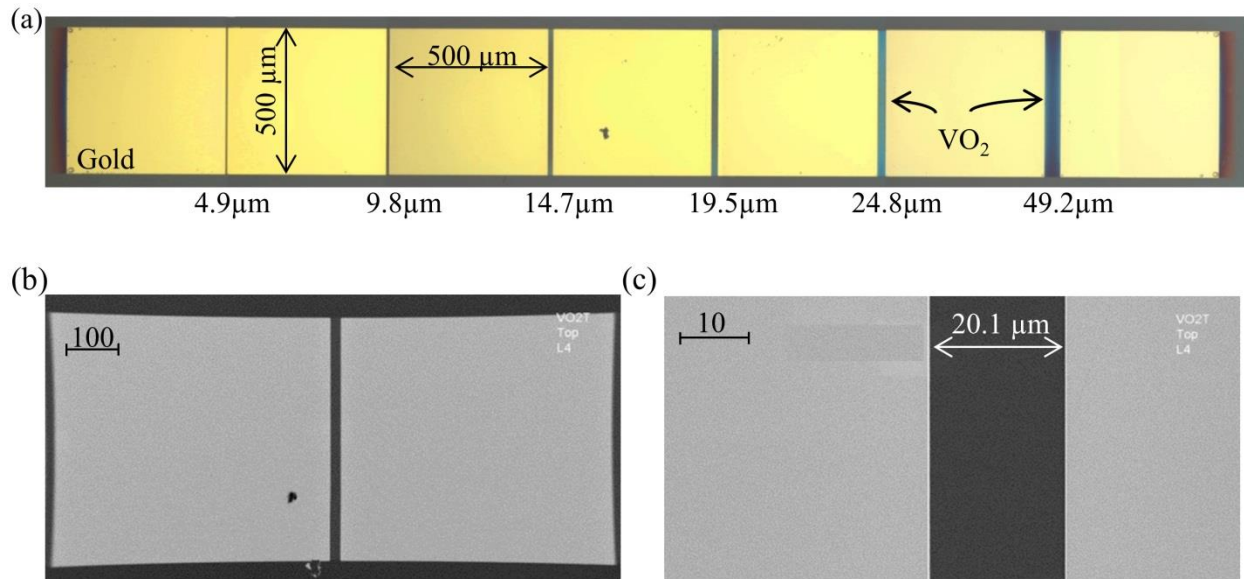


Figure 4.5: (a) An optical image of a contact resistance measurement device. The six pads are separated by increasing lengths. The  $VO_2$  extends past the ends of the device by 50 μm on each side and is flush on the top and bottom of the contacts. (b) An SEM of two contact pads and the gap between them. The slightly oblique shape is an artifact of the SEM and not real. (c) A higher magnification of the gap used to inspect the quality of the contact pad edges.



### 4.2.3 Pad Geometry and Characterization

The contact resistance structure consists of seven  $500 \times 500 \mu\text{m}$  contact pads on a  $\text{VO}_2$  mesa. The gap lengths between contact pads are nominally designed to be 5, 10, 15, 20, 25, and  $50 \mu\text{m}$ . The  $\text{VO}_2$  mesa is  $500 \mu\text{m}$  wide by  $3635 \mu\text{m}$  long (Figure 4.5). The final dimensions are within  $1 \mu\text{m}$  of the design values.

An exact measurement of the contact pad gap length is required to accurately calculate contact resistance and related values. The gap lengths were measured after fabrication and before the resistance measurements; the design values are not accurate enough. A change in gap length on the order of tenths of microns can result in a change in contact resistance of tens of ohms. SEM was used to measure the gap lengths at higher magnification. The most repeatable measurements were performed using a tool in the SEM software suite that plots the pixel intensity along a given line (Figure 4.6). At the edge of the contact pads, the pixel intensity drops abruptly. The gap length is designated as the distance between these two abrupt changes in pixel brightness.

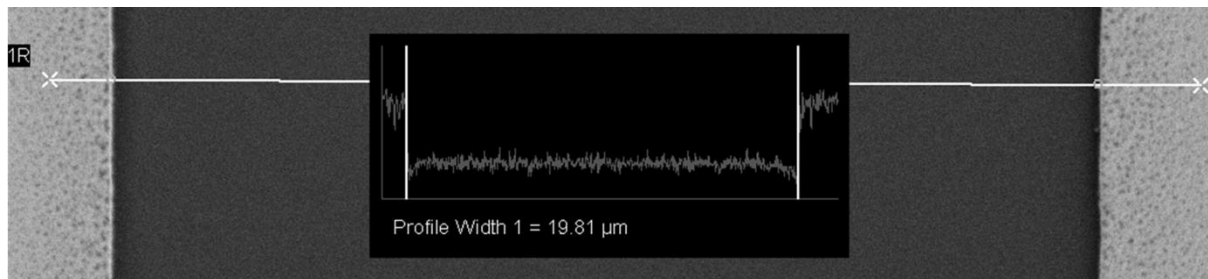


Figure 4.6: Measurement of the gap length using the pixel intensity along a drawn line on an SEM image to determine the edge of the contact pad.

### 4.2.4 DC Measurement System

DC resistance measurements on the samples were performed using a Keithley 236 source-measure unit (SMU) attached to a four point probe setup. Each probe was attached to a micromanipulator that could be moved independently. All measurements were performed by sourcing current and sensing voltage. The SMU was operated in “linear staircase” mode with an “on” time of 400 ms and an “off” time of 22ms as determined by the speed of the instrument.

Pulses were used to reduce the effects of device heating on the measurements. Each sweep had a maximum of 1000 data points or 500 “on” data points as a result of the Keithley’s memory capacity. The unit was setup, operated, and data collected using a customized NI LabView program. Each device required a set of six measurements. The source range was constant for all six measurements regardless of the transition current value. After each sweep, the probes were moved to the next set of contact pads during a one minute delay. The data was plotted and inspected for anomalies. Anomalies include an open circuit or short circuit, a sudden increase in voltage to compliance level, or an outlier. If an anomaly was found, the anomalous region was visually inspected for damage (see appendix A), an uneven contact edge, or fabrication error (e.g. a gold flake in the region between the pads) and the data was rejected. The “off” or 0 bias points were removed from the data sets before performing the calculations. A sample dataset is shown in Figure 4.7.

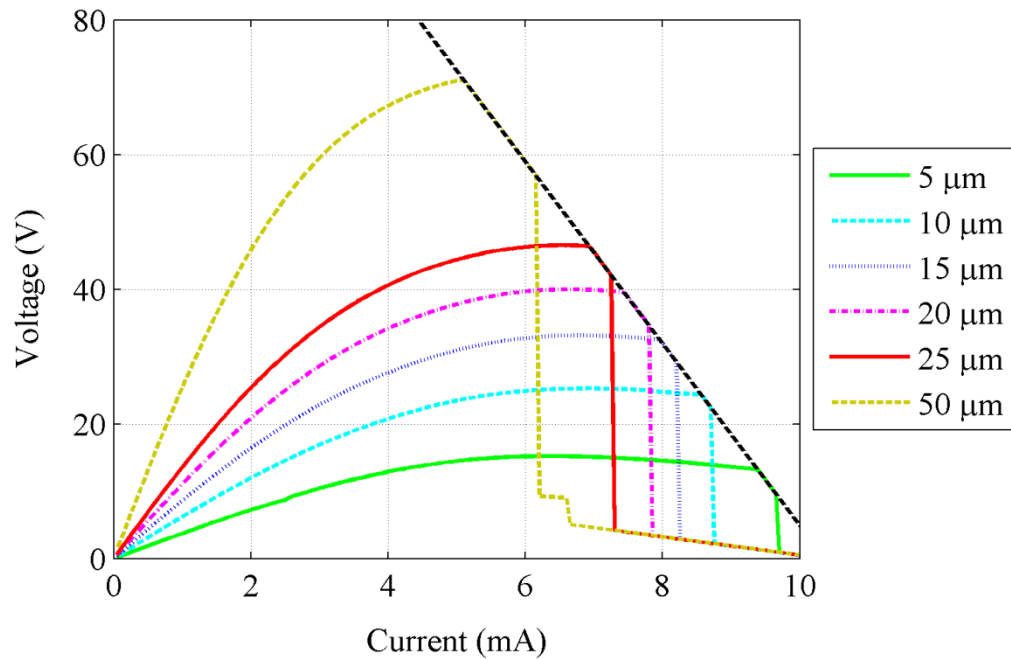
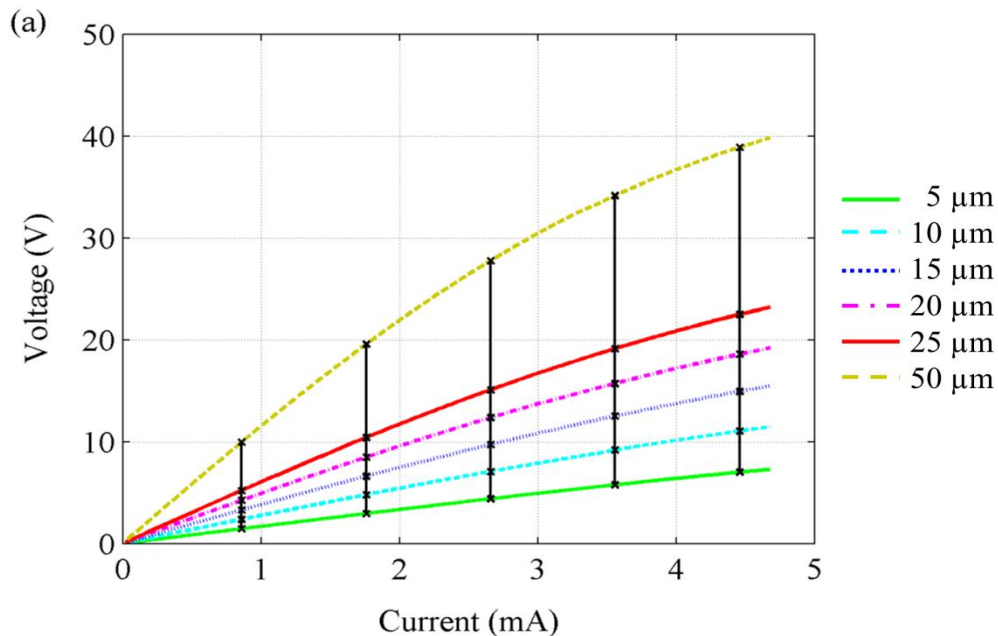


Figure 4.7: A sample contact resistance measurements dataset. The black, diagonal, dashed line connects the transition points for each gap length.

### 4.3 Development of a Modified Method for Measuring Contact Resistance

#### 4.3.1 Standard Method

In the standard method for characterizing contact resistance, the resistance across each gap is measured using a single, low value bias point. In this study, the devices were measured at multiple biases allowing the contact resistance and sheet resistance to be calculated across a range of values (Figure 4.8a). The resulting resistance-length plots contained several interesting features (Figure 4.8b). The first observation was the decrease in slope as the current bias was increased. This result is intuitive in that the slope is proportional to the vanadium dioxide sheet resistance, which decreases with increasing current. Second, the best fit lines to the data all intersected at a single point corresponding to a gap length of several microns. It was hypothesized that the intersection point was the contact resistance and it was shifted from the resistance axis as a result of the volume of the active region being different from the volume between the contact pads. Finally, the intercept point on the resistance axis increased with increasing current. If this pattern were to hold true for smaller current bias values, the resulting contact resistance could become negative, a nonphysical result.



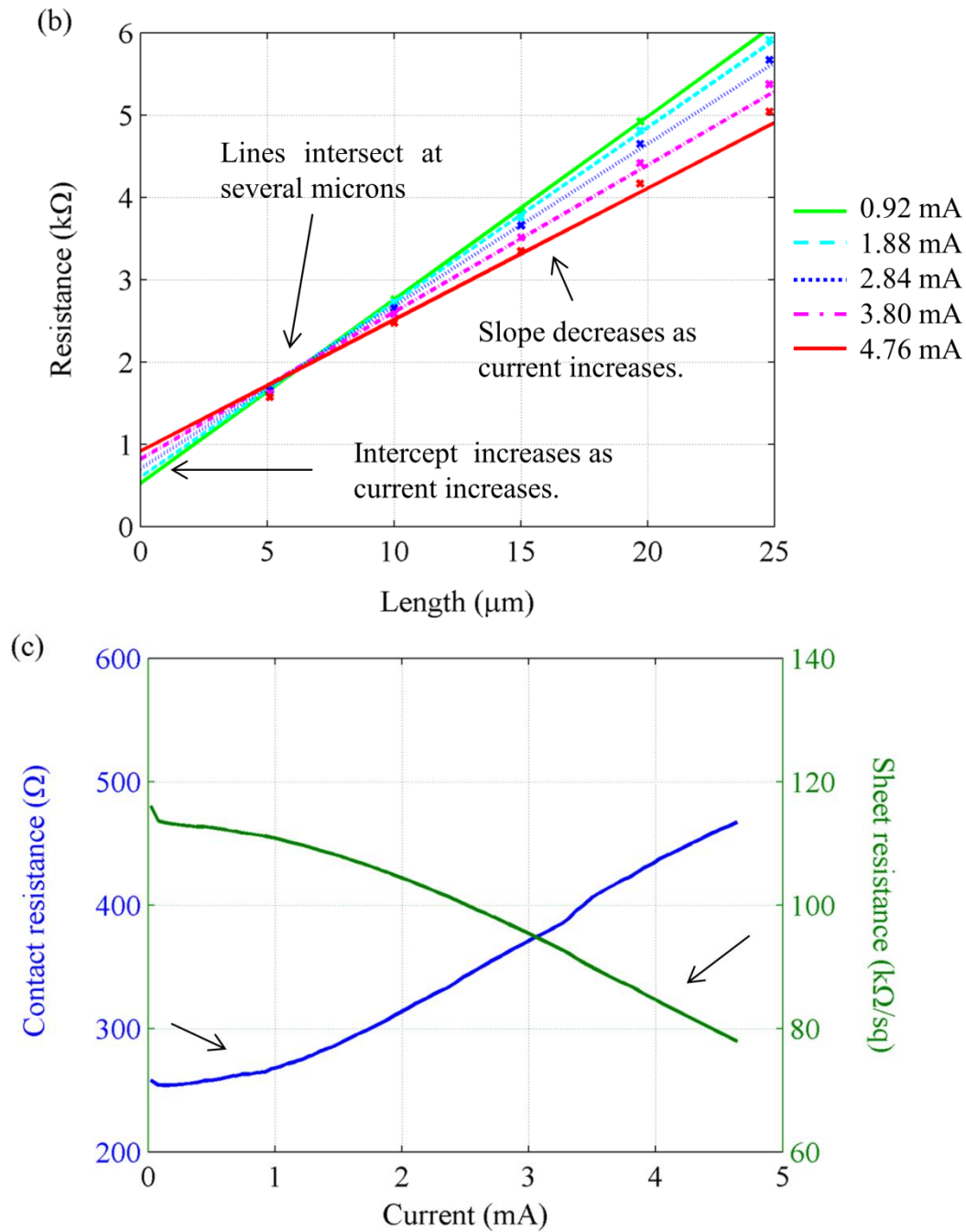


Figure 4.8: (a) The raw IV data with superimposed lines of constant current. (b) A resistance-length plot from the constant current with points of interest highlighted. At least fifty different current values are used for the calculations but only five are plotted for clarity. (c) The contact resistance and sheet resistance as calculated using the constant current method.

### 4.3.2 Constant Power Density Method

The method described in the previous section employs a fixed current and extracts the contact resistance from sensing the voltage induced across pairs of contact pads. This is done for all contact gap lengths. With a fixed current, pairs of pads with shorter gap lengths and, therefore, smaller volume will dissipate less power (and be at a lower temperature) in the vanadium dioxide film than pairs of pads with longer gaps. Lee et al. [11] have shown the heat flow across a  $10\text{ }\mu\text{m} \times 10\text{ }\mu\text{m}$   $\text{VO}_2$  film with Au/Cr electrodes for time scales of 10-50  $\mu\text{s}$ , a limit imposed by the speed of their infrared detector. Their data and subsequent modeling show that the temperature distribution is not uniform for the timescales used for data collection in this analysis [11]. Moreover, infrared images of a  $4\text{ }\mu\text{m} \times 4\text{ }\mu\text{m}$  section of the  $\text{VO}_2$  film showed the percolation of metallic regions at temperatures near the transition region [12]. As the temperature of the sample was increased from 341K to 343.6K using an external heat source, the formation of metallic regions was imaged (Figure 4.9) [12]. Regions with a higher temperature have a higher ratio of metallic region to semiconductor region.

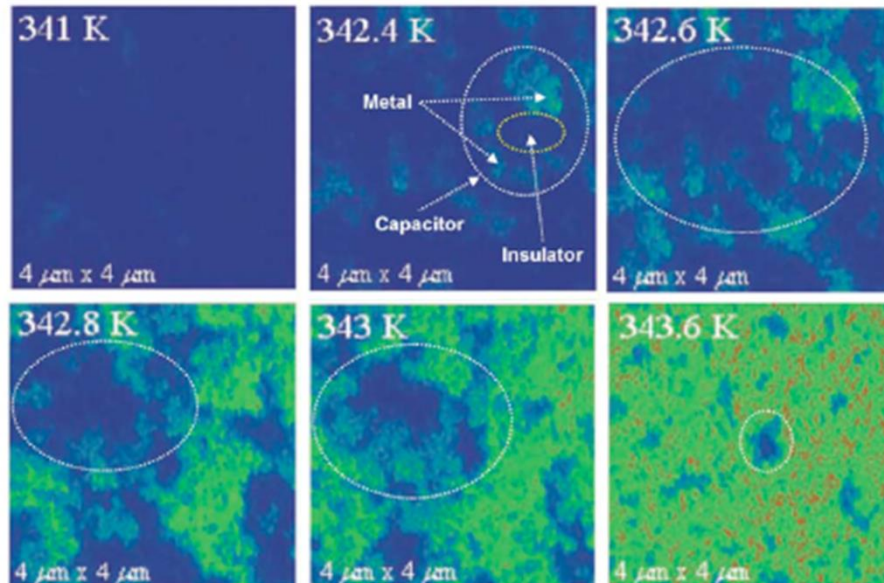
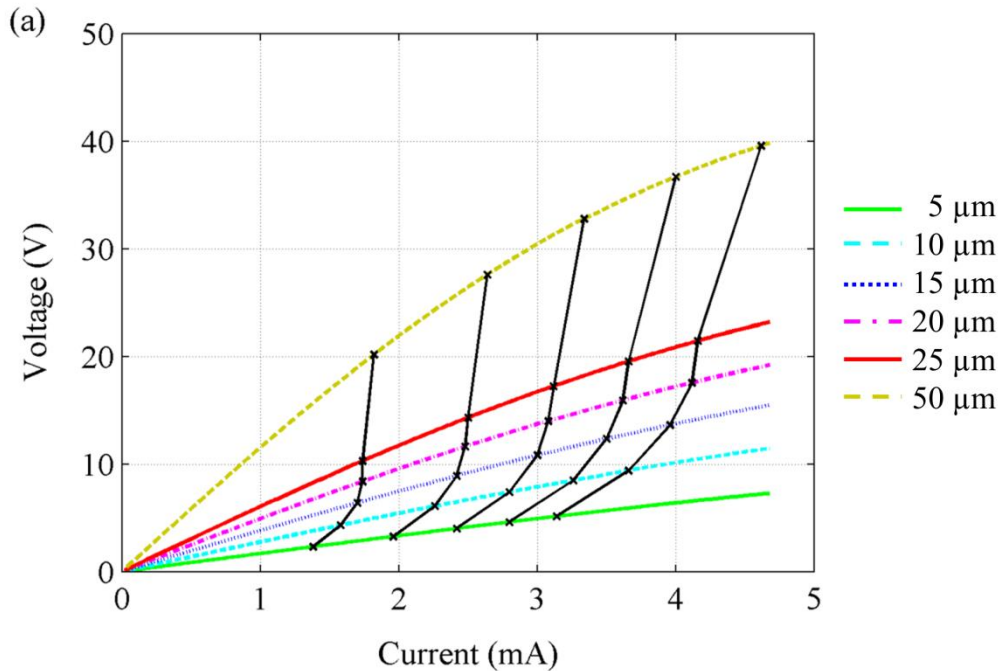


Figure 4.9: Midinfrared near field image showing the percolation of metallic regions with increasing temperature. The 341K image in the upper left is mostly in the insulating state (blue) while the 343.6K image in the lower right is mostly in the metallic state (green) [12].

The temperature of the VO<sub>2</sub> film for longer gap lengths is higher than the temperature for shorter gap lengths. The VO<sub>2</sub> nearer the contact pads is most likely cooler than the VO<sub>2</sub> farther from the contact pads as a result of the contacts acting as heat sinks. For a longer gap length, there are regions of VO<sub>2</sub> that are farther from the pads than for the shorter devices. Thus, as gap length increases, the ratio of metallic to semiconductor regions in a given gap at a given current is increased. Using a fixed dissipated power density instead of a constant current provides a method to select regions that have similar semiconductor to metallic region ratios.

Curves of constant dissipated power density are superimposed on the IV data to illustrate this selection method (Figure 4.10a). The dissipated power density is calculated using only the volume of VO<sub>2</sub> between the contacts. At a given power density the smallest current corresponded to the shortest spacing and the highest current to the longest spacing. It is expected that at a given power density the current would be higher for the shortest gap just as the shortest gap has the highest critical current value (see black, dashed line in Figure 4.7). This implies that the dissipated power density is not accurately determined for this system. Furthermore, the point of intersection on the resistance-length plot remained nearly unchanged (Figure 4.10b). Considering only the volume between the contacts when calculating the dissipated power density is insufficient.



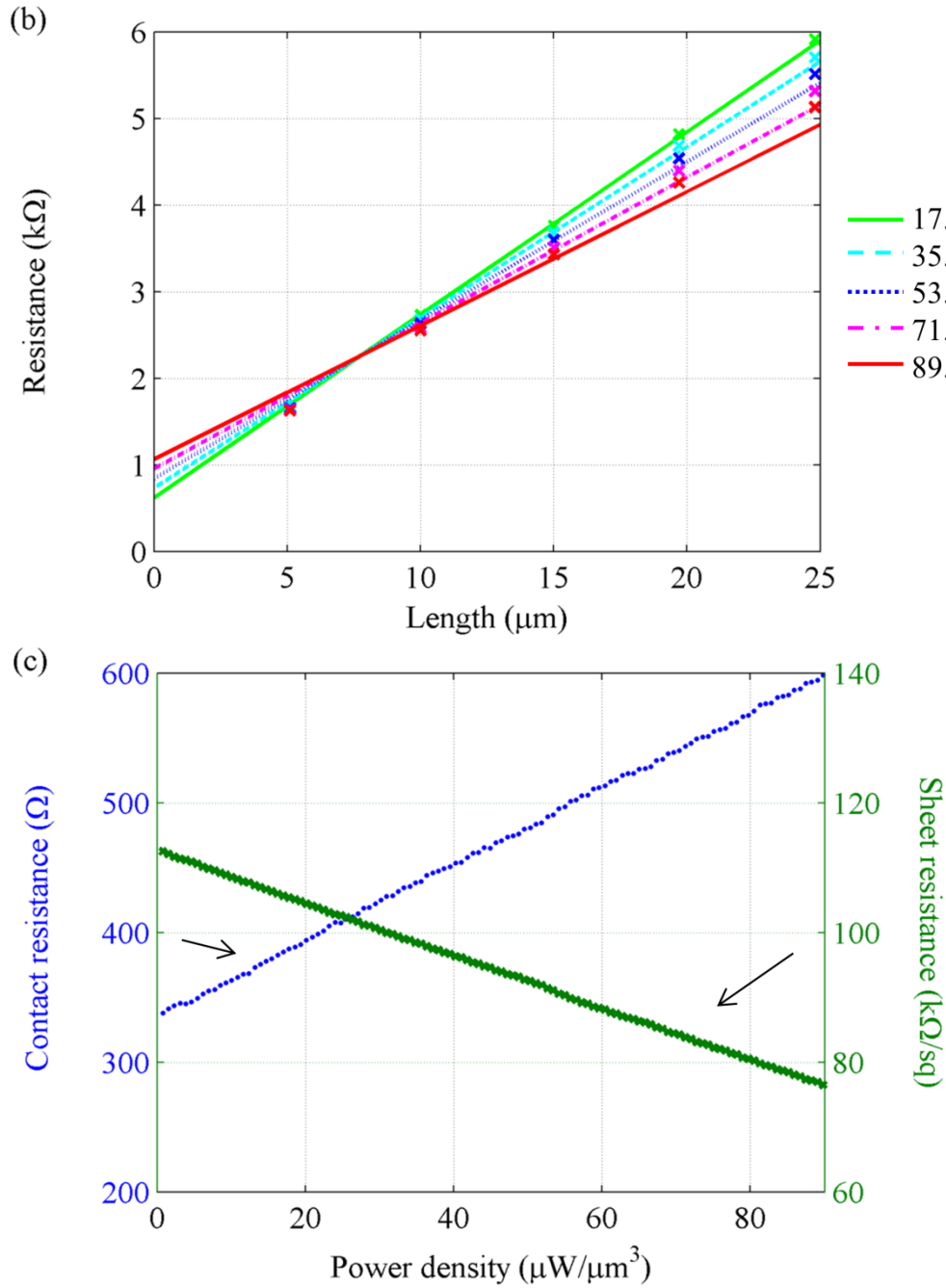


Figure 4.10: (a) The IV data with several superimposed lines of constant dissipated power density as calculated for the volume between the contact pads. (b) A resistance-length plot using the data from (a). At least fifty different power densities are used for the calculations but only five are plotted for clarity. (c) The contact resistance and sheet resistance.

### 4.3.3 Incorporation of the Transfer Length

Finding resistance as a function of gap length for a constant dissipated power density accounts for the effects of Joule heating normalized over the device volume. Note that power is dissipated not only in the space between the contacts, but also for some volume underneath the pads. From the transmission line model, the transfer length,  $L_t$ , describes the length under the pad at which the current drops by  $1/e$  of its maximum value. This parameter is generally small in comparison to the pad dimensions [2]. The power density selection method described in the previous selection was further modified to include the transfer length when calculating the volume for the power density calculation (equation 4.6). In equation 4.6,  $I$  is the current bias,  $V$  is

$$P_D = \frac{IV}{wh(L + 2L_t)} \quad (4.6)$$

voltage measured across the contacts,  $w$  is contact pad width,  $h$  is the  $\text{VO}_2$  thickness,  $L$  is the length between the pads, and  $L_t$  is the transfer length. It should be noted that equation 4.6 assumes that the current under the contact is uniform, which is not true from the base definition of transfer length. However, transfer length is a previously defined concept and provided a strong starting point for modifying the power density method.

When the sheet resistance of the semiconductor under the contact pad is the same as the sheet resistance between the pads, the transfer length is one half the  $x$ -axis intercept of a resistance-length curve [4]. Using this definition and the resistance-length curve for the lowest current bias data, a transfer length of  $1.5 \mu\text{m}$  was calculated. This value increases with increasing current but does not exceed a few microns. This small value shifts the intersection on the resistance-gap length plot by less than  $1 \mu\text{m}$  toward the resistance axis but otherwise does not noticeably alter the resistance-length linear regression results. Moreover, the sheet resistance under the contact pads,  $R_{sk}$ , is different from the sheet resistance between the contacts,  $R_{sh}$  (see section 4.3.4).

When the sheet resistance under and between the contacts is not constant, an additional quantity known as end resistance is required to determine  $L_t$  [4]. The end resistance (Figure 4.11a) is defined as the voltage at the end of the contact ( $x = d$ ) divided by the incoming current



at the front of the contact ( $x = 0$ ) when  $I(d) = 0$  [2]. End resistance can be found by measuring the resistance between two non-adjacent contacts [4] and subtracting it from the sum of the resistance across each pair of adjacent contacts (equation 4.7, Figure 4.11b).

$$R_E = \frac{1}{2}(R_1 + R_2 - R_3) \quad (4.7)$$

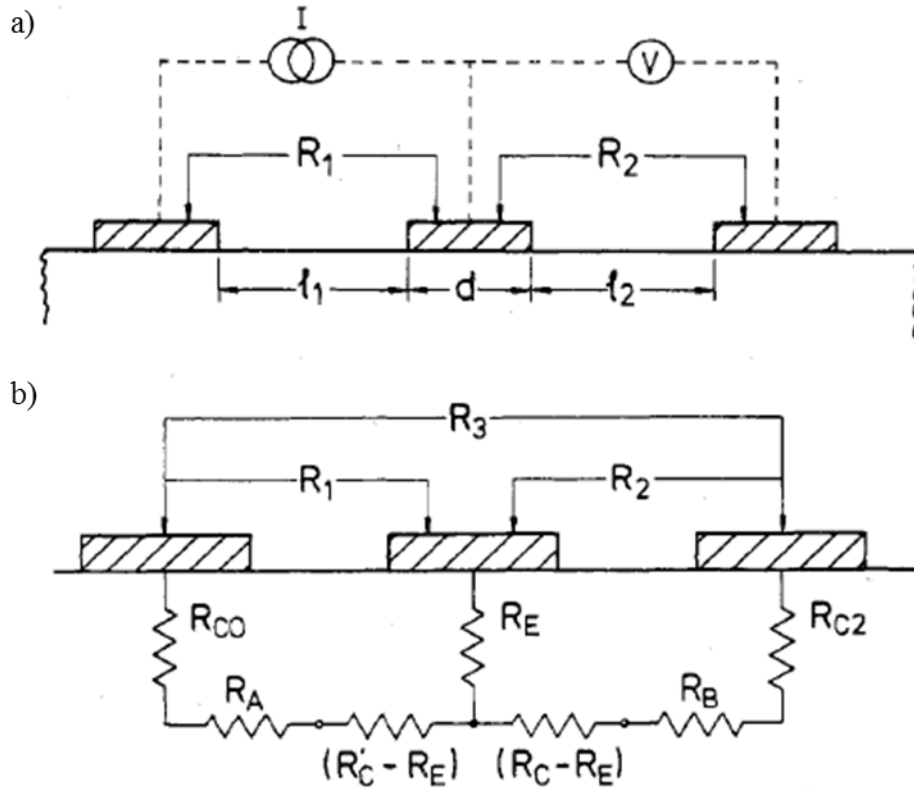
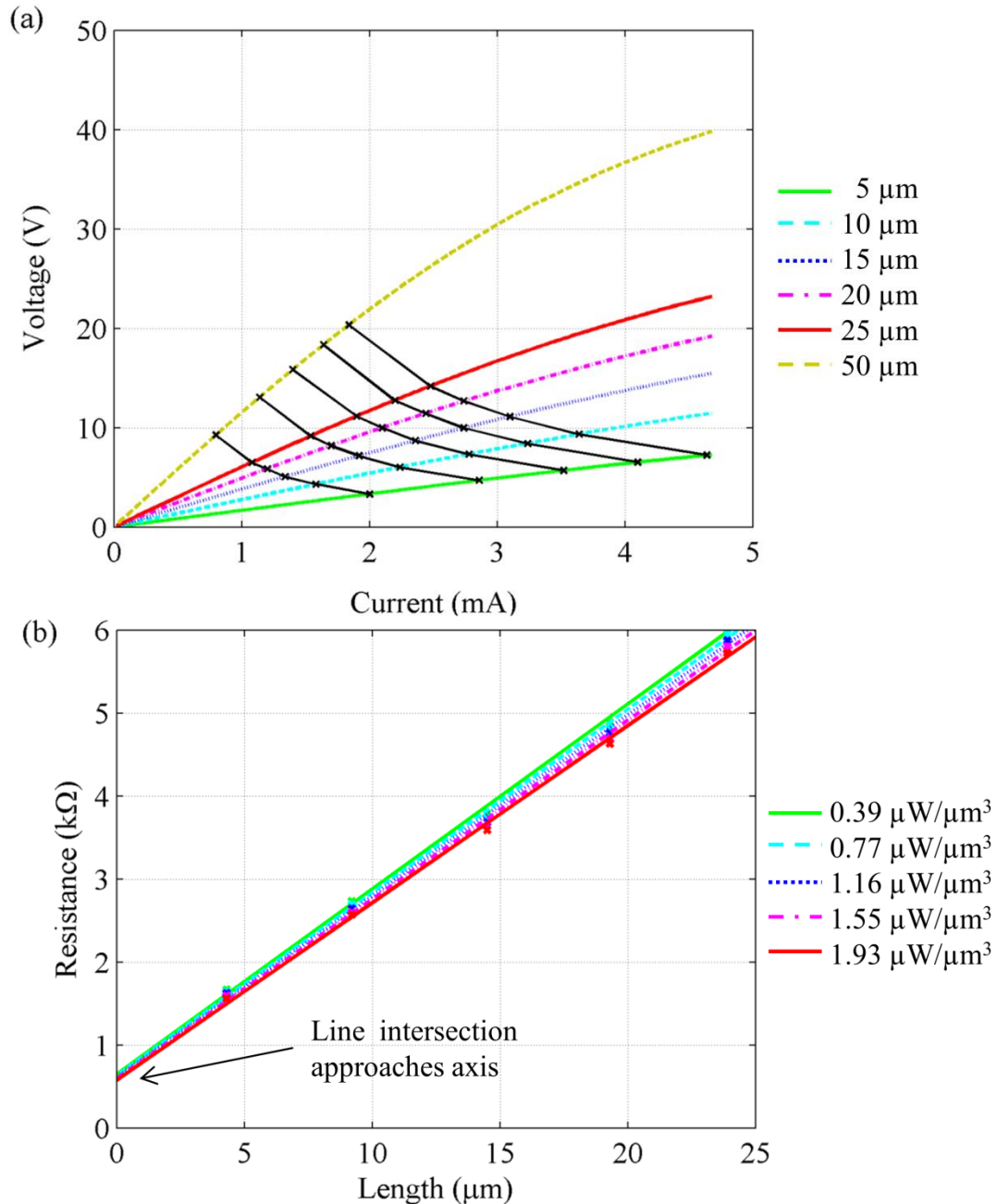


Figure 4.11: (a) A diagram illustrating the definition of the end resistance. (b) A diagram showing the three measurements needed to calculate the end resistance [4].

For the contacts studied in this work, the end resistance measurements for different pairs of contacts were inconsistent and resulted in both negative transfer lengths and transfer lengths exceeding the size of the contact. For lack of a better method, the measured values were averaged and the mean value of  $203 \mu\text{m}$  was used.

Recalculating the power density using a transfer length of  $203 \mu\text{m}$  moved the point of intersection on the resistance-length plot nearer to the resistance-axis (Figure 4.12b). Moreover, it changed the concavities of the power density curves superimposed on the IV from left facing to right facing (Figure 4.12a). The transfer length results showed the importance of including the power being dissipated underneath the pads. However, the transfer length calculations were not

consistent and comprise 40% the contact pad lengths, a violation of the assumption that  $d \gg L_t$  used when deriving  $t_{lm}$  [2]. Additionally, the end resistance is a function of power density, which is not taken into account. Lastly, the transfer length method is recursive. The transfer length calculation relies on the slope of the resistance-length data. It has already been shown that the slope decreases with increasing power density. A single sheet resistance and therefore slope is needed to calculate the transfer length. In this calculation the lowest current bias data was used.



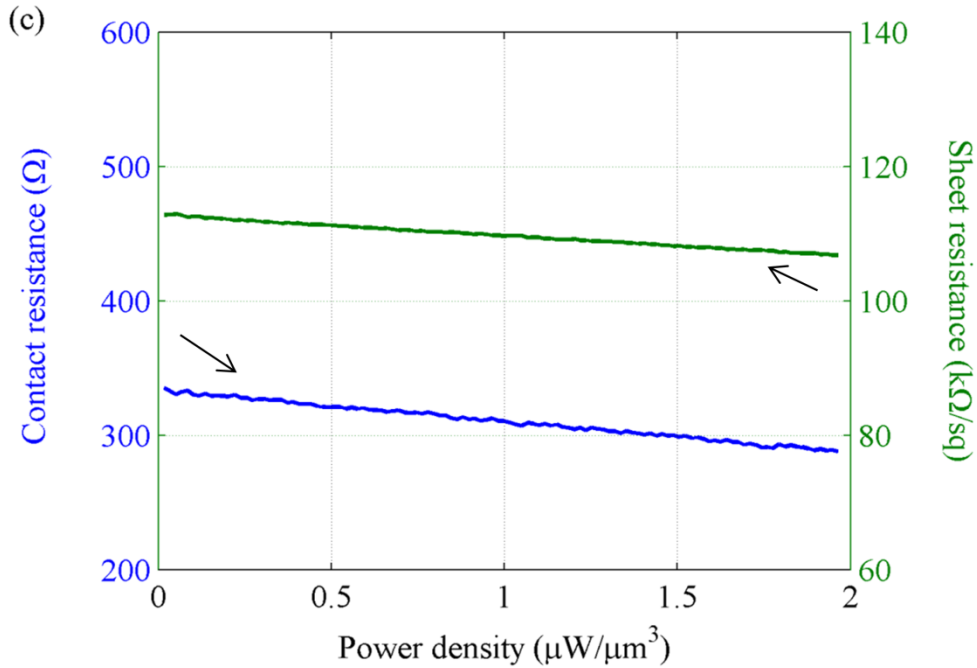


Figure 4.12: (a) The raw IV data with several superimposed lines of constant dissipated power density as calculated using the volume between the contacts and the volume under the contacts and within the transfer length. (b) A resistance-length plot using the data from (a). At least fifty different power densities are used for the calculations but only five are plotted for clarity. (c) The contact resistance and sheet resistance.

#### 4.3.4 Effective Volume Method

The inconsistent transfer length and discussed drawbacks in the previous sections pointed to the need for a different method to determine the effective volume under the contact pads in which the power is dissipated. A criterion that the contact resistance is independent of power density was applied to find an effective volume that is represented by an effective lateral distance under each pad,  $x$  (Figure 4.13). This criterion can be justified by noting that the transition in  $\text{VO}_2$  is thermally driven via Joule heating but the large gold contact pads and probe tips act as a

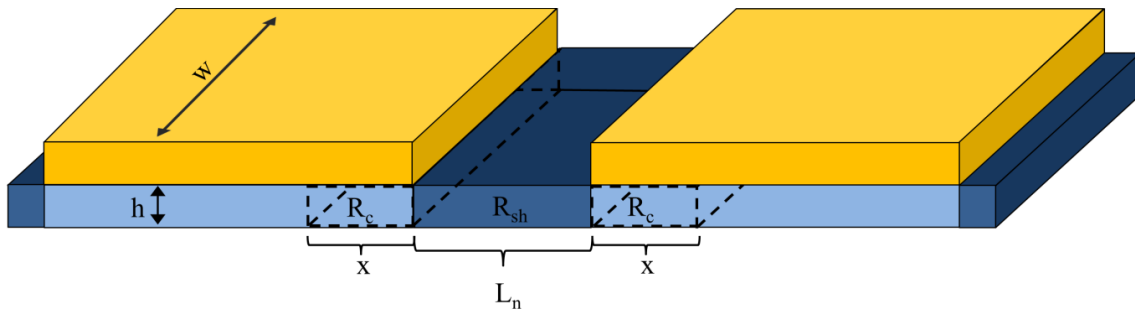


Figure 4.13: A sketch illustrating “effective  $x$ ”.  $L_n$  is the gap length,  $R_{sh}$  is the sheet resistance of the  $\text{VO}_2$  between the contacts, and  $R_c$  is the contact resistance, which includes the resistance of the  $\text{VO}_2$  under the pad (which is different from  $R_{sh}$ ) and the interfacial resistance.

heat sink, which prevents local heating under the contact pads. Joule heating in the volume between the contacts rather than under the pads is thus expected to be the dominant factor determining the temperature profile in the film. Consequently, the contact resistance is anticipated to be a weak function of power dissipated in the film.

The criterion that contact resistance does not change with dissipated power density requires that the resistance-gap length lines all intersect on the resistance-axis. A series of trial values for the volume under the contact in which power is dissipated, described by “effective length”,  $x$ , were tried and the “best” was chosen. For a given  $x$ -value, a series of power density values were used to extract the resistance-gap length data. A least-squares fit linear regression was used to find the slope and y-intercept values for the resistance-length data at each power density. The range of resistance-axis-intercepts for each  $x$ -value was calculated. The  $x$ -value was then incremented and the process was repeated. The  $x$ -value that yielded the smallest range of resistance-axis intercepts was determined to be the “best” value and the volume under the contact pads in which the power is dissipated was defined (Figure 4.14).

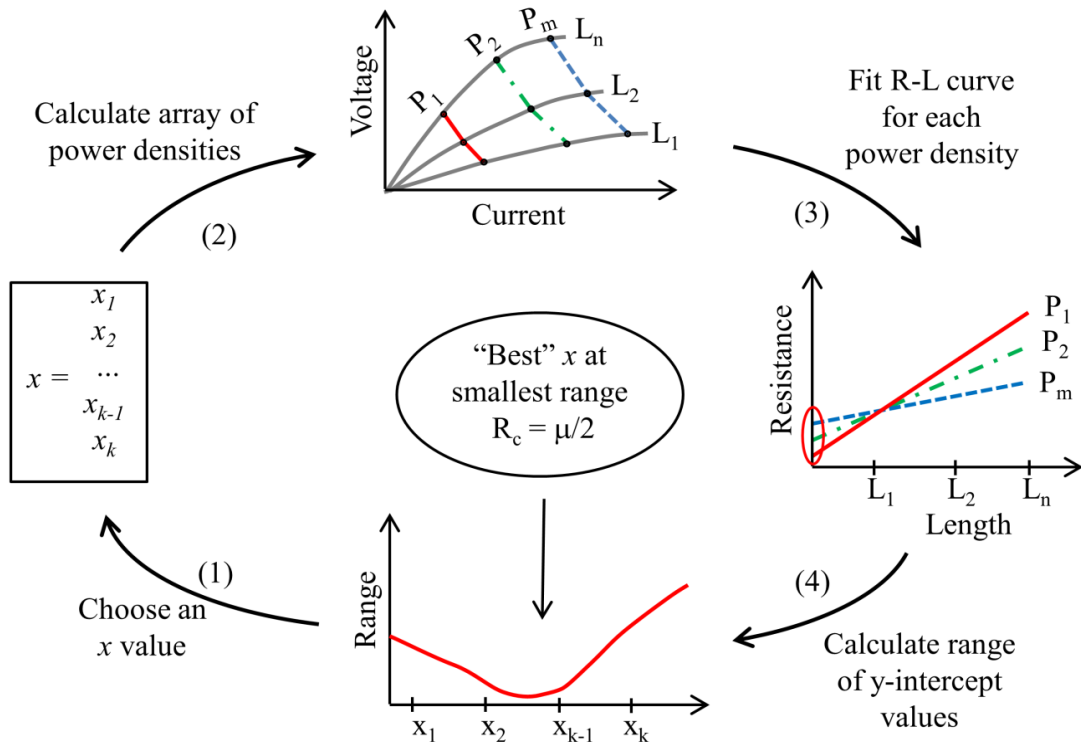
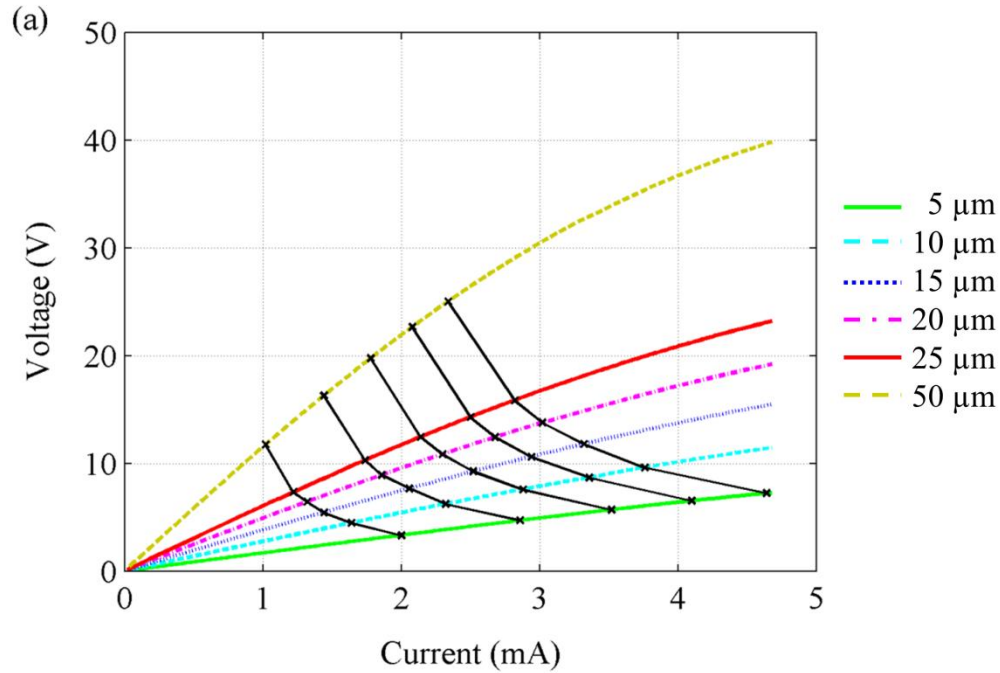
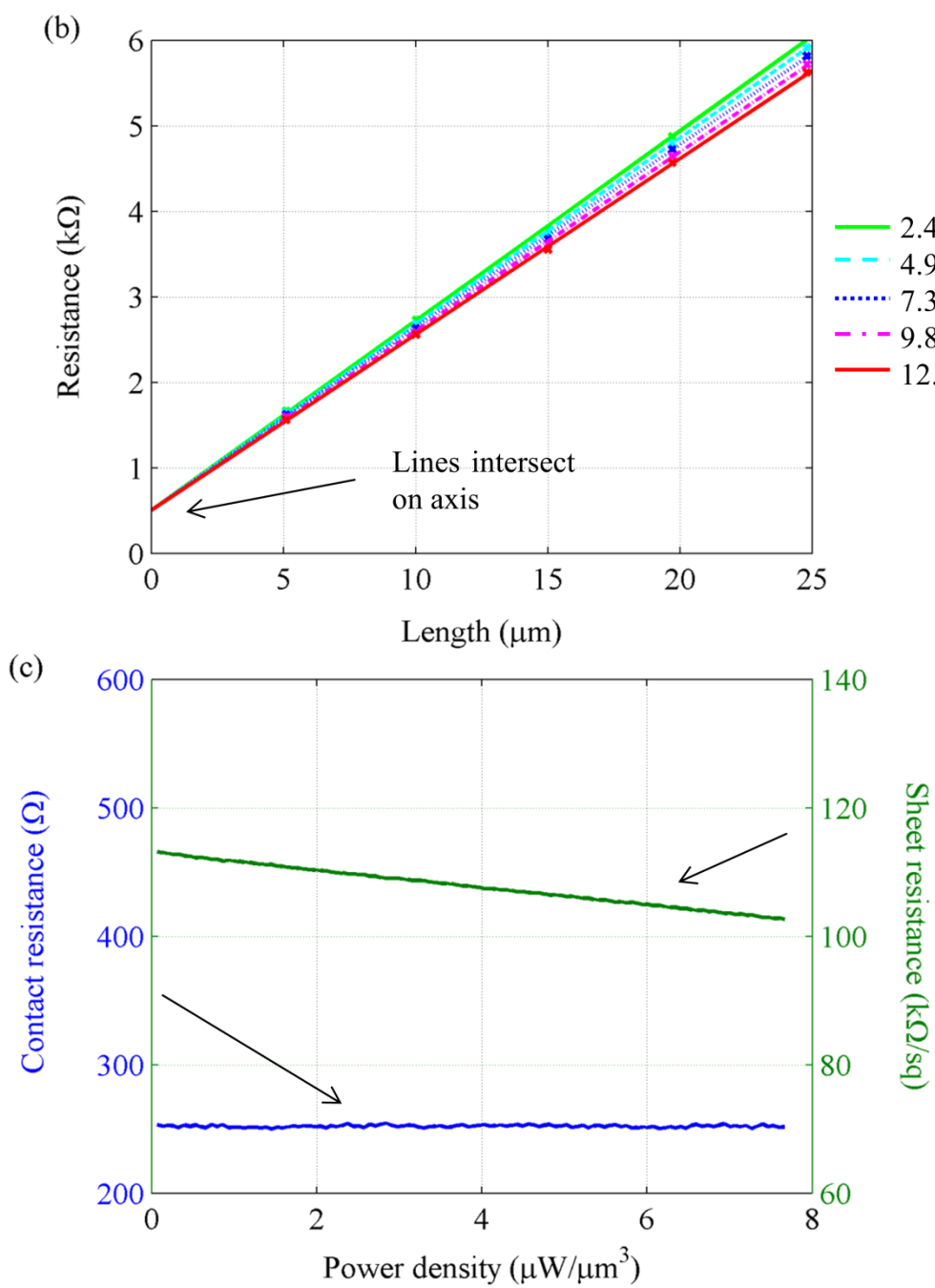


Figure 4.14: A diagram showing the process used to determine the effective length,  $x$ . (1) An array of  $x$ -values is stepped through. (2) The resistance-length data for a given  $x$  value is extracted from the raw data using the modified dissipated power density. (3) A linear fit to the R-L data is performed for each power density. (4) The range of the y-intercepts in (3) is calculated. After the range of intercepts for each  $x$  value has been calculated, the value with the smallest range of resistance axis intercepts is chosen as the “best”.

#### 4.4 Contact Resistance Measurement Results

The process described above was applied to a set of measured data as shown in Figure 4.15. The effective  $x$  value was found and used to calculate the dissipated power density. Using this modification, the intersection of the resistance-gap length lines was shifted to the resistance axis (Figure 4.15b). The minimum range of resistance intercept values occurred at an effective  $x$  of  $26\text{ }\mu\text{m}$ , yielding an effective volume of  $1300\text{ }\mu\text{m}^3$  per contact pad (Figure 4.15d). The contact resistance and sheet resistance (Figure 4.15c) were calculated across the semiconducting phase of the device for differing levels of power dissipation. The contact resistance was about  $250\text{ }\Omega$  for all power densities indicating that the constraint used in developing the method is consistent. The power density is directly related to temperature so the decrease in sheet resistance with increasing power density is an expected result.





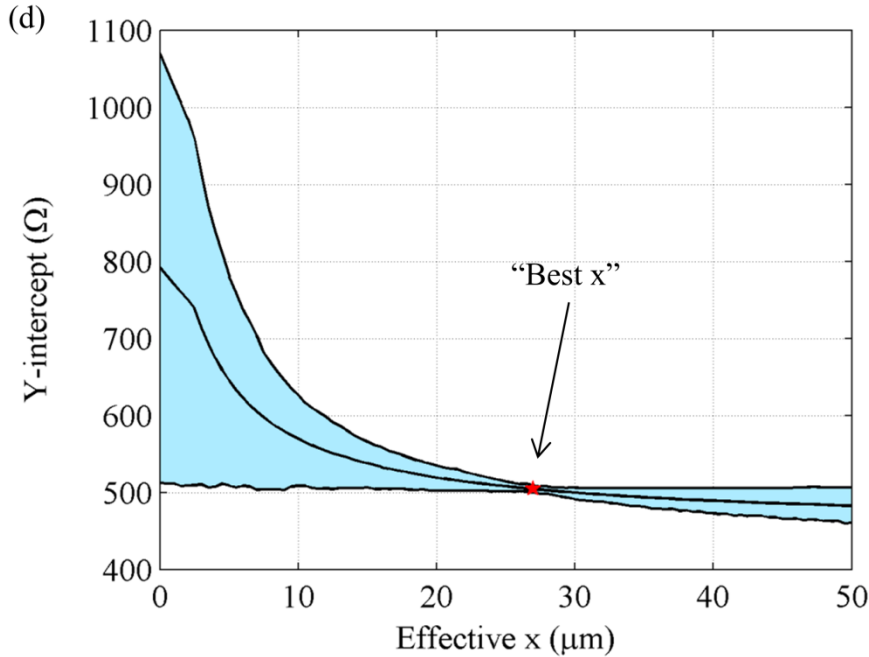


Figure 4.15: (a) The raw IV data with several superimposed lines of constant dissipated power density as calculated using the volume between the contacts and the volume under the contacts and within the calculated “effective  $x$ ” value. (b) A resistance-length plot using the data from (a). At least fifty different power densities are used for the calculations but only five are plotted for clarity. (c) The resulting contact resistance and sheet resistance. (d) The mean y-intercept and one standard deviation plotted for each “effective  $x$ ” value.

#### 4.4.1 Resistivity as a function of power density

Resistivity is an intrinsic material parameter and is expected to be independent of the gap length of the contact pads across the entire measurement range. Figure 4.16 shows the resistivity of the  $\text{VO}_2$  between each pair of adjacent contact pads as a function of current or dissipated power density with and without the contact resistance removed. In all cases, the resistivity calculation assumes that the  $\text{VO}_2$  has a uniform current flow between the contacts with a uniform cross-sectional area and a length equivalent to the contact pad gap length (equation 4.8).

$$\rho = \left( \frac{V}{I} - 2R_c \right) \frac{wh}{L} \quad (4.8)$$

For results that do not remove the contact resistance, such as those shown in Figure 4.16a and Figure 4.16c,  $R_c$  is set equal to  $0 \, \Omega$ . The resistivity calculation does not include the effective  $x$  value because removing the contact resistance accounts for the region under the contact pad.

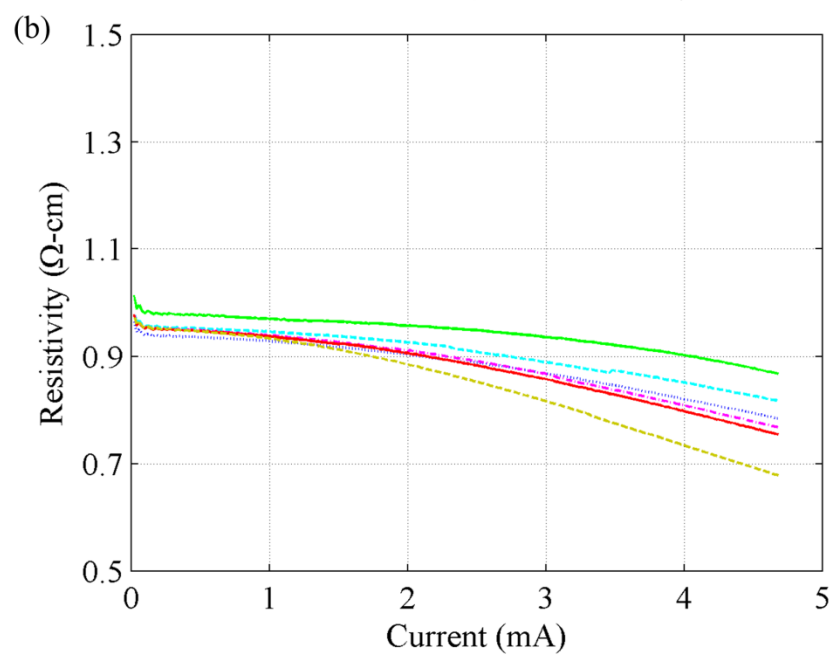
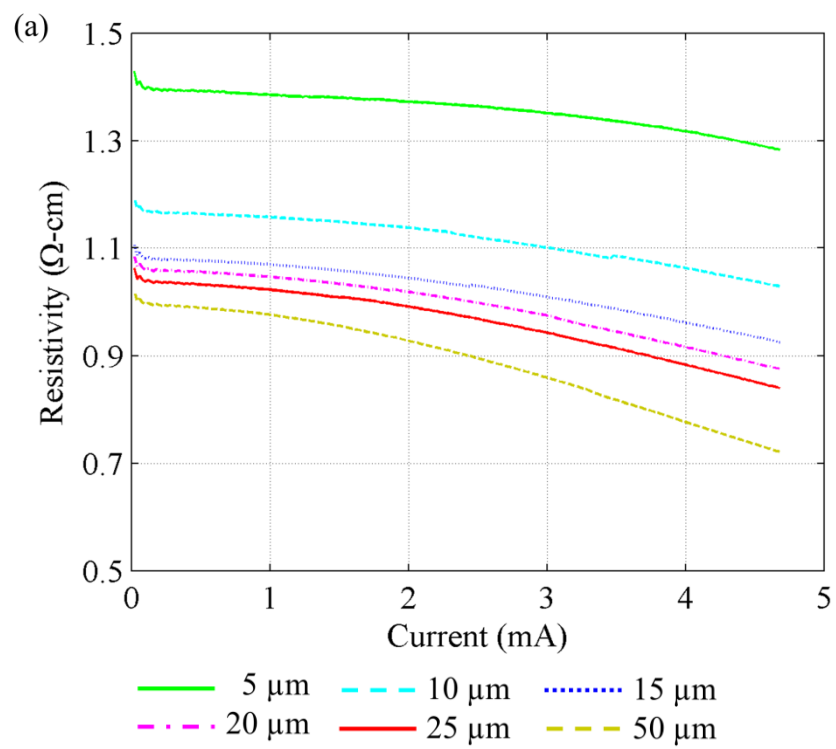
Figure 4.16a shows the resistivity, including contact resistance, as a function of current. The resistivity for each of the gaps was different and that difference increased with increasing current. Figure 4.16b is the same as Figure 4.16a except the contact resistance as calculated using the traditional method at a small current bias (Figure 4.8c) was removed. The resistivity for each gap is closer to a single value; however, they diverge as the current increases.

When calculating resistivity as a function of power density (4.9), the divergence

$$P_D = \frac{IV}{wh(L + 2x)} \quad (4.9)$$

with increasing power density was nearly removed. The power density accounts for the percolation of metallic regions as the power density increases. In Figure 4.16c, the resistivity, including the contact resistance, is plotted against the power density where the power density calculation does not include the volume under the contact pads ( $x = 0$ ). The resistivity is not uniform for each gap but the divergence across the range of power densities is less than with the current bias method. Figure 4.16d shows the resistivity calculated using the effective volume method. The contact resistance was removed from the measured resistance before calculating the resistivity and the power density was calculated including the volume under the contact pads. Removing the contact resistance prior to calculating the resistivity brings the calculated resistivity closer to uniform. Including the effective volume under the pads in which power is dissipated makes it so that the decrease in resistivity with increasing power density is uniform for all gaps.





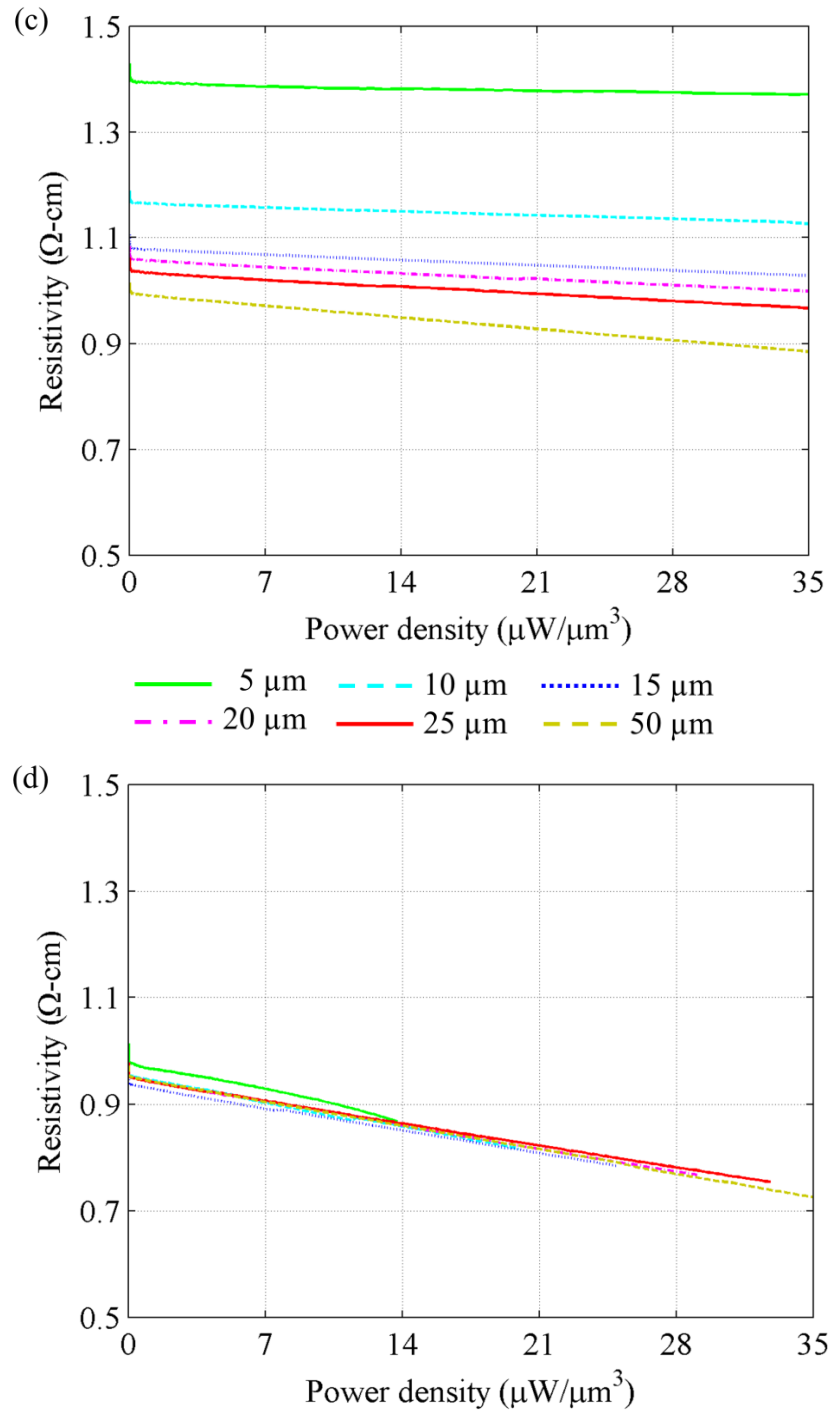


Figure 4.16: The resistivity of the  $\text{VO}_2$  between the contact pads for each gap length (a) versus current without contact resistance removed, (b) versus current with the contact resistance removed, (c) versus power density without contact resistance removed, and (d) versus power density with contact resistance removed.

The measured resistivity of the VO<sub>2</sub> using the modified method is found to be 0.95 Ω-cm for lower power densities and decreases to 0.73 Ω-cm as the power density increases. This value is 3.5x the room temperature resistivity as calculated without any geometric corrections during resistance – temperature measurements. This difference can be partially attributed to different fabrication procedure as discussed in chapter 3.

#### 4.4.1.1 Contact Resistance and Specific Contact Resistivity

The specific contact resistance,  $\rho_c$ , is a normalization parameter for contact resistance. If the effective  $x$  value is taken to play the same role as transfer length, then the specific contact resistance can be calculated from equation 4.10. In equation 4.10,  $R_c$  is the calculated contact

$$\rho_c = R_c w x \quad (4.10)$$

resistance,  $w$  is the width of the contact, and  $x$  is the effective  $x$  value.

Using an effective length of 26 μm and a contact pad width of 500 μm, specific contact resistivity,  $\rho_c$ , is found to be  $3.4 \times 10^{-2} \Omega\text{-cm}^2$ . Using the standard tlm method with a small, constant current bias (20 μA), the specific contact resistance of our device is calculated as  $1.4 \times 10^{-3} \Omega\text{-cm}^2$ . This suggests that in materials with a non-constant resistivity due to thermal effects, such as VO<sub>2</sub>, the standard tlm method can lead to underestimating the contact resistance because of the Joule heating. Thus, the constant dissipated power density method presented should be used in such materials.

A previous study reports a room temperature specific contact resistivity for a VO<sub>2</sub> – gold interface of approximately  $3 \times 10^{-5}$  to  $10^{-4} \Omega\text{-cm}^2$  using circular tlm method at a single bias current [5]. The standard rectangular tlm method with a 20 μA constant current bias uses the same basic theory as the circular tlm method used in the previous study [9]. Using the standard rectangular tlm method, a specific contact resistivity of  $1.4 \times 10^{-3} \Omega\text{-cm}^2$  was measured, which is about an order of magnitude larger than the published value. There are several possible sources for this discrepancy. The previous study does not specify the current or voltage bias used in the resistance measurements. It was shown in this chapter that lower current bias will yield lower

contact resistance (Figure 4.8b). They did not describe the fabrication technique beyond specifying that the gold was deposited using thermoresistive evaporation (compared to e-beam evaporation). The existence of an adhesion layer, its material, and its thickness are not described; however, their conclusions suggest that the metal used for the contact can have a huge effect on the specific contact resistance [5]. Cleaning prior to contact deposition is not mentioned other than exposure to hydrofluoric acid to remove a  $\text{SiO}_2$  capping layer used during fabrication to protect the  $\text{VO}_2$  film. The  $\text{VO}_2$  films in this chapter were not cleaned via an ion mill or other technique before evaporation of the metallic contact. Additionally, their films were grown via oxidation of vanadium metal on a  $\text{SiO}_2$  substrate whereas the films in this chapter were grown on sapphire using RBTIBD. As with all ohmic contacts, fabrication techniques play a significant role in the quality of metal-semiconductor interface and specific contact resistance can be decreased significantly by optimizing the fabrication procedure.

#### **4.4.2 Contact Resistance as a Function of External Temperature**

To determine the effect of external temperature on the contact resistance and effective volume under the contact pad, a single device was measured at four different temperatures between room temperature and the material transition temperature. The wafer was measured while lying on a hot plate and the wafer temperature monitored using a diode thermometer. The use of a hot plate ensured that the entirety of the wafer, including the contact pads, was at the same temperature. The wafer was not moved between measurements. The measurement range was chosen such that the device would not reach the transition point during the first three measurements. This prevents the  $\text{VO}_2$  from being permanently altered from the additional Joule heating during the measurements (see appendix A). Consistent with the expected results, it was found that the specific contact resistivity, sheet resistance, and effective volume all decreased as a function of increasing temperature (Figure 4.17).

The sheet resistances presented in the results in Figure 4.17a are based on the calculated sheet resistance using the modified contact resistance method at the lowest power density used in the measurements. This value is used so that any change in sheet resistance as the temperature

increases is a result of applied external temperature increase and not Joule heating. It is seen that the sheet resistance decreases with increasing temperature. The sheet resistance is directly related to the resistivity of the VO<sub>2</sub>, which is well known to decrease as temperature increases (e.g. [13]) and thus this result is expected. Additionally, the sheet resistance decreased by one order of

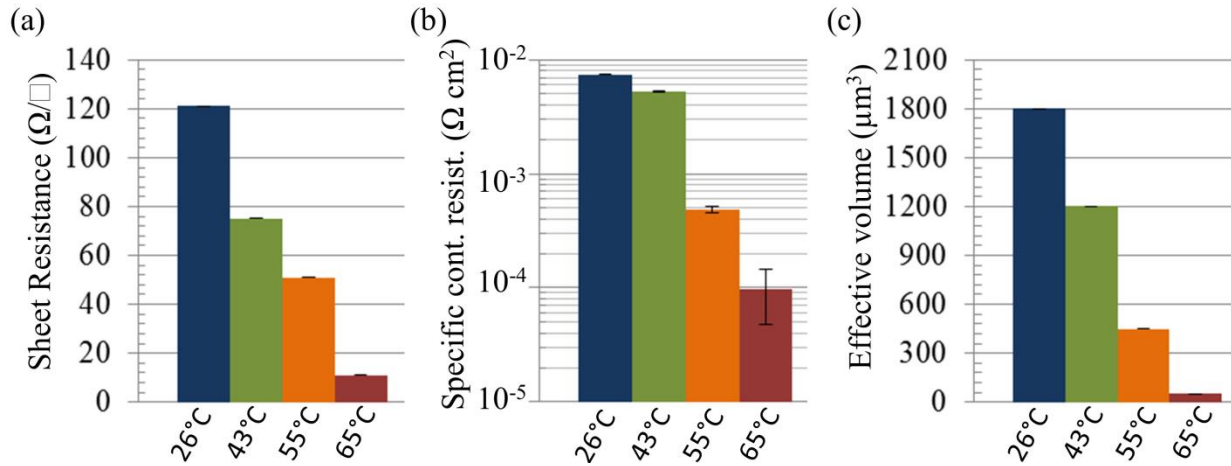


Figure 4.17: The (a) sheet resistance, (b) specific contact resistivity, and (c) effective volume at 26 °C, 43 °C, 55 °C, and 65 °C. The specific contact resistivity error is based on the range of y-intercept values. The sheet resistance is based on the best fit equation for the sheet resistance as a function of power density when power density is extrapolated to 0 (the y-intercept of the best fit line).

magnitude over the range of temperatures which is in agreement with the resistance – temperature measurement in Figure 4.4a.

The specific contact resistivity (Figure 4.17b) decreases with increasing temperature. The increase in applied external temperature causes the sheet resistance of the VO<sub>2</sub> both between and underneath the contacts to decrease. The specific contact resistance includes not only the interfacial resistance but the resistance of the VO<sub>2</sub> beneath the contacts. So as the sheet resistance of the VO<sub>2</sub> beneath the contacts decreases, the specific contact resistant also decreases.

The effective volume (Figure 4.17c) also decreases with increasing temperature. The transition temperature is the sum of the externally applied temperature and the increase in temperature from Joule heating. As the external temperature increases, there is a smaller increase in temperature from Joule heating so less power is dissipated into the contact pads, or heat sinks. With less power to dissipate, the size of the heat sink can be smaller and thus a smaller effective volume is expected at higher external temperatures.

## 4.5 Conclusions

In summary, a modified approach for determining contact resistance has been described to evaluate the quality of the contacts for planar devices with resistivity dependent on Joule heating. In comparison, the standard tlm method is shown to yield the contact resistance one order of magnitude smaller. The modified method yields a resistivity that is independent of the gap length across the entire range of power densities.

- [1] Editorial, “The interface is still the device,” *Nature Materials*, p. 11, Feb. 2012.
- [2] H. Berger, “Models for contacts to planar devices,” *Solid-State Electron.*, vol. 15, no. 2, pp. 145 – 158, 1972.
- [3] G. S. Marlow and M. B. Das, “The effects of contact size and non-zero metal resistance on the determination of specific contact resistance,” *Solid-State Electronics*, vol. 25, no. 2, pp. 91 – 94, 1982.
- [4] G. Reeves and H. B. Harrison, “Obtaining the specific contact resistance from transmission line model measurements,” *Electron Device Letters, IEEE*, vol. 3, no. 5, pp. 111–113, 1982.
- [5] K. Martens, I. P. Radu, S. Mertens, X. Shi, L. Nyns, S. Cosemans, P. Favia, H. Bender, T. Conard, M. Schaekers, S. De Gendt, V. Afanas’ev, J. A. Kittl, M. Heyns, and M. Jurczak, “The VO<sub>2</sub> interface, the metal-insulator transition tunnel junction, and the metal-insulator transition switch on-off resistance,” *Journal of Applied Physics*, vol. 112, no. 12, p. 124501, 2012.
- [6] W. Shockley, “Research and investigation of inverse epitaxial uhf power transistors,” Wright-Patterson Air Force Base, Ohio, Tech. Rep., September, 1964.
- [7] V. Y. Niskov and G. A. Kubetskii, “Resistance of ohmic contacts between metals and semiconductor films,” *Soviet Physics - semiconductors*, vol. 4, pp. 1553–1554, 1971 1971.

- [8] R. Williams, *Modern GaAs Processing Methods*, 2nd ed. Boston: Artech House, 1990.
- [9] G. Reeves, "Specific contact resistance using a circular transmission line model," *Solid-State Electronics*, vol. 23, no. 5, pp. 487 – 490, 1980.
- [10] K. West, J. Lu, J. Yu, D. Kirkwood, W. Chen, Y. Pei, J. Claassen, and S. A. Wolf, "Growth and characterization of vanadium dioxide thin films prepared by reactive-biased target ion beam deposition," *Journal of Vacuum Science Technology A: Vacuum, Surfaces, and Films*, vol. 26, no. 1, pp. 133–139, 2008.
- [11] J. S. Lee, M. Ortolani, U. Schade, Y. J. Chang, and T. W. Noh, "Time-resolved visualization of the heat flow in VO<sub>2</sub>/Al<sub>2</sub>O<sub>3</sub> films," *Applied Physics Letters*, vol. 90, no. 5, p. 051907, 2007.
- [12] H.-T. Kim, B.-J. Kim, S. Choi, B.-G. Chae, Y. W. Lee, T. Driscoll, M. M. Qazilbash, and D. N. Basov, "Electrical oscillations induced by the metal-insulator transition in VO<sub>2</sub>," *J. Appl. Phys.*, vol. 107, no. 2, p. 023702, 2010.
- [13] F. J. Morin, "Oxides which show a metal-to-insulator transition at the Neel temperature," *Phys. Rev. Lett.*, vol. 3, pp. 34–36, Jul 1959.

## Chapter 5: Characterization of VO<sub>2</sub> Switching Elements at Submillimeter Wavelengths

The recent development of on-wafer terahertz measurement systems permits direct in-situ characterization of planar devices at frequencies approaching 1 THz. Such measurements are critical for assessing new and emerging device technologies for high-frequency applications, including those based on vanadium oxide, and allow accurate circuit models to be derived for use in circuit design. Vanadium oxide switches are of interest for their potential use in realizing reconfigurable circuits at these frequencies. Moreover, VO<sub>2</sub> could be used for designing tunable circuit elements such as matching networks and filters. The large current- or voltage- induced change in resistivity associated with VO<sub>2</sub> makes it appealing for such applications.

In this chapter, a single element (one port) device consisting of a thin film VO<sub>2</sub> load at the terminus of a coplanar waveguide (CPW) transmission line is designed and characterized in the WR-1.5 waveguide band (500-750 GHz). These results demonstrate that the voltage-induced IMT modulates the return loss by about 10 dB. The metallic state impedance of the VO<sub>2</sub> film is also calculated from the data obtained. Next, a two port switch consisting of two CPW transmission lines connected in series with a VO<sub>2</sub> load is designed and characterized in the WR-1.5 waveguide band. The results show that the IMT modulates the switch by 5 to 10 dB depending on the device size. In both devices, the results indicate a primarily resistive device making VO<sub>2</sub> attractive for broadband applications. These results represent the first on-wafer VO<sub>2</sub> controlled terahertz switch. A similar design has been measured on-wafer at microwave frequencies [1] but has not been scaled to higher frequencies. Terahertz switches based on the VO<sub>2</sub> IMT have been demonstrated at terahertz frequencies but these devices were quasi-optical switches, not on wafer [2, 3].



## 5.1 Microwave Frequency Measurements

On-wafer return loss measurements of VO<sub>2</sub> films from 0.045 to 20 GHz were performed using an HP8510 vector network analyzer equipped with commercially-available probes manufactured by GGB Industries. The HP8510 was calibrated to the probe tips using trl method and pre-printed standards. The reflection coefficient ( $\Gamma$ ) was initially measured to characterize the microwave response of the material. The device under test (DUT) (Figure 5.1) was a recycled structure used for Hall Effect measurements. The signal probe was placed on the lower left contact and the ground probe on the lower right contact pad device. The device was current biased via the RF probe tips using a Keithley 236 SMU under manual operation. The transition occurred at 8 mA; unfortunately, the dc resistance was not recorded.

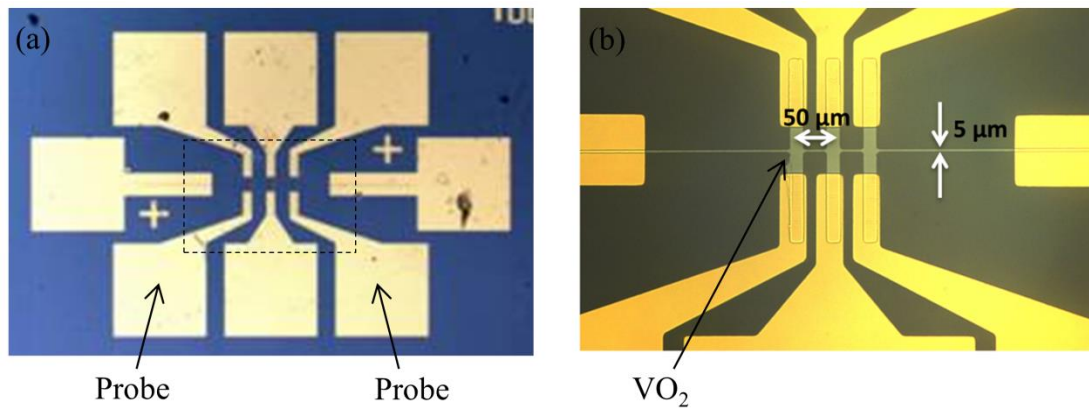


Figure 5.1: (a) A photograph of the DUT indicating the probe location. (b) A higher magnification photo showing geometry of the VO<sub>2</sub> in a similar device.

The impedance of the DUT is primarily real at lower frequencies and exhibits increasing susceptance with increasing frequency (Figure 5.2). At a bias of 14 mA, the VO<sub>2</sub> is in the metallic state, has a lower impedance, and is closer to the center of the Smith chart, indicating a higher return loss. With no bias applied, the device is in a semiconducting state, has relatively high impedance, and is closer to the open-circuit on the Smith chart.

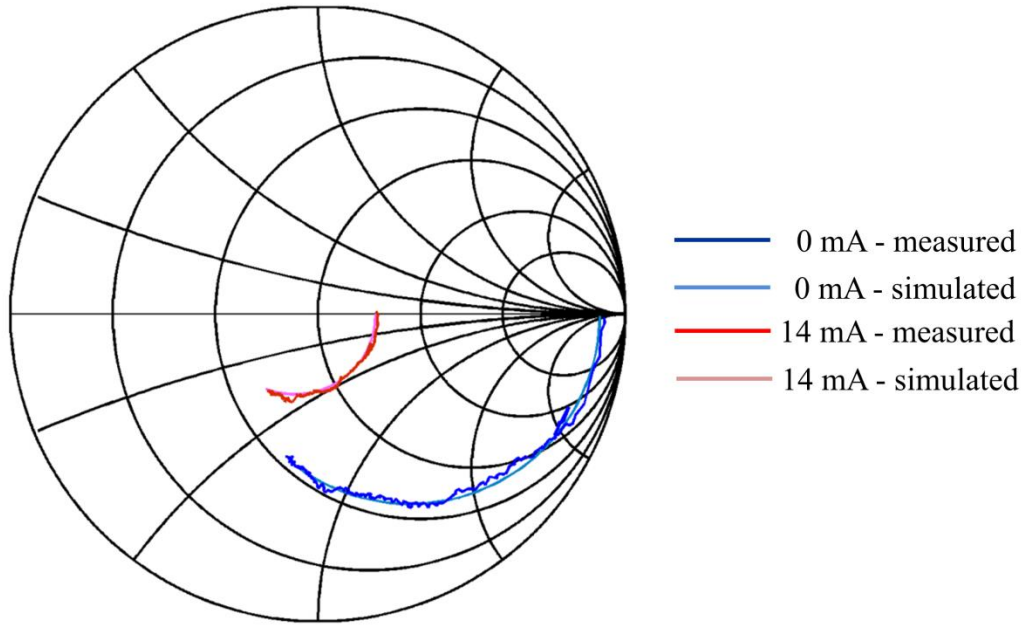


Figure 5.2: A Smith Chart showing measured and simulated return loss from 0.050 to 20 GHz.

A simulation of the VO<sub>2</sub> device was performed using Agilent Advanced Designs System (ADS) schematic. The HP8510 was calibrated to the probe tips so the measurement includes the transmission lines between the probe tips and the VO<sub>2</sub> itself. Because the device was not designed for this measurement, the transmission lines are not standard so a parallel RC circuit was used to simulate them along with a different parallel RC circuit to represent the VO<sub>2</sub>. The equivalent circuit is shown in Figure 5.3. When the transmission line portions of this circuit are removed from the measurement data, the VO<sub>2</sub> portion of the measurement lies on a line of constant conductance indicating that only the susceptance changes (Figure 5.4). This is most likely a result of the geometry of the circuit and not the VO<sub>2</sub>; the VO<sub>2</sub> is purely resistive.

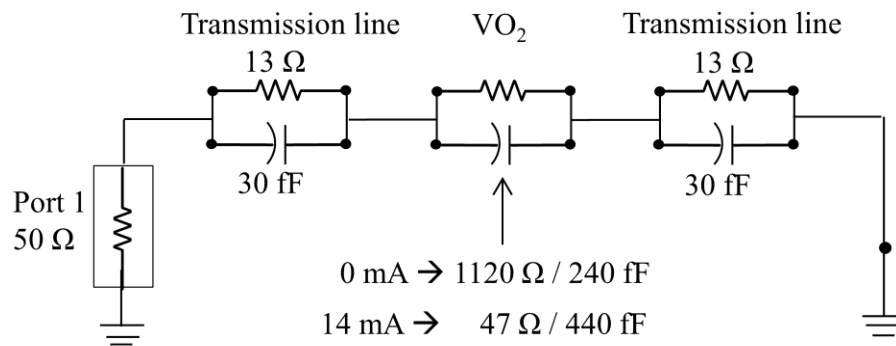


Figure 5.3: The equivalent circuit model for the Hall Bar structure. The transmission line represents the gold lines between the probe and the VO<sub>2</sub>. The VO<sub>2</sub> results are given for the semiconducting (0 mA) and metallic (14 mA) states.

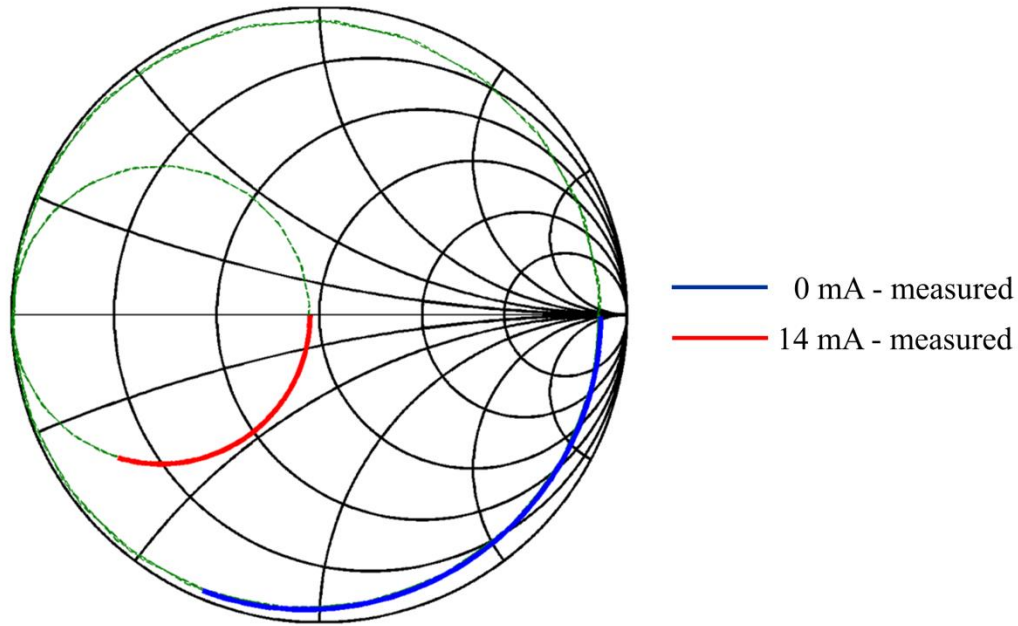


Figure 5.4: The equivalent circuit model results for the microwave device after the transmission line portion has been removed. Notice that both the semiconductor and metallic state regions lie on lines of constant conductance.

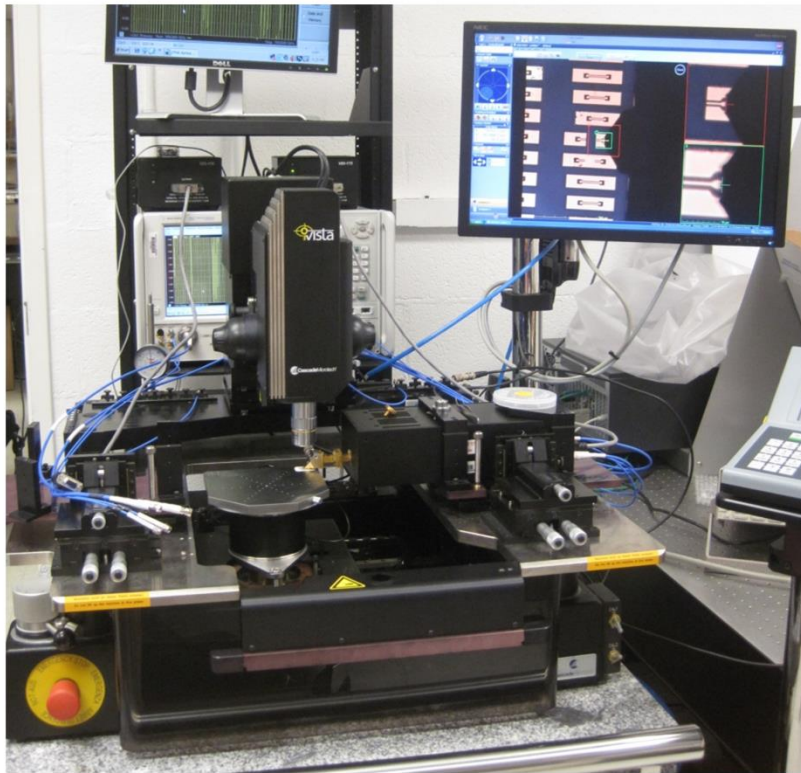
## 5.2 VO<sub>2</sub> Device Fabrication and Experimental Setup for Submillimeter On-Wafer Measurements

### 5.2.1 Fabrication Approach

The vanadium oxide thin film switching elements were fabricated on a c-plane sapphire substrate. Reactive-biased target ion beam deposition (RBTIBD) was used to deposit an approximately 100 nm thick single phase and highly textured VO<sub>2</sub> thin film similar to that described in chapter 2. The devices were formed in two lithography steps. The VO<sub>2</sub> thin film was initially patterned using positive photoresist and then etched using a reactive ion etch (RIE). The resist was then removed using an O<sub>2</sub> plasma clean at 120W. Following this, CPW lines were patterned using negative-tone photoresist and UV lithography. An electron-beam evaporation system was used to deposit a 100Å thick Titanium adhesion layer followed by an in-situ 1500Å thick gold layer. Liftoff was performed using an 80 °C NMP soak followed by an ethylene-glycol swab forming the metallic contact pads. The devices were inspected for irregularities using an optical microscope and SEM.

The VO<sub>2</sub> devices were characterized using WR-1.5 on-wafer probes designed and fabricated at the University of Virginia and interfaced to a backend Agilent N5245A vector network analyzer and frequency extension modules manufactured by Virginia Diodes, Inc. using rectangular waveguide adaptors (Figure 5.5). The DUT was placed on a ceramic platen inlaid in the stage to suppress potential surface wave excitation caused by a metallic ground plane beneath CPW line. The DUT was biased through the RF probes using a Keithley 236 SMU. A Python script was used to increase the voltage bias until the current reaches compliance (set to 10mA), indicating that the VO<sub>2</sub> had become metallic. Continuing to increase the voltage after the transition can result in permanent structural damage to the VO<sub>2</sub> or even destroy the device (see appendix A).

(a)



(b)

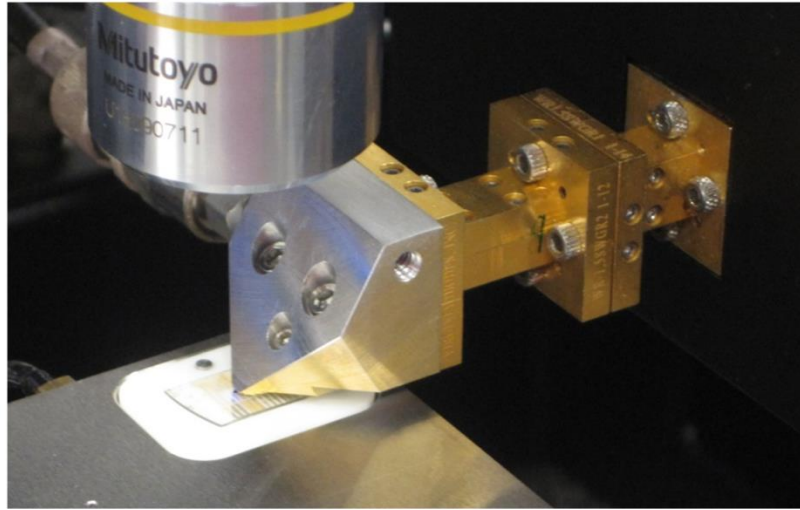


Figure 5.5: (a) A photograph of the THz probe state in one-port configuration.  
(b) A photograph of the WR-1.5 probe contacting the DUT.

### 5.3 One Port Device with $\text{VO}_2$ Load in Semiconducting and Metallic States

The return loss of a transmission line terminated with a  $\text{VO}_2$  load was measured at WR-1.5 when the  $\text{VO}_2$  was in the semiconducting and metallic states. Five identical DUT's from a single wafer and processing run were each measured multiple times. The magnitude and phase of the return loss and the metallic state impedance were extracted from these measurements. A large mismatch between the semiconducting impedance and the probe impedance prevented the semiconducting impedance from being calculable. A sample result, a study of uniformity between the devices, and a study of the repeatability of a single device over ten switching events are presented.

#### 5.3.1 Design of a CPW Terminated with a $\text{VO}_2$ Load

The change in the state of  $\text{VO}_2$  that accompanies the IMT can be used to modulate the return loss for a variety of applications. The  $\text{VO}_2$  film is fed using coplanar waveguide (CPW).

CPW is a planar transmission line consisting of a center conductor line separated by a gap from the ground plane on either lateral side, all atop a dielectric material (Figure 5.6). In theory, the dielectric material is infinitely thick; in practice, a general guideline is that the dielectric layer must be thicker than the distance between the two ground planes. Its main benefit is the ease of incorporating active elements, such as the  $\text{VO}_2$  load, into the circuit without having to worry about an exact dielectric thickness, thinning the dielectric, or a ground plane below the dielectric such as with microstrip line. In theory, an infinite number of combinations of signal conductor width and conductor-ground plane separation distances are available for any given impedance; a satisfactory combination can be chosen based on desired device parameters, loss, fabrication, and real estate limitations [4].

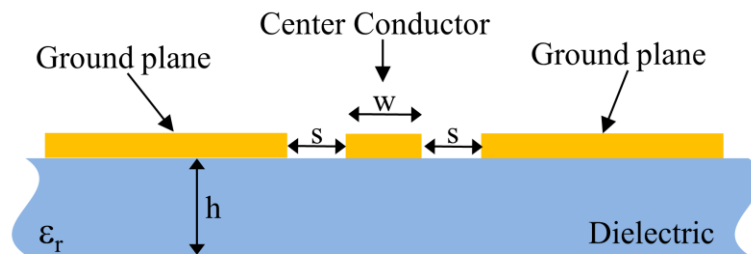


Figure 5.6: A sketch of the structure of CPW. The center conductor has a width,  $w$ , and center conductor to ground distance,  $s$ . The direction of wave propagation is into or out of the page.

CPW was chosen in this design for its ease of integration with the  $\text{VO}_2$  film and so as to avoid thinning the sapphire substrate. The CPW line was designed to have a characteristic impedance that matches the on-wafer probe impedance of  $50\ \Omega$ . The width of the  $\text{VO}_2$  was chosen to be equal to that of the center conductor of the CPW (Figure 5.7) to prevent stray reflections that occur where there is a change in width of the center conductor. The length of the film was based on the sheet resistance of the  $\text{VO}_2$ . Prior measurements done at the University of Virginia found that the semiconducting state sheet resistance of 100 nm thick  $\text{VO}_2$  films deposited in the RBTIBD system is approximately  $10\ \text{k}\Omega/\text{sq.}$  and the metallic state sheet resistance is approximately  $100\ \Omega/\text{sq.}$  at room temperature. Consequently, a  $\text{VO}_2$  film with a size of half square was chosen so that the metallic state  $\text{VO}_2$  thin film resistance matches the resistance of the transmission line and measurement system. The half square  $\text{VO}_2$  load in the semiconducting state was expected to produce a high resistance, approximately  $5000\ \Omega$ . In simulation, this design yielded an ideal semiconducting return loss of  $-0.174\ \text{dB}$  and a perfect



match (with no reflection) in the metallic state. The load was modeled as resistive (no reactance) so the return loss was not dependent on frequency.

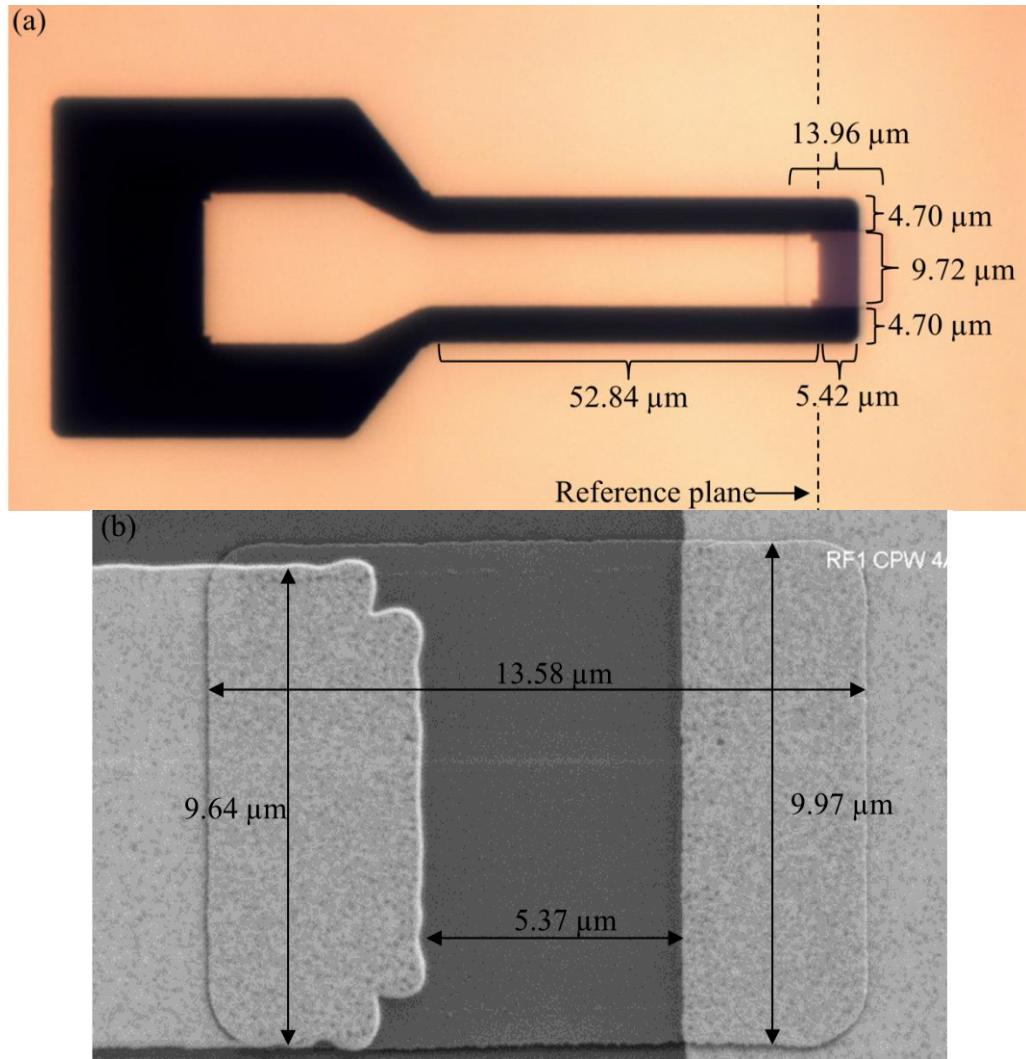


Figure 5.7: An (a) optical image and a (b) SEM image of a one-port, CPW fed, VO<sub>2</sub> device.

### 5.3.2 Calibration for One-Port Measurements

The WR-1.5 measurement system was configured for a one-port measurement and was calibrated using a set of known terminations, known as standards. Six standards were used, which exceeds the number of necessary unknowns (three) in the standard one-port error model of the system. Consequently, a least squares method was applied to this over determined system to permit a better estimation of the system error coefficients. The calibration coefficients were

determined by measuring five different delay shorts and an open circuit and comparing these measurements to the simulated results from Ansoft's High Frequency Structure Simulators (HFSS). Re-measuring the standards after calibration allowed measurement repeatability and error to be assessed. When this was done, the open standard's reflection coefficients were partially outside the Smith Chart that indicating some systematic error was not removed from the measurement (Figure 5.8).

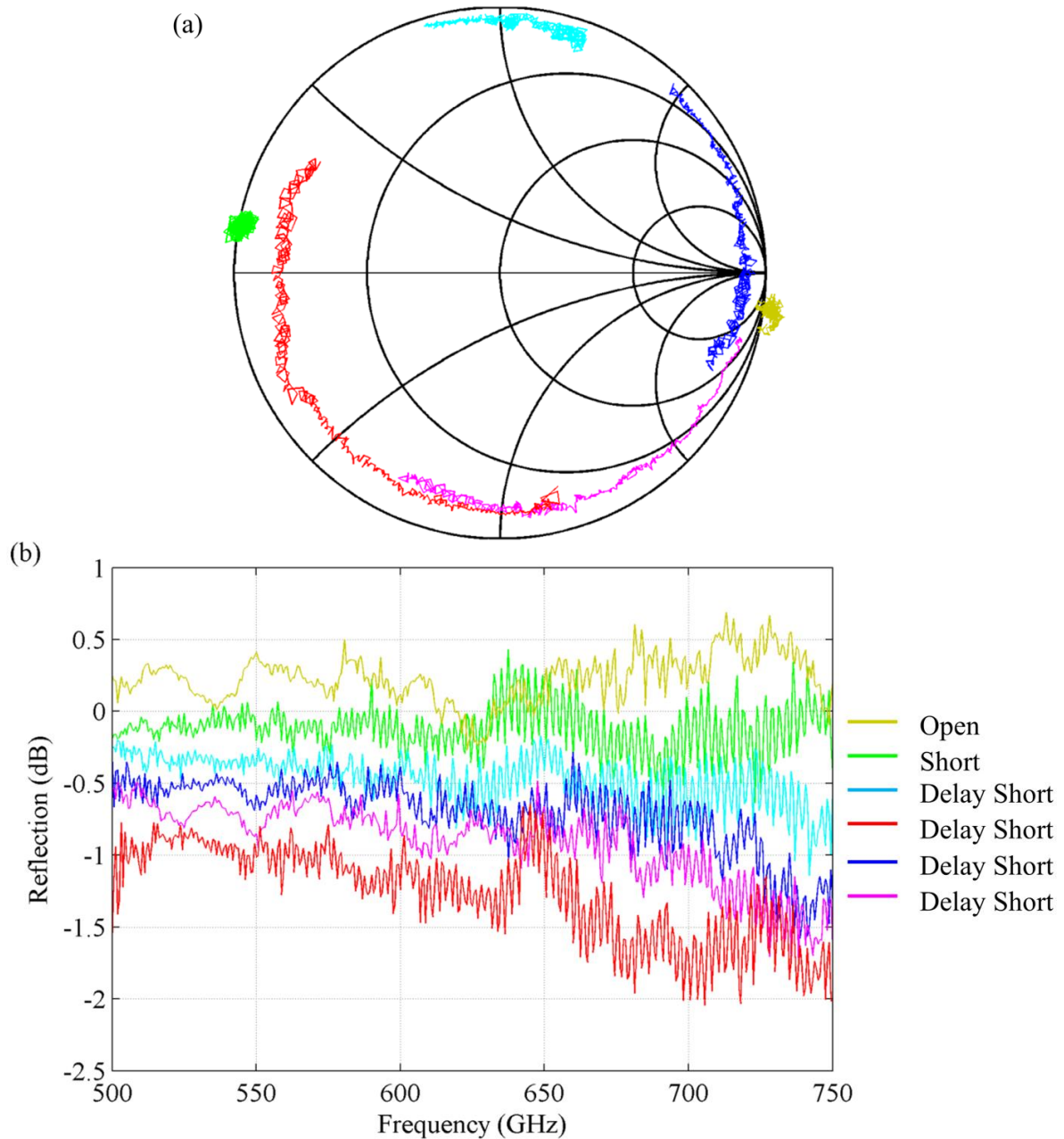


Figure 5.8: The calibration standards as re-measured after calibration. (a) A Smith Chart representation shows that some measurements lie outside the  $\Gamma = 1$  circle. (b) A magnitude plot shows that the open and parts of the short have return loss greater than 0 dB.



The calibration error as indicated by remeasuring the open standard was manually removed from the return loss measurements. The open standard was measured twice and the results averaged by frequency (Figure 5.9). Averaged across the band, the open standard had a magnitude of  $+0.2262 \pm 0.1172$  dB with a maximum value of  $+0.7386$  dB and a minimum value of  $-0.2769$  dB. The open standard should have a magnitude of 0 dB across the entire band. To account for this error, the return loss measurements were normalized by dividing the return loss results by the open standard results at each frequency (equation 5.1).

$$\Gamma_{normalized} = \frac{Z_{measured}}{Z_{open}} = \frac{R + jX}{R_{open} + jX_{open}} \quad (5.1)$$

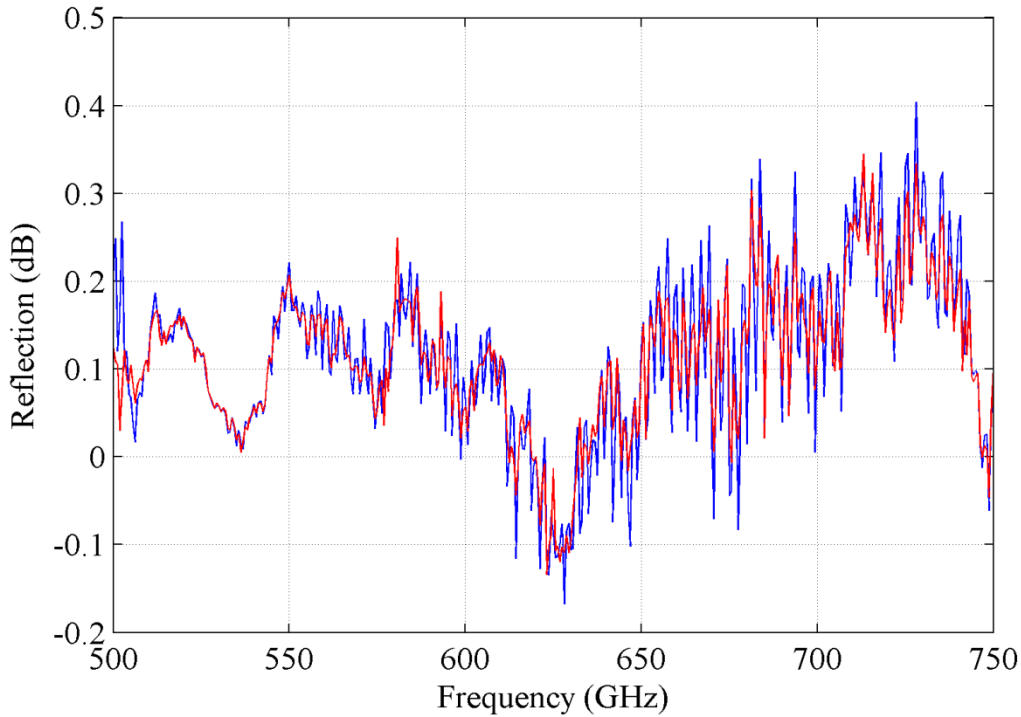


Figure 5.9: The open calibration standard re-measured twice after calibration.

### 5.3.3 One-port Measurement Results

In this section, the return loss measurements of the VO<sub>2</sub> films in the semiconducting and metallic states are presented. Five identical DUT's from a single wafer and processing run were measured one to nine times each. The magnitude and phase of the return loss and the metallic state impedance were extracted from these measurements. Calibration error combined with a

large mismatch between the semiconducting impedance and the probe impedance prevent the semiconducting impedance from being determined with precision. A representative measurement result, a study of uniformity between the devices, and a study of the repeatability over ten switching events are presented.

### 5.3.3.1 A Representative Measurement

A voltage induced IMT was used to change the return loss of a device from 0 dB when the VO<sub>2</sub> was in the semiconducting state to about -10 dB when the VO<sub>2</sub> was in the metallic state. The device was first measured at a dc bias of 0V then the voltage was increased in 2V steps until the measured current reached the SMU compliance level set at 10mA, in this case at a source voltage of 20 V, indicating that the VO<sub>2</sub> was in the metallic state (Figure 5.10). At this maximum voltage, the metallic state reflection was measured. The results are shown as a representative measurement. From these measurements, the change in return loss between the semiconducting and metallic state can be determined and the impedance can be calculated.

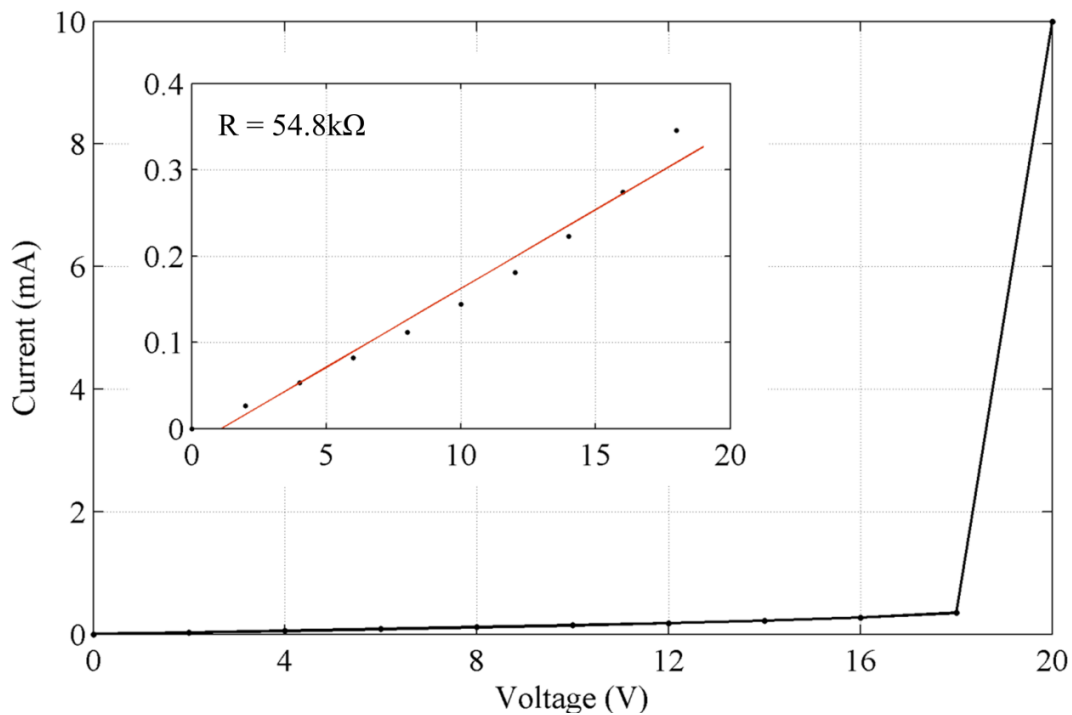
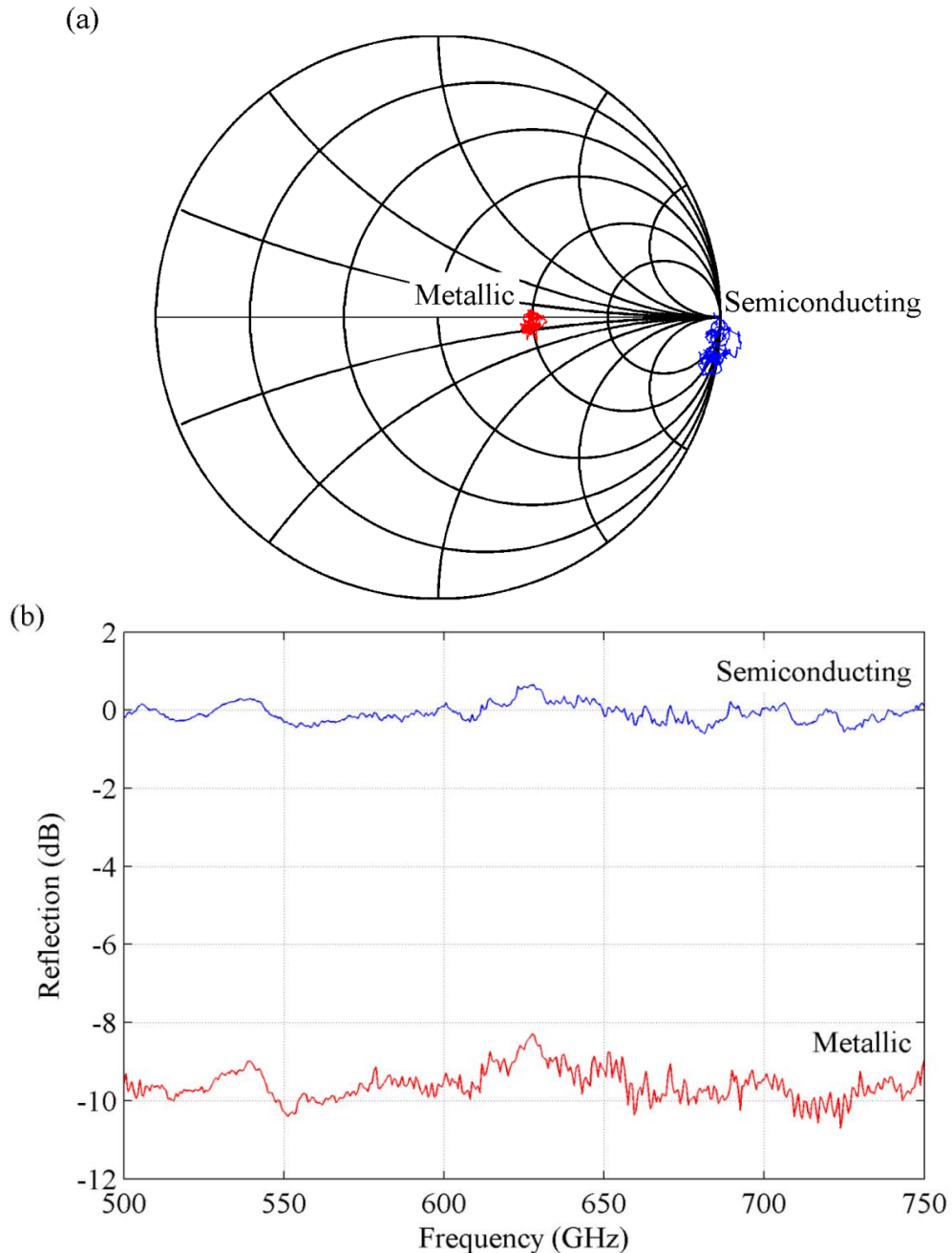


Figure 5.10: Electrically induced IMT transition for the DUT. After the VO<sub>2</sub> undergoes the IMT, the SMU is limited by its compliance at 10 mA. The inset shows the semiconducting portion of the data with the linear regression used to find the mean dc resistance.

The return loss decreased from approximately 0 dB in the semiconducting state to a mean value of -9.4 dB in the metallic state (Figure 5.11b). The average change in phase between the metallic and semiconducting states was  $2.78^\circ$  and is fairly constant across the band (Figure 5.11c). In the metallic state, the phase ranges from about  $-6^\circ$  at 500 GHz to  $-16^\circ$  at 750 GHz. The change in phase is largely explained by the capacitance between the end of the center conductor and the ground metal on the far side of the  $\text{VO}_2$  (more in section 5.3.6). This indicates that the  $\text{VO}_2$  film itself is primarily resistive.



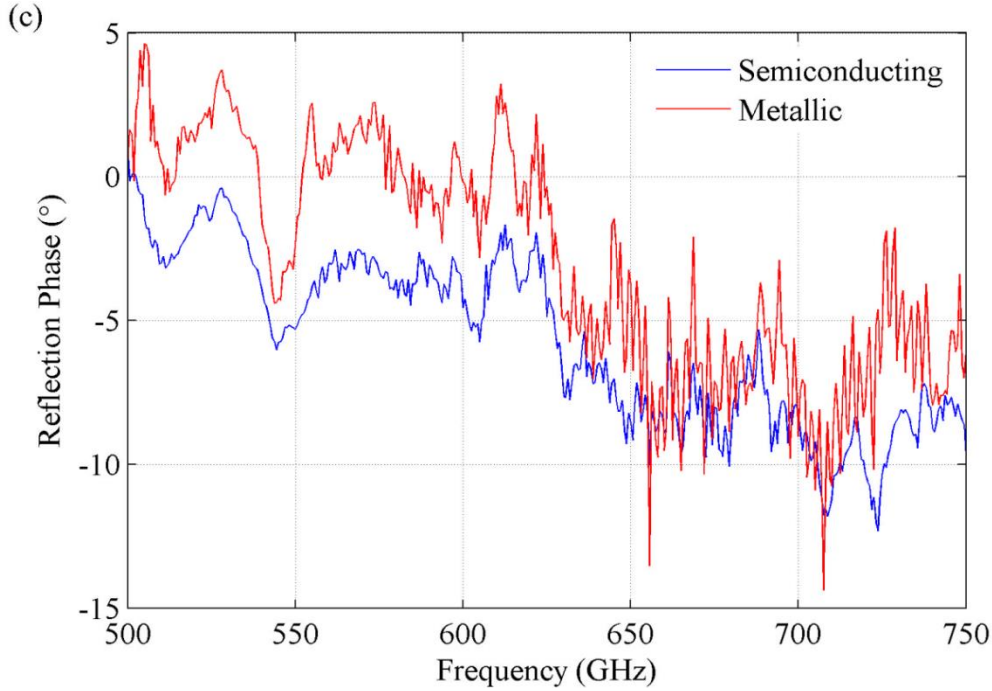


Figure 5.11: The results for a typical one-port VO<sub>2</sub> switch in the semiconducting and metallic state. (a) A Smith chart representation of the data. (b) The magnitude and (c) phase in the semiconducting and metallic states.

The impedance of the VO<sub>2</sub> film in the metallic state can be calculated from the WR-1.5 measurements (Figure 5.12). Equation 5.2 shows the expression for calculating impedance where  $Z_0$  is the normalizing impedance, in this case 50  $\Omega$ , and  $\Gamma$  is the measured reflection coefficient.

$$Z = Z_0 \frac{1 + \Gamma}{1 - \Gamma} \quad (5.2)$$

The mean metallic resistance across the band was 98.47  $\Omega$  and the mean reactance was -13.66  $\Omega$ . The reactance is associated with the capacitance between the center conductor and the ground plane at the far end of the VO<sub>2</sub> film (see section 5.3.6). Based on this calculation, the sheet resistance of the VO<sub>2</sub> is 200  $\Omega/\text{sq.}$ , which is twice the value used when designing this device. The difference between the measured and design values could be caused by many factors. The resistance of the VO<sub>2</sub> film in the design was chosen based on resistivity – temperature ( $\rho$ -T) measurements made on a different wafer grown with the same growth parameter settings. Small variations in the actual growth parameters could lead to a slightly different film thickness and resistivity. Additionally, the structures for the  $\rho$ -T measurements were made using slightly different fabrication procedure, which can affect the film resistance as shown in chapter 3. Lastly, the metallic state resistivity was measured at a temperature well past

the transition temperature; however, the metallic state data in this measurement is taken at the first voltage the reaches the current compliance (10 mA). If the compliance were not reached, the resistivity may have continued to decrease as voltage continued to increase. The measurement was limited because continuing to increase voltage in the metallic state can cause permanent damage to the device. The magnitude of the change in return loss could be increased significantly by properly matching the VO<sub>2</sub> thin film metallic resistance to that of the measurement system. Using the sheet resistance found in this measurement, the size of the VO<sub>2</sub> thin film should be one quarter square to minimize return loss in the metallic state.

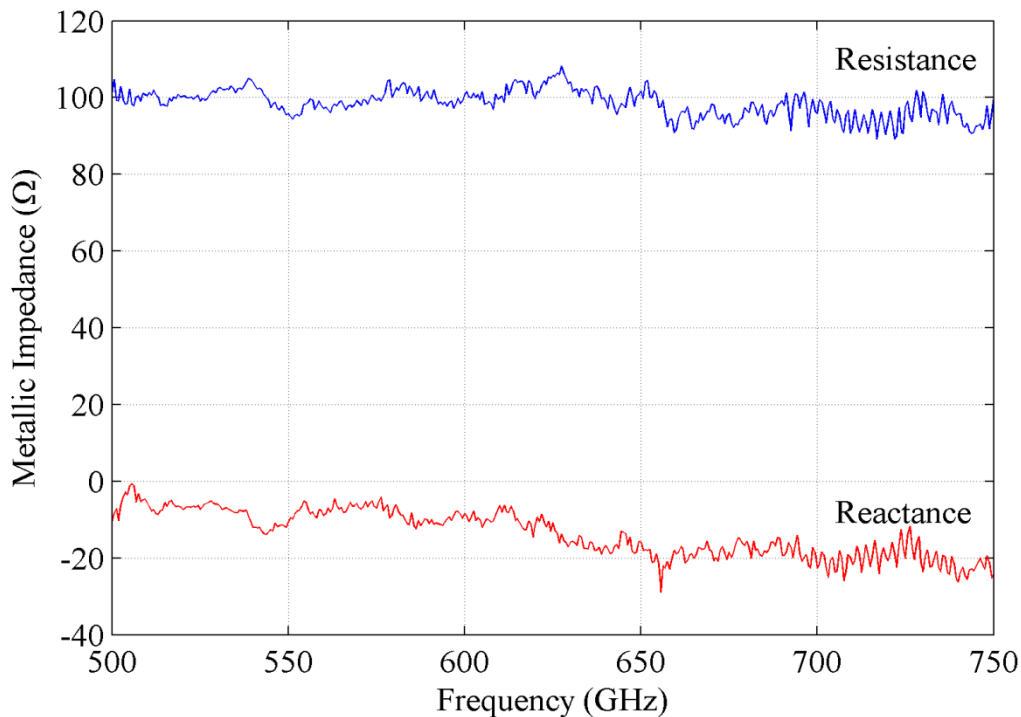


Figure 5.12: The resistance and reactance of the VO<sub>2</sub> film in the metallic state.

The semiconducting state impedance cannot be calculated accurately because its impedance is three orders of magnitude greater than the port impedance of the measurement system. With such a large mismatch, the difference between 10 kΩ and 1 MΩ is less than 0.05 dB. Instead, the average semiconducting state resistance was calculated by applying a linear regression to the dc voltage-current data when the device was in the semiconducting state. A resistance of 54.8 kΩ was calculated and included resistance from the probes (Figure 5.10, inset). The probe resistance varies from 30 kΩ to 1 MΩ and appears in parallel with the DUT giving an estimated DUT resistance in the semiconducting state between 20 and 50 kΩ.

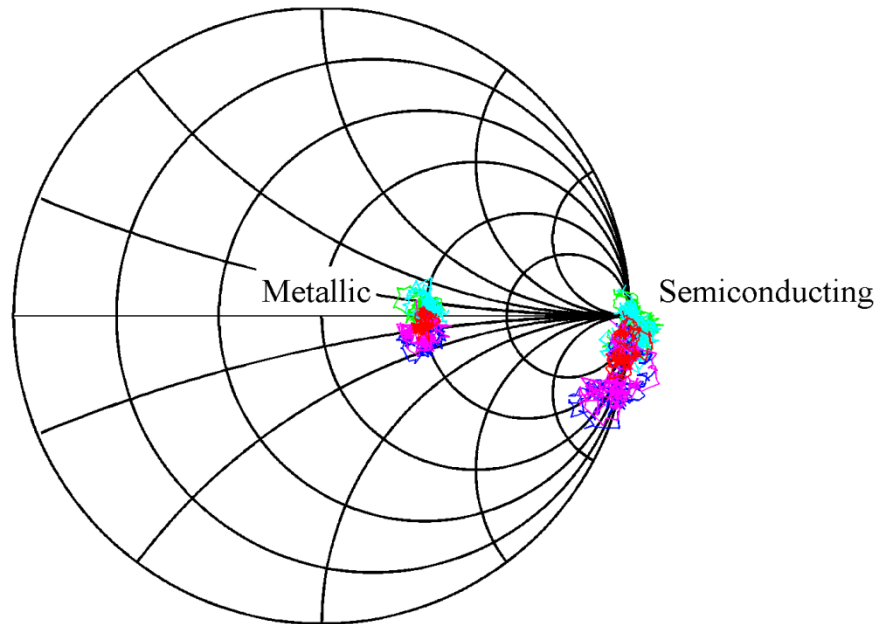
### 5.3.4 Uniformity of Return Loss for Multiple Devices on a Single Wafer

Five identical VO<sub>2</sub> devices on a single wafer were measured and the results compared to assess the uniformity between devices (Figure 5.13). This is an important consideration for potential circuit architectures that incorporate multiple devices into a switching array. The VO<sub>2</sub> transitioned from the semiconducting to the metallic state at 20V (2V step size) for four of the devices and 18V for one of the devices. The results are summarized in Table 5.1. The error range represents one standard deviation from the mean value. The change in magnitude is consistent to better than 3%. The phase variation between devices is a result of the exact probe location, which can vary by about  $\pm 5 \mu\text{m}$ . The low variation between different devices on the same wafer is important for array applications where many devices with the same characteristics are desirable.

Table 5.1: The average magnitude and phase of five devices in the semiconducting and metallic state.

	<b>Magnitude (dB)</b>	<b>Phase (°)</b>	<b>Resistance (<math>\Omega</math>)</b>	<b>Reactance (<math>\Omega</math>)</b>
Semiconducting	$-0.0528 \pm 0.272$	$-13.64 \pm 4.70$	N/A	N/A
Metallic	$-9.424 \pm 0.523$	$-10.43 \pm 5.85$	$99.34 \pm 4.67$	$-13.67 \pm 6.93$
Average change	$-9.371 \pm 0.318$	$+3.21 \pm 2.55$		

(a)



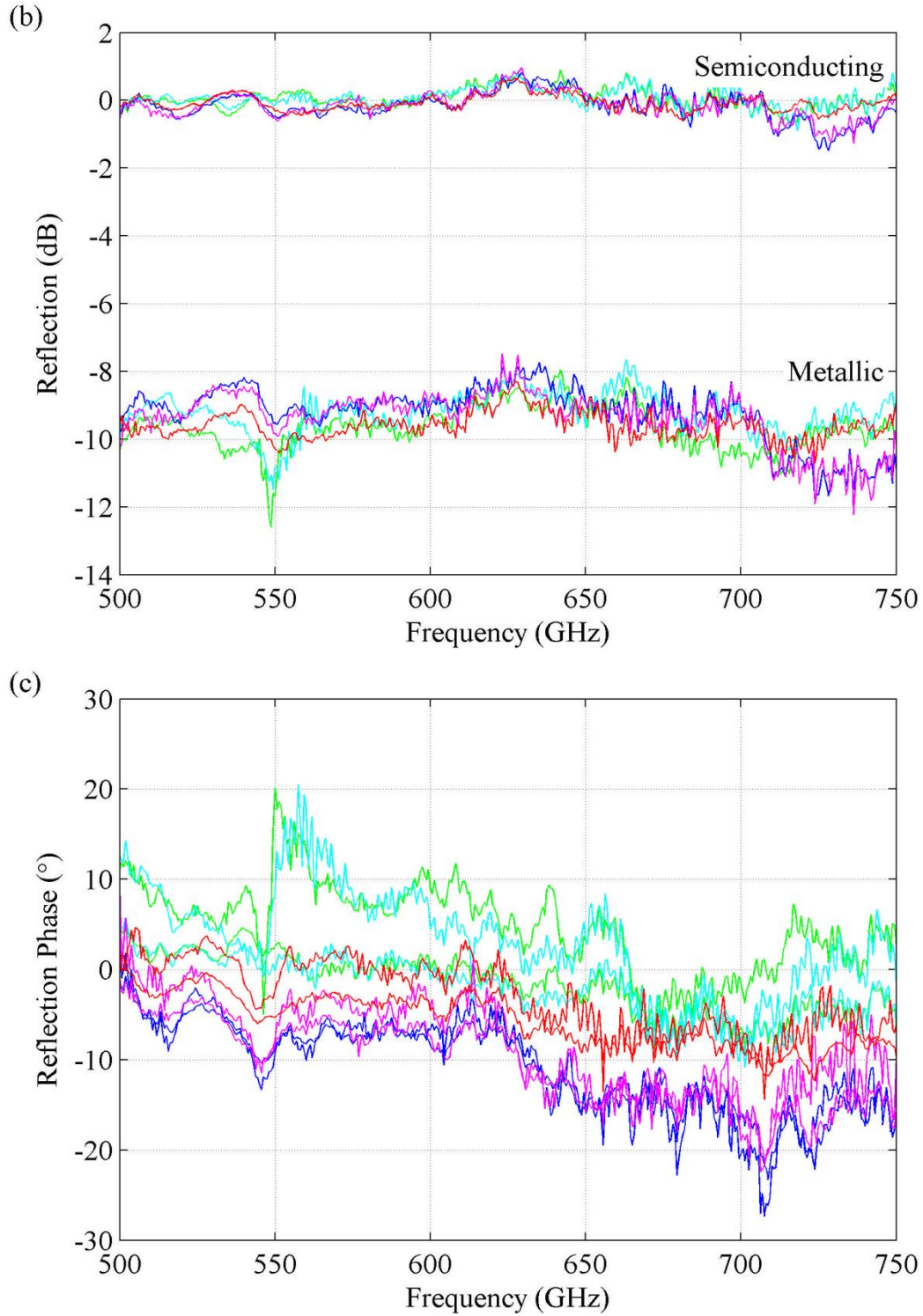


Figure 5.13: The results for five different one-port VO<sub>2</sub> switches on a single wafer. (a) A Smith chart representation of the data. (b) The magnitude and (c) phase in the semiconducting and metallic states.



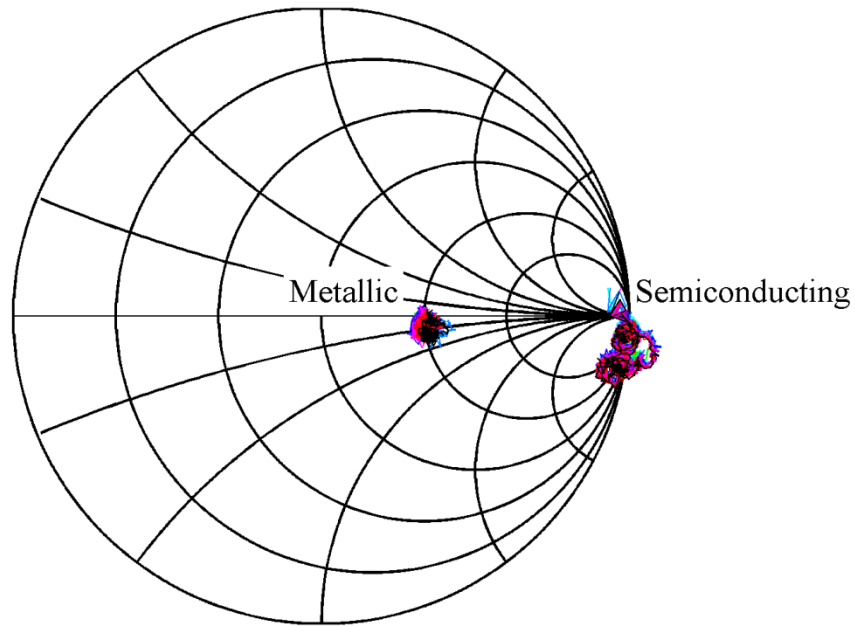
### 5.3.5 Repeatability Characterization of a Single Device

To assess the repeatability of a single device, nine repeated measurement were performed without moving the probes and the results compared (Figure 5.14). The magnitude of the return loss over the nine sweeps had an average change (between the metallic and semiconducting states) of  $9.235 \pm 0.226$  dB (Figure 5.14b). The phase was slightly less consistent with an average change of  $-1.375^\circ \pm 1.491^\circ$  (Figure 5.14c). In eight of the measurements, the metallic state phase was less than the semiconducting state while for the final sweep the opposite was true. The results are summarized in Table 5.2.

Table 5.2: The magnitude and phase in the semiconducting and metallic state for nine sweeps of the same devices.

	<b>Magnitude (dB)</b>	<b>Phase (<math>^\circ</math>)</b>	<b>Resistance (<math>\Omega</math>)</b>	<b>Reactance (<math>\Omega</math>)</b>
Semiconducting	$-0.102 \pm 2.88$	$-6.339 \pm 3.187$	N/A	N/A
Metallic	$-9.337 \pm 0.374$	$-4.963 \pm 3.847$	$99.57 \pm 3.69$	$-17.23 \pm 6.15$
Average change	$-9.235 \pm 0.226$	$+1.375 \pm 1.491$		

(a)





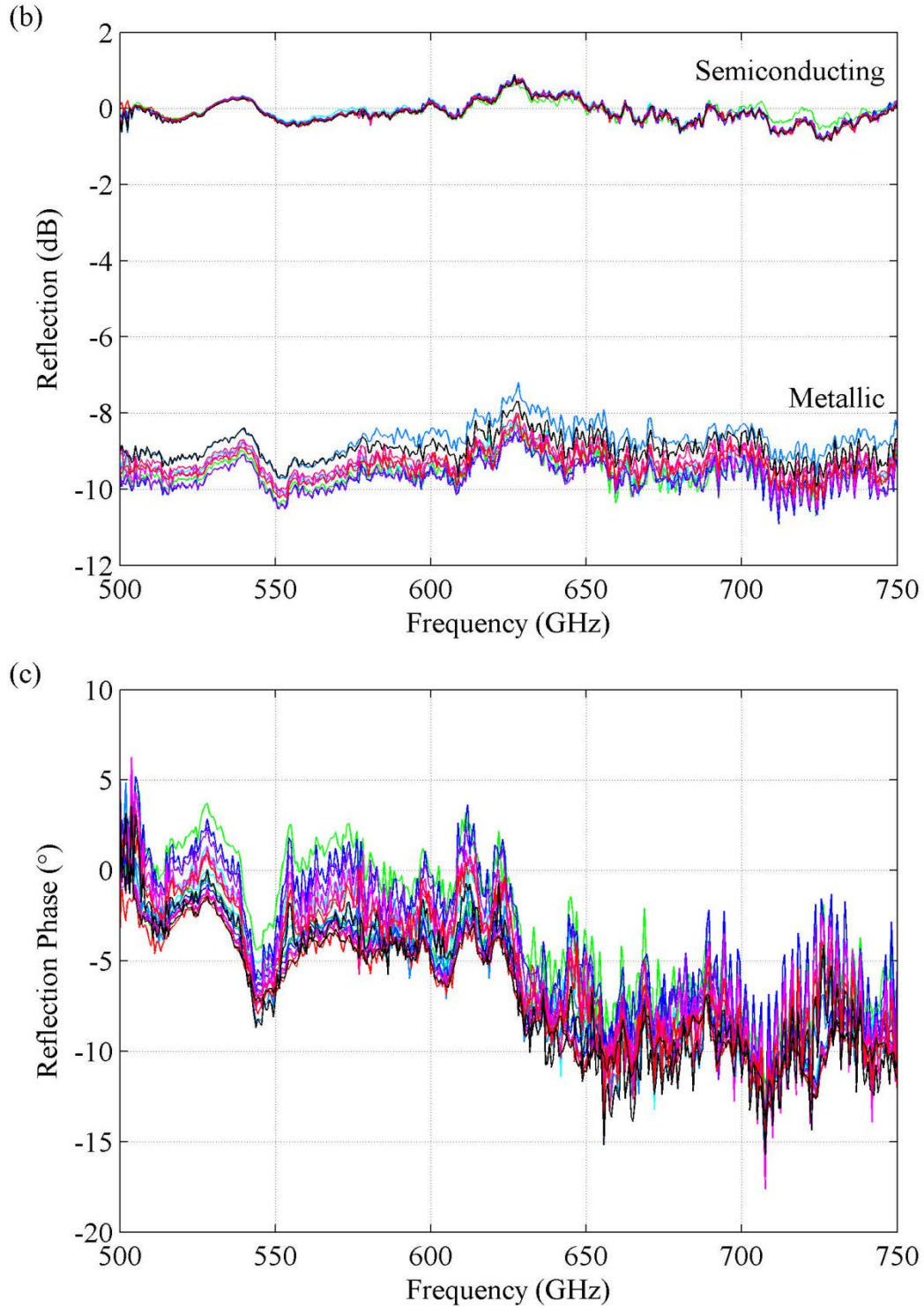


Figure 5.14: The results for nine back-to-back sweeps on a single device. (a) A Smith chart representation of the data. (b) The magnitude and (c) phase of the reflection in the semiconducting and metallic states. The sweep order starts at green (grayscale lightest) through red then black (grayscale darkest).

The current was measured for each voltage step during the data collection (Figure 5.15). On the 1<sup>st</sup> sweep, the VO<sub>2</sub> transitioned into the metallic state at 20V and returned to the semiconducting state at 10V. The voltage at which the semiconductor to metal transition (increasing voltage) occurred decreased with each subsequent measurement; however, the metal to semiconductor transition (decreasing voltage) remained constant across eight measurements. On the ninth sweep, the metal to semiconductor transition occurred at 2V. The device became an open circuit during the tenth sweep and that data is not included. The increase in the size of the hysteresis loop coupled with the failed tenth sweep likely indicates damage to the VO<sub>2</sub> during the ninth sweep followed by catastrophic damage in the tenth sweep (Figure 5.16). The repeatability of the transition is important for the lifetime of a device. While the change in magnitude was repeatable over multiple transitions, the lifetime (number of cycles) needs improvement.

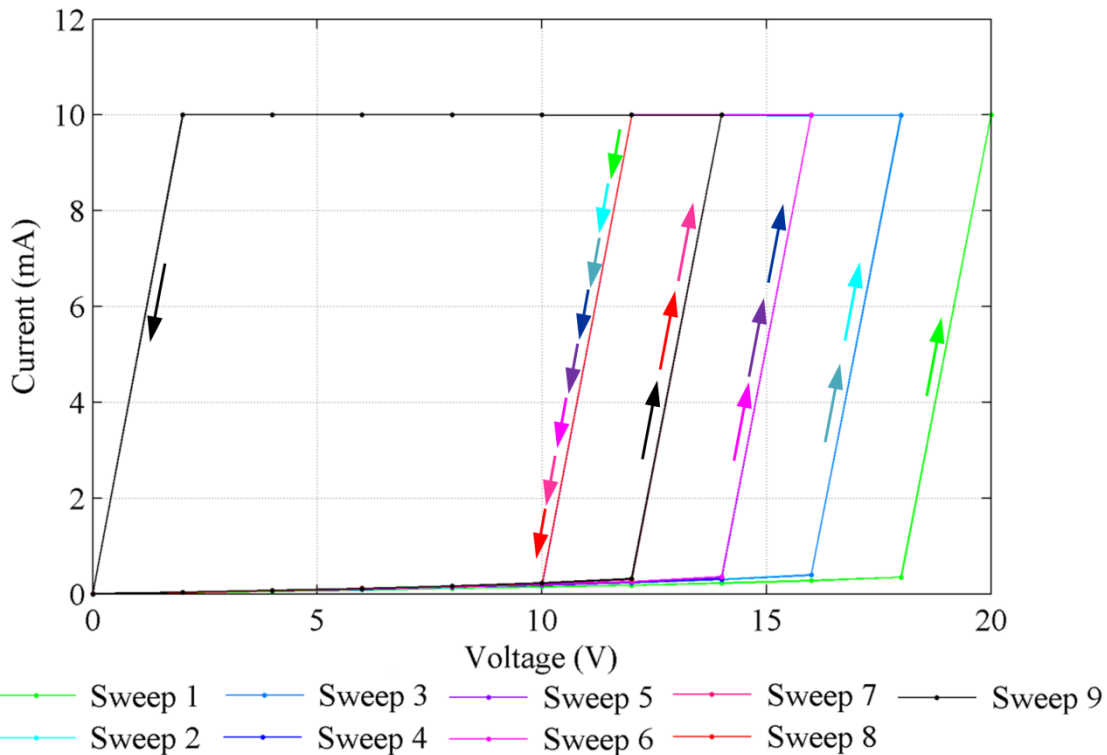


Figure 5.15: The bias voltage and resulting dc current for nine consecutive sweeps. The arrows indicate increasing or decreasing voltage and the hysteretic nature of the VO<sub>2</sub>. The voltage step size was 2V so there are likely smaller changes in critical voltage between sweeps. The final sweep (black) had a much larger hysteresis.

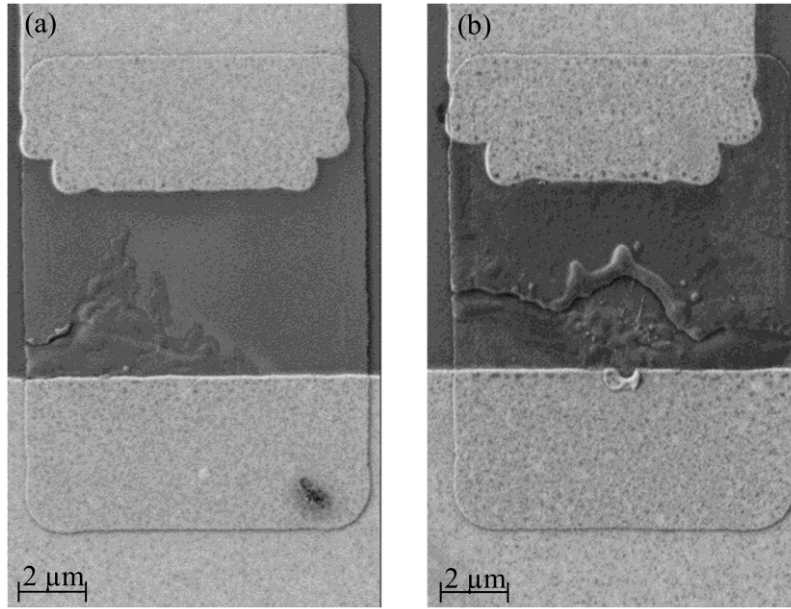


Figure 5.16: SEM image of two different devices that were (a) permanently damaged and (b) destroyed during measurements. The device in (a) shows the damage similar to that expected after the ninth sweep and (b) shows the destruction of a device similar to that caused by the tenth sweep.

### 5.3.6 Broadband Potential

As was seen in the presented measurements, the resistance of the  $\text{VO}_2$  films is not dependent on the frequency. Moreover, the change in phase between the metallic and semiconducting states was negligible at  $1.32 \pm 1.49^\circ$  (Figure 5.17) and phase change across the band was about  $-10^\circ$  in both states. The change in phase is associated with the shape of the device and, in particular, with the distance from the end of the center conductor to the ground plane that terminates the  $\text{VO}_2$  film. To verify this assertion, the one-port structure without the  $\text{VO}_2$  film was simulated in Ansoft HFSS (Figure 5.18). The simulation results showed the same decrease in phase across the band as the device but shifted by  $8^\circ$ . The electrical length of a  $5 \mu\text{m}$  (length of the  $\text{VO}_2$ ) long CPW line with the dimensions used in the device is  $7.8^\circ$  at the center frequency as found using ADS LineCalc. When the  $7.8^\circ$  electrical length is subtracted from the HFSS results for all frequencies, the simulated and the measured phase results agree (Figure 5.19). This indicates that phase shift seen in the device measurements is a result of the device structure and not intrinsic to the  $\text{VO}_2$  film. The  $\text{VO}_2$  film is nearly purely resistive making it attractive for use in broadband devices.

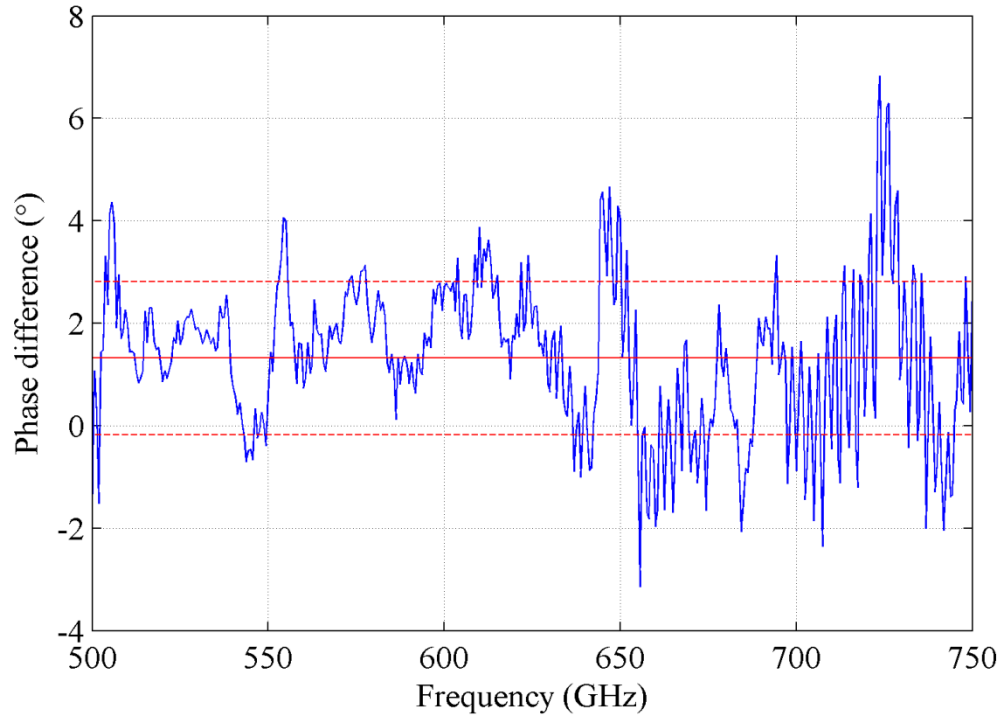


Figure 5.17: The average change in phase with the mean (red solid line) and standard deviation (red dashed line) indicated.

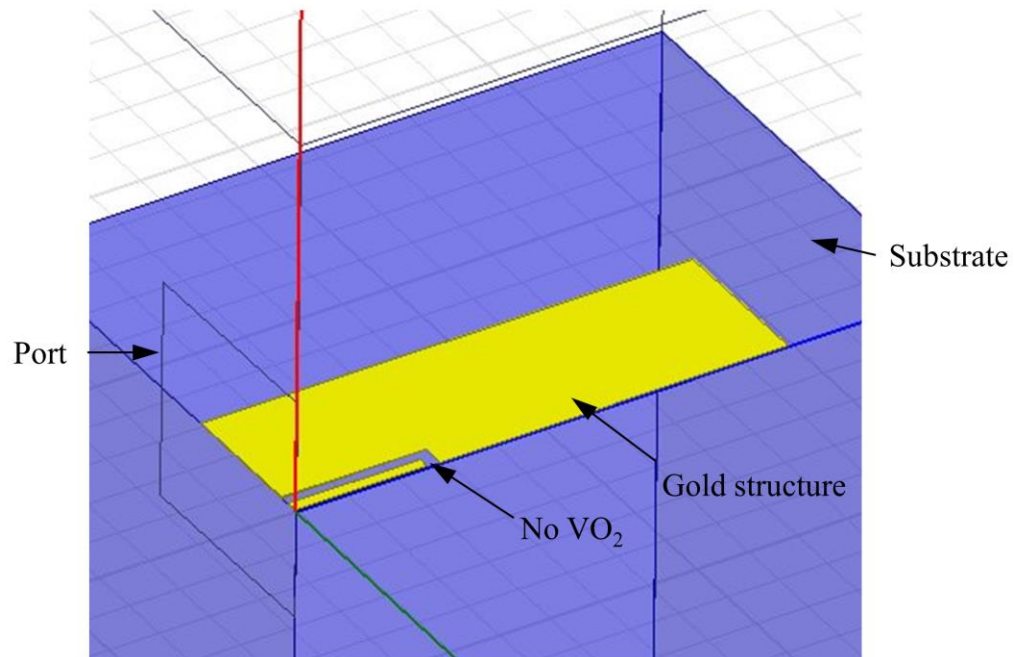


Figure 5.18: HFSS simulation structure. Note that there is not  $\text{VO}_2$  present in this simulation.

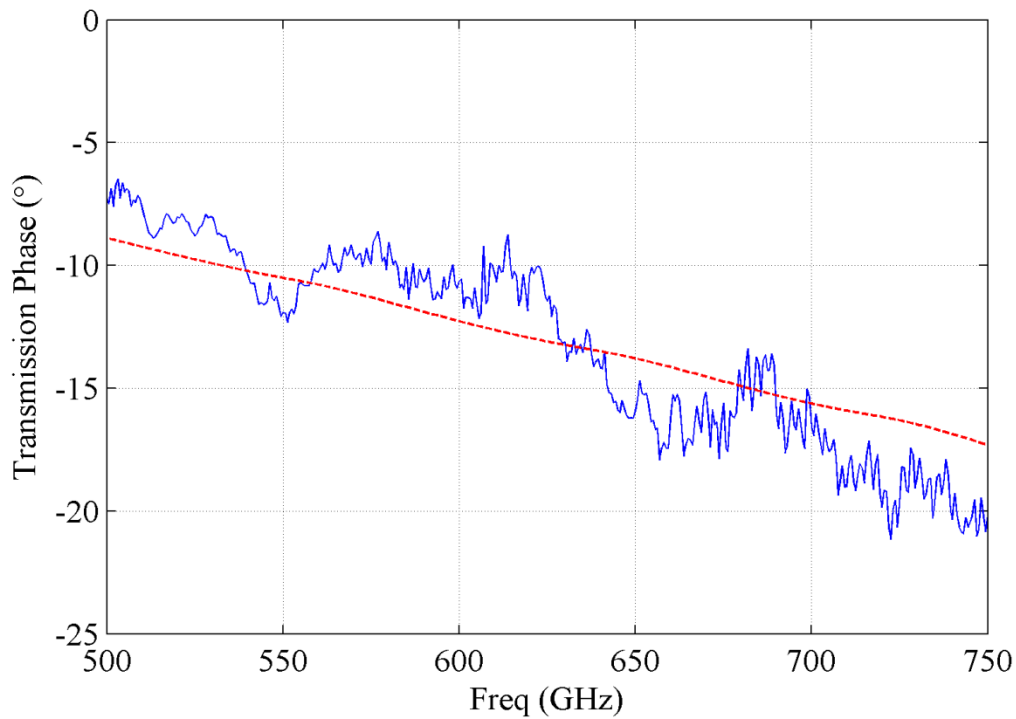


Figure 5.19: The phase of the VO<sub>2</sub> device in the semiconducting state (blue solid) and the phase of the simulated structure without the VO<sub>2</sub> film (red dashed).

### 5.3.7 Summary of One-Port Device Results

The voltage-induced IMT in vanadium dioxide has been demonstrated and characterized on-wafer for the first time over the WR-1.5 (500—750 GHz) band. The return loss of the device changed by about 10 dB and the resistance of the device in the metallic state was found to be approximately 100  $\Omega$ . These results were consistent across multiple devices indicating that such a device could be integrated into an array (see chapter 6). Moreover, the VO<sub>2</sub> is almost purely resistive with very little associated reactance. The reactance present is a result of the device geometry and not the VO<sub>2</sub> itself. This feature is important in broadband applications such as switchable calibration standards.

## 5.4 Two Port VO<sub>2</sub> On-Wafer Switch

Two different size two-port switches utilizing the VO<sub>2</sub> IMT to change between an on and off state were fabricated simultaneously with the one port device (Figure 5.20). The switches consisted of a one half square VO<sub>2</sub> film connecting the center conductor of two CPW lines. Each device had a CPW impedance of 50  $\Omega$ ; however, the CPW dimensions were different. In both designs, the width of the VO<sub>2</sub> film was equivalent to the width of the center conductor and the length was chosen such that the VO<sub>2</sub> retained its half square dimension, resulting in a different length and volume. The insertion loss when the VO<sub>2</sub> was in the metallic and semiconducting states was measured. The results are presented.

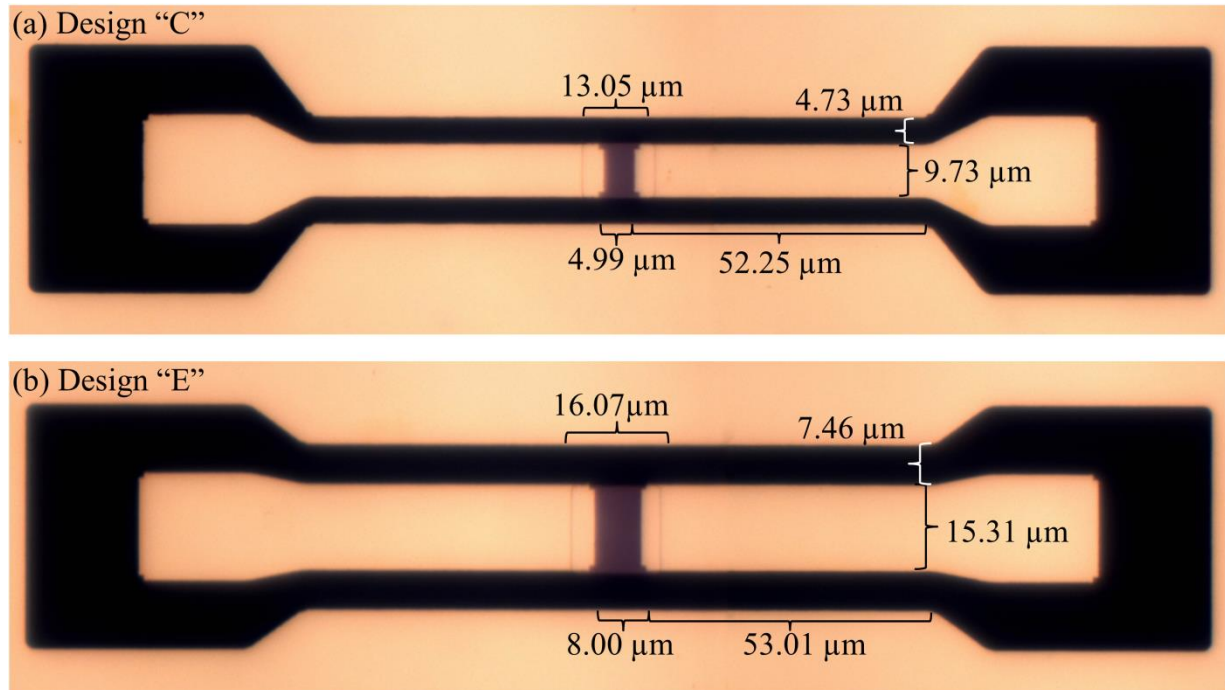
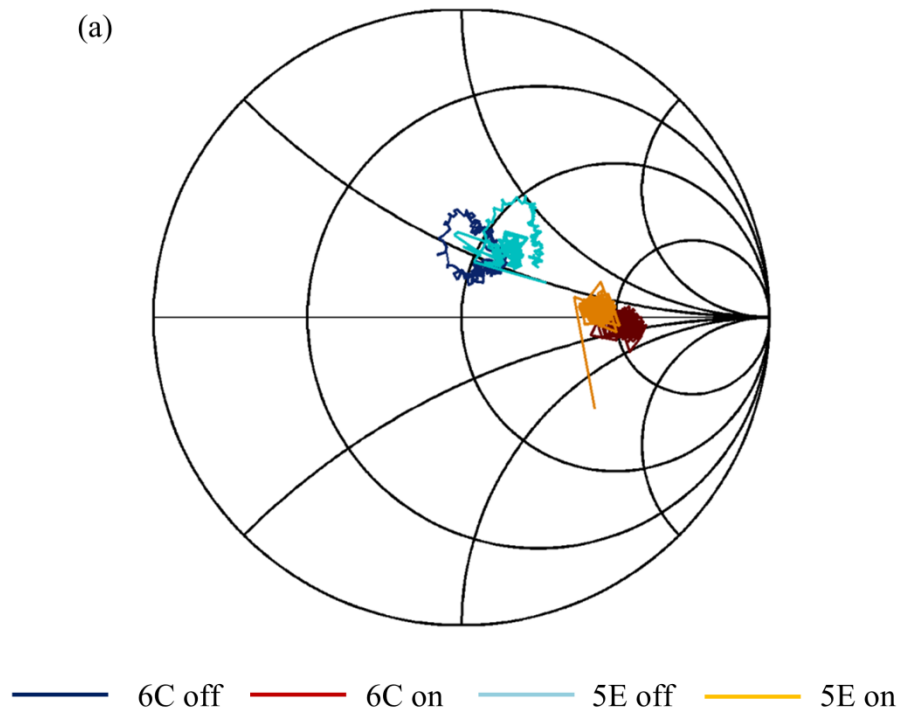


Figure 5.20: Optical images of the two-port device configurations. (a) The smaller device, design "C". (b) The large device, design "E".

### 5.4.1 Insertion Loss in the VO<sub>2</sub> Semiconducting and Metallic State

A voltage-induced IMT in the VO<sub>2</sub> film caused a change in transmission (insertion loss) in the VO<sub>2</sub> switch from 500 to 650 GHz (Figure 5.21). Above 650 GHz, the semiconducting state exhibited a sudden increase in transmission. The smaller device, “C”, had a 9.86 dB change in insertion loss when the switch was turned from the “off” (semiconducting) to the “on” (metallic) state. The IMT for the larger device, “E”, exhibited a change in magnitude of transmission of 4.78dB, or about half that of the smaller device.





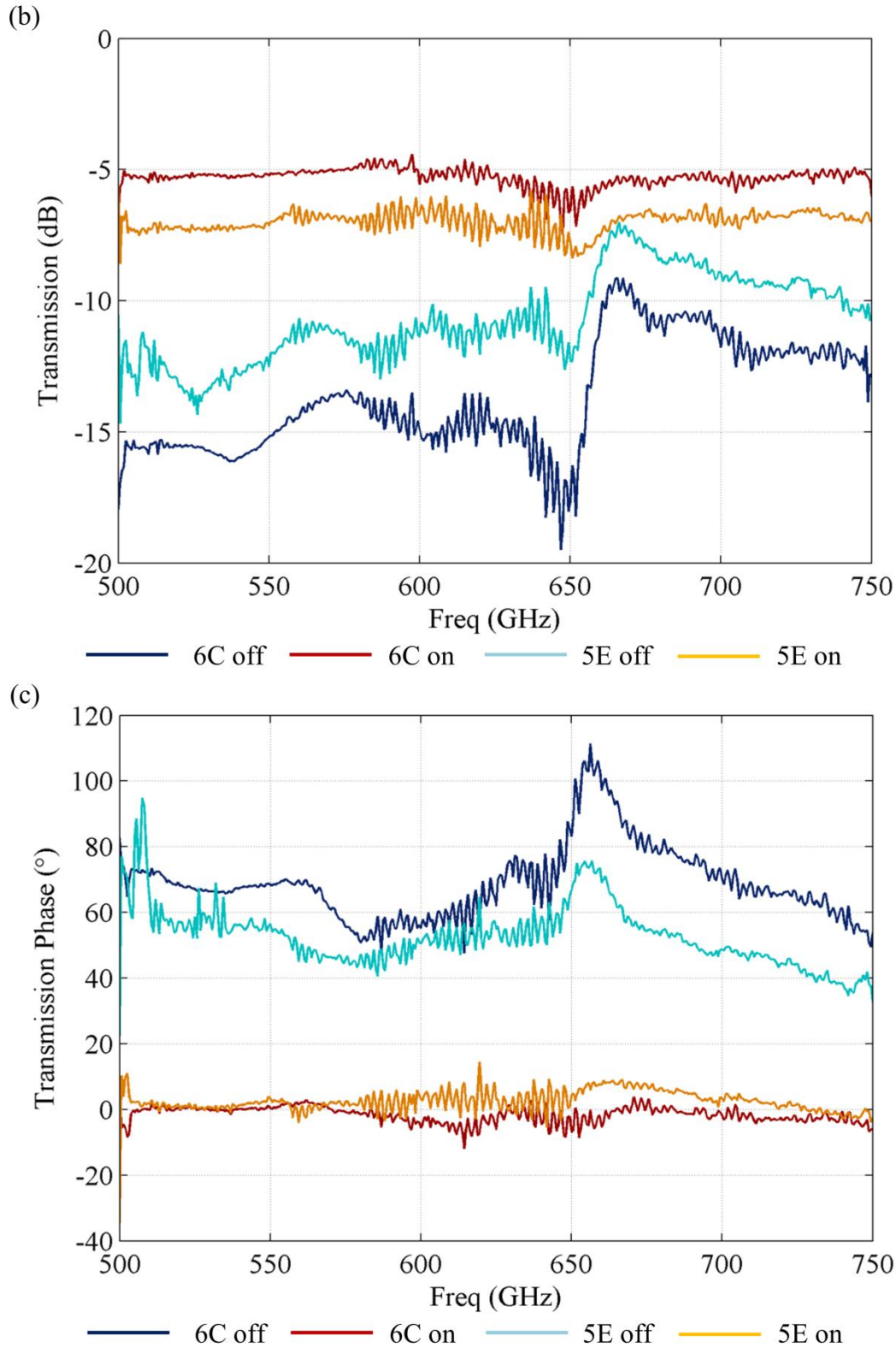
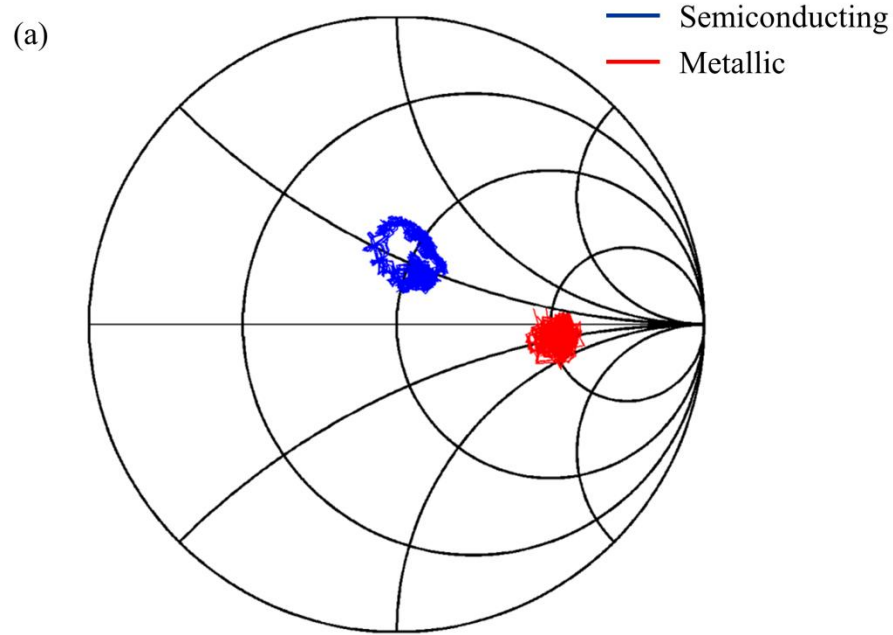


Figure 5.21: The “on” (metallic) and “off” (semiconducting) transmission for the “C” and “E” design two-port switches. (a) A Smith chart representation of the data. (b) The magnitude and (c) phase of each design in each state.



### 5.4.2 Repeatability of a Single Device over Multiple Switching Events

The repeatability of the switch over multiple switching events was tested. For practical use, the switch needs to be turned on and off multiple times. A single design “C” device was switched nine times and the insertion loss was measured in each state every time (Figure 5.22). The mean metallic state transmission was  $-5.33 \pm 0.0554$  dB and the mean semiconducting state transmission was  $-15.19 \pm 0.0741$  dB. The small standard deviation in transmission between measurements indicates that the switch was consistent over several iterations.



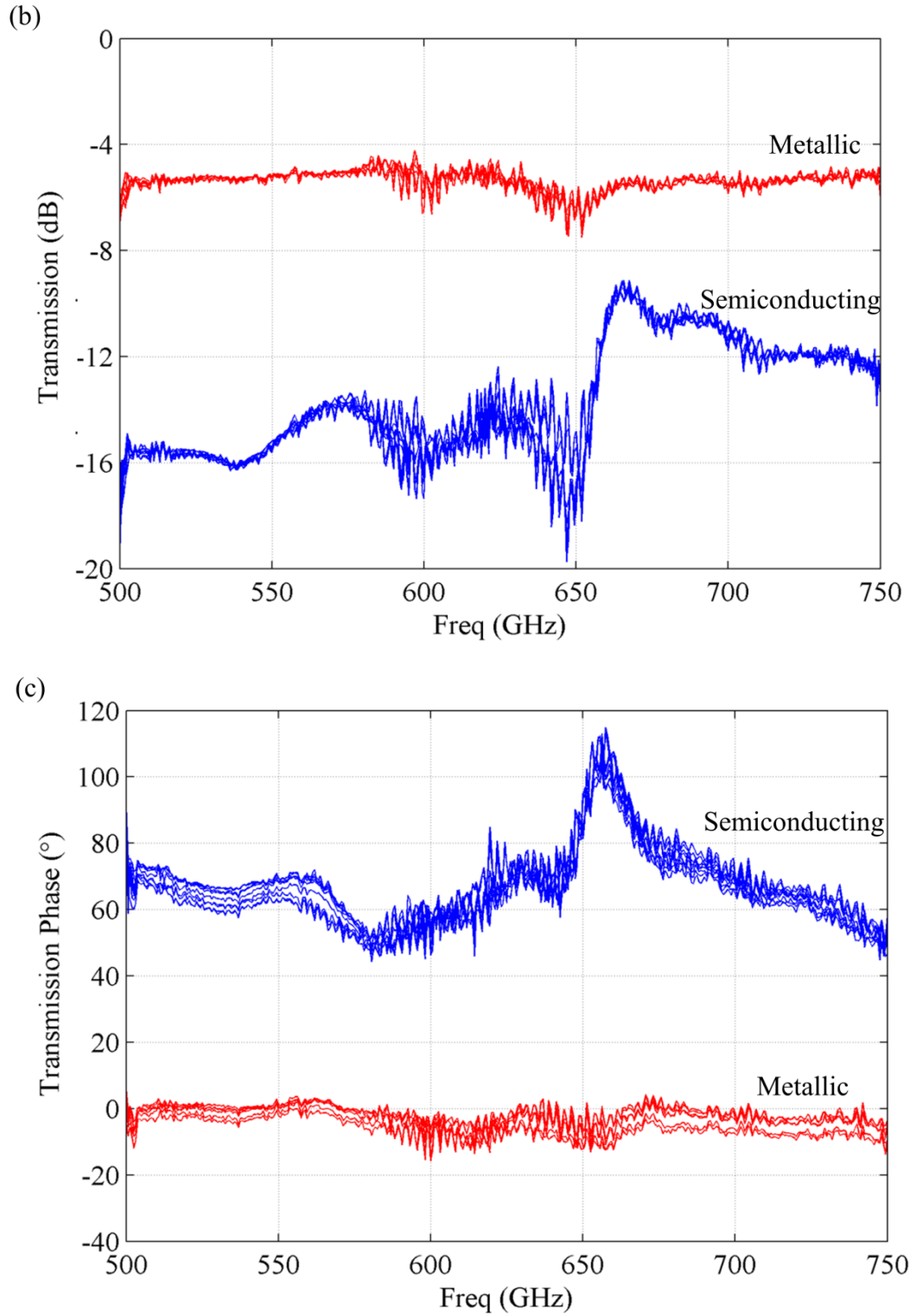
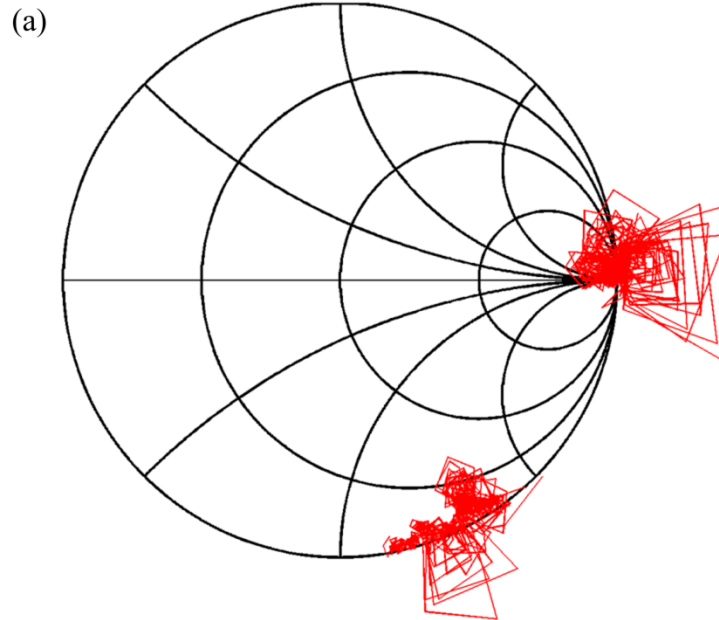


Figure 5.22: A single design “C” device switched measured nine times. (a) A Smith chart representation of the data. (b) The magnitude and (c) phase in each state.

### 5.4.3 Calibration

Calibration of the two-port measurement setup was performed using the thru-reflect-line (trl) method. The trl method is beneficial in that it can be done on-wafer using the same CPW dimensions as the DUT and can establish the reference plane via the length of the thru instead of de-embedding through modeling or calculation. The reflect is an open circuit that reflects back the signal with a magnitude of one. The line is an offset of the thru with a length known to within one quarter effective wavelength for the transmission line structure. From these measurements, the error boxes for the probes and the transmission line up to the reference plane can be calculated and removed from the measurements. These standards were included on the wafer with the two-port devices. After completing the calibrations, the thru and line were re-measured to check the accuracy of the calibration. Despite several attempts, there was still some error in the calibration. Some possible causes for this error are probe position during calibration and measurements, crosstalk between the probes, or substrate effects; however, further investigation is left as a future work.



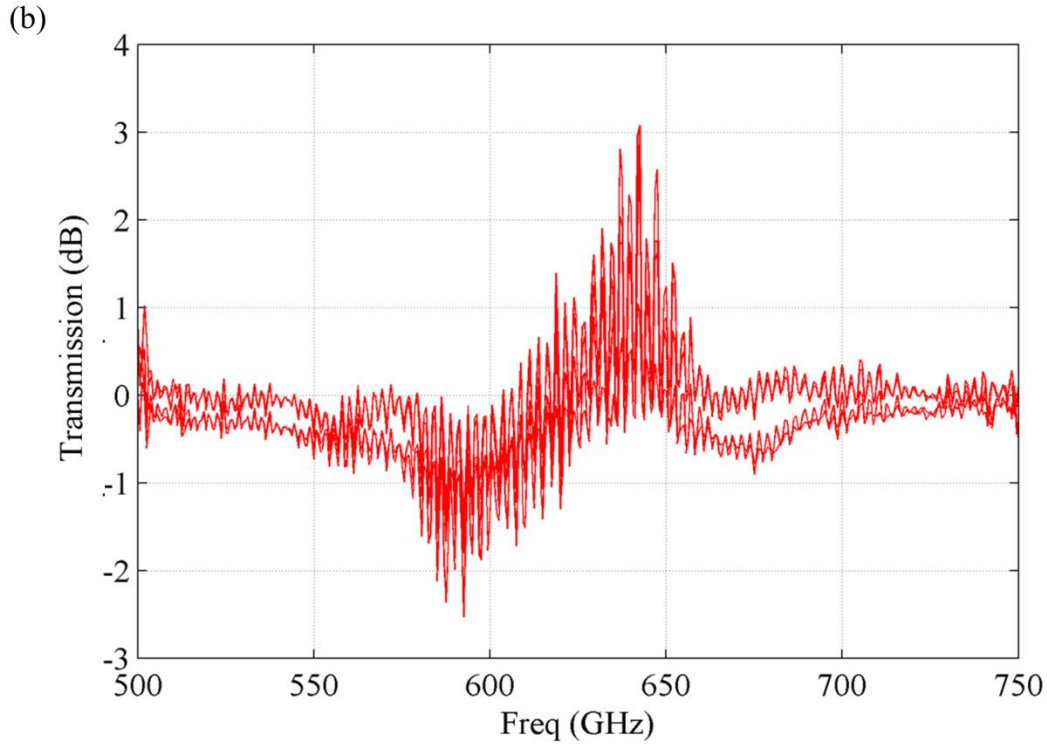


Figure 5.23: The thru and line calibration standards as measured after calibration. (a) The Smith Chart representation of the data shows that the magnitude of the transmission sometimes exceeds one indicating error in the calibration. (b) The magnitude of the thru and line transmission is  $\pm 2$  dB. Ideally, these measurements should be 0 dB.

## 5.5 Conclusion/summary

This chapter presented the first on-wafer WR-1.5 measurements of VO<sub>2</sub> devices. The proof-of-concept devices demonstrated the potential for VO<sub>2</sub> thin films switches. The voltage-controlled IMT in a VO<sub>2</sub> thin film load was shown to modulate the return loss in a one port device and the insertion loss in a two port switch.

The one port device demonstrated the effect of the IMT of a VO<sub>2</sub> load on the return loss of a device. The results were used to calculate the metallic state sheet resistance of 200  $\Omega$ /sq. at 500 – 750 GHz, a parameter that is useful in designing future devices. Several devices across a single wafer were measured with similar results indicating consistency across the wafer. This feature is necessary for array applications where individual VO<sub>2</sub> elements could be used to modulate individual pixels.

The two port switch results confirmed that the IMT in the VO<sub>2</sub> could effectively alter the insertion loss between an “on” and “off” state. This feature could be used to make tunable terahertz components such as filters and matching networks. Coupled with the potential for VO<sub>2</sub> to operate at high bandwidths, such devices could significantly increase the bandwidth of a single circuit.

Modulation with 10 dB amplitude was demonstrated in both the one- and two- port devices. The amplitude of the modulation would be increased significantly if the VO<sub>2</sub> load size was adjusted such that the load impedance in the metallic state matched that of the CPW line. The effect of the transition was shown to be consistent between several devices on a single wafer and repeatable over nine events. The VO<sub>2</sub> was shown to be nearly purely resistive indicating high potential for use in broadband devices. The results presented in this chapter indicated that VO<sub>2</sub> thin film is a promising material for switching applications.

- [1] A. Crunteanu, F. Dumas-Bouchiat, C. Champeaux, A. Catherinot, A. Pothier, and P. Blondy, “Microwave switching functions using reversible metal-insulator transition (MIT) in VO<sub>2</sub> thin films,” in *Microwave Conference, 2007. European*, 2007, pp. 12–15.
- [2] T. Driscoll, S. Palit, M. M. Qazilbash, M. Brehm, F. Keilmann, B.-G. Chae, S.-J. Yun, H.-T. Kim, S. Y. Cho, N. M. Jokerst, D. R. Smith, and D. N. Basov, “Dynamic tuning of an infrared hybrid-metamaterial resonance using vanadium dioxide,” *Applied Physics Letters*, vol. 93, no. 2, p. 024101, 2008.
- [3] Y.-G. Jeong, H. Bernien, J.-S. Kyoung, H.-R. Park, H. Kim, J.-W. Choi, B.-J. Kim, H.-T. Kim, K. J. Ahn, and D.-S. Kim, “Electrical control of terahertz nano antennas on VO<sub>2</sub> thin film,” *Opt. Express*, vol. 19, no. 22, pp. 21211–21215, Oct 2011.
- [4] C. Wen, “Coplanar waveguide: A surface strip transmission line suitable for nonreciprocal gyromagnetic device applications,” *Microwave Theory and Techniques, IEEE Transactions on*, vol. 17, no. 12, pp. 1087–1090, 1969.

## Chapter 6: Conclusion and Future Work

In this chapter, the objectives and accomplishments of the research presented in this dissertation are reviewed. The promising VO<sub>2</sub> results are discussed along with a few concerning aspects. Finally, a few ideas for future research directly related to the research presented are proposed.

### 6.1 Review of Research Objectives

Vanadium dioxide films have a variety of potential applications from dc to ultraviolet frequencies. When fabricating these devices, the processes and reagents used can alter VO<sub>2</sub> films yet the processes that effect the VO<sub>2</sub> are not widely published unless they were developed for a specific purpose, such as with an etch process. The effects on the appearance, resistivity, and thickness of a VO<sub>2</sub> film for several common procedures and reagents used in the fabrication of VO<sub>2</sub> devices were investigated and presented.

When designing, fabricating, and testing a device, many different parameters need to be taken into account. One such material property is the contact resistance. In measuring the contact resistance, it was found that the traditional method developed by Shockley [1] and his successors (e.g. [2-4]) was insufficient. A new method to address materials with high thermal coefficients of resistance (TCR) such as VO<sub>2</sub> was developed.

Thirdly, one-port and two-port WR-1.5 switches were demonstrated as sample devices. These devices were used to find several properties of VO<sub>2</sub> films such as impedance at terahertz frequencies and demonstrate potential for broadband uses. These properties, specifically the terahertz impedance, are useful for designing future terahertz devices.

## 6.2 Accomplishments

The accomplishments and results from the research in this dissertation are summarized in list form below.

1. The contact resistance of the interface between VO<sub>2</sub> films and titanium/gold metallization was measured. In the process of performing these measurements, it was found that the tradition method is insufficient. A new method to address the insufficiencies caused by Joule heating in the VO<sub>2</sub> film was developed. This process was used to determine the specific contact resistivity of the VO<sub>2</sub> – metal interface and the results were compared with those from the traditional method.
2. The effects of several common fabrication reagents, O<sub>2</sub> plasma cleaning, and nLOF2020 photolithography on the VO<sub>2</sub> film were investigated and, where applicable, quantified. It was found that NMP and propylene-glycol liftoff procedure and O<sub>2</sub> plasma cleaning clearly alter VO<sub>2</sub> films. Resistivity measurements suggest that acetone will change the film properties. Visual inspection indicates that DI water and photolithography also modify the VO<sub>2</sub> film.
3. The first on-wafer VO<sub>2</sub> measurements at terahertz frequencies were performed and the results presented.
4. A VO<sub>2</sub> load terminating a CPW transmission line was measured in the metallic and semiconducting state. From this measurement,
  - a. The impedance of the VO<sub>2</sub> in the metallic state was calculated at terahertz frequencies, a parameter that is useful in designing future devices.
  - b. Consistency between multiple devices was demonstrating indicating that the VO<sub>2</sub> could be used in array applications.
  - c. Repeatable measurements of a single device were demonstrated.
5. An on-wafer VO<sub>2</sub> switch was demonstrated and shown to be repeatable.
6. The VO<sub>2</sub> films were demonstrated to be mostly resistive at terahertz frequencies. The reactance associated with the devices was shown to be from the device geometry and not the film. This feature is important for future use in very broadband applications.

## 6.3 Future Research

Several research directions based on the research presented in this dissertation are discussed in this section. These include reducing contact resistivity, finding a suitable passivation layer for VO<sub>2</sub> films, improving calibration techniques for terahertz on-wafer measurements, and a quasioptical bowtie array utilizing a VO<sub>2</sub> film as a switching element.

### 6.3.1 Reduce Contact Resistivity

Contact resistance adds unnecessary loss to a device and can prevent it from performing adequately. The specific contact resistivity presented in this research for a VO<sub>2</sub>/Ti/Au structure was high at  $10^{-2} \Omega\text{-cm}^2$ . It was previously shown that VO<sub>2</sub>/metal specific contact resistivities  $10^{-6} \Omega\text{-cm}^2$  can be achieved by using a different metal for the contact pads [5]. Specific contact resistivities of  $10^{-7} \Omega\text{-cm}^2$  are typical for GaAs devices [6]. Changing the contact metal or adhesion layer metal, doping the VO<sub>2</sub> near the contact, improving fabrication technique, and improving VO<sub>2</sub> surface cleanliness should all be investigated as ways to reduce contact resistance and optimize a VO<sub>2</sub> device.

### 6.3.2 Passivation Layer for VO<sub>2</sub> Thin Film

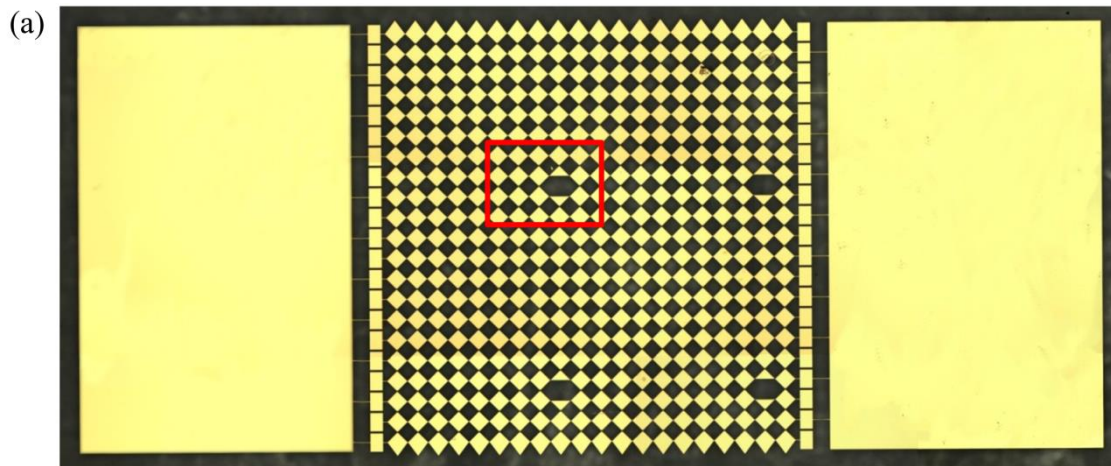
The results from chapter 3 in this dissertation demonstrated that several fabrication processes can alter the properties of VO<sub>2</sub> film including etching and oxidizing the film. As VO<sub>2</sub> thin films become thinner, the effects of these alterations will become more prominent. An in-situ passivation layer during VO<sub>2</sub> thin film growth would be ideal as it would prevent the film from being contaminated after it is removed from the deposition chamber. If an in-situ method is not available, a passivation layer should be applied directly after removing the film from the chamber and before building the device. The passivation layer should not degrade the performance of the VO<sub>2</sub> such as reducing the magnitude of the change in resistivity between the



semiconducting and metallic states or decreasing the sharpness of the transition. A few attempts at passivation of the VO<sub>2</sub> films grown at the University of Virginia were investigated and found to degrade the quality of the VO<sub>2</sub> transition. Other researchers use materials such as Si<sub>3</sub>N<sub>4</sub> [7] and SiO<sub>2</sub> [5] although many researchers do not mention use of a passivation layer.

### 6.3.3 VO<sub>2</sub> Modulated Bowtie Antenna Array

Switching arrays consisting of bowtie antennas with a VO<sub>2</sub> element at the feed point have been designed and fabricated. Each array consists of several bowtie antennas with VO<sub>2</sub> loads located at the antenna feed. There are three different size arrays consisting of 10x10, 20x20, or 50x50 elements. Additionally, several single elements surround each array to find critical switching values (current, voltage, temperature, optical irradiation) for the individual elements. The bowties have an angle of 90 degrees and a diagonal length of 71.7 μm. The VO<sub>2</sub> is located at the antenna feed and has a size of 3 μm by 3 μm or 5 μm by 5 μm, depending on the array (Figure 6.1).



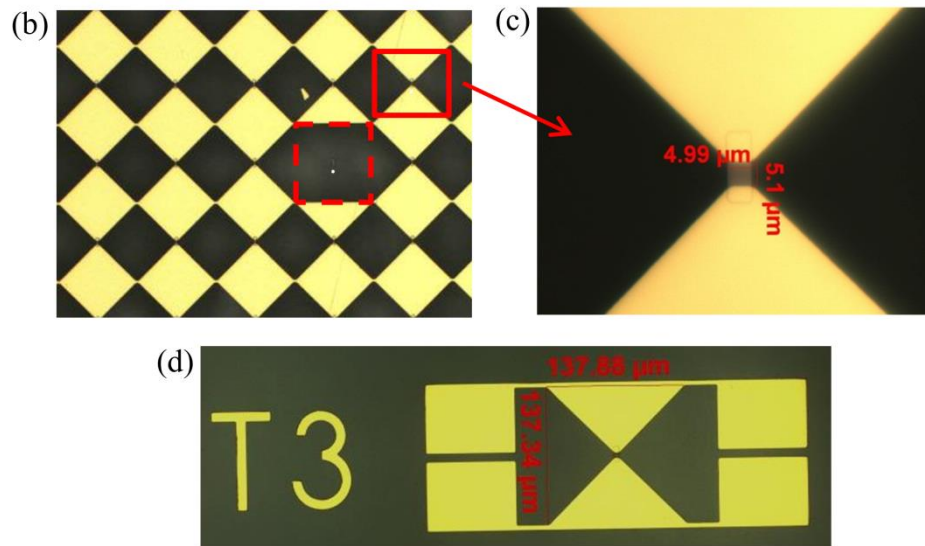


Figure 6.1: A VO<sub>2</sub> – bowtie antenna array. (a) A 20x20 μm array showing the large gold contact pads on either side. (b) A higher magnification view of a portion of the array showing the bowties antennas and how they are connected. The dashed line square shows a defect in the mask. The solid line square indicates a single bowtie antenna. (c) A higher magnification image of a single bowtie and VO<sub>2</sub> feed. (d) A single antenna and feed for testing the bowties. The four pads are for four point probe measurements.

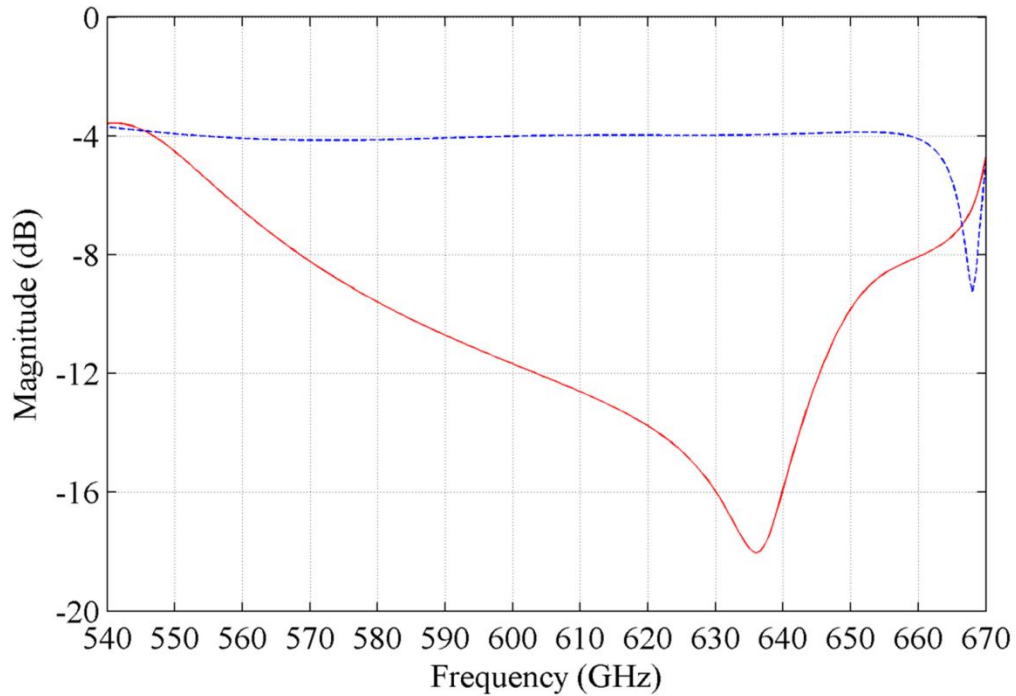


Figure 6.2: Ansoft HFSS simulation of the transmission of the bowtie antenna array when the VO<sub>2</sub> is in the semiconducting (red solid) and metallic (blue dashes) states.

The bowtie antenna arrays are designed to modulate the transmission of a 600 to 650 GHz signal by more than 8 dB. A 100nm thick VO<sub>2</sub> thin film located at the antenna feed point should shift the resonance frequency of the bowtie antenna such that the antenna reflects the THz signal when the VO<sub>2</sub> is “off” state (semiconducting) and transmits the signal when it is in the “on” state (metallic) (Figure 6.2).

The antennas are connected at the corners of the bowties to allow for biasing. The arrays consist of  $n$  rows of  $n$  series elements where  $n$  is the array dimension in number of antennas. The rows are connected in parallel with each other. The devices were designed to be switched using a voltage bias; however, after measuring the RF devices and seeing how easily they could be damaged after transitioning into the metallic state, there is worry that the elements toward the end of the series chains would not be transitioned before the voltage at the start of the chain caused the VO<sub>2</sub> devices to be destroyed. As a result of this concern, the antenna will be tested using an external heat source to induce a thermal transition [8] or optical illumination for photoinduced transition [9].

The terahertz signal will be generated and measured using Virginia Diodes, Inc. (VDI) frequency extension modules interfaced with a vector network analyzer. The VDI modules transmit the terahertz signal via rectangular waveguide. The signal will be radiated from the rectangular waveguide, focused onto the array using an off-axis parabolic mirror, reflected or transmitted through the array, then be focused into the rectangular waveguide at the second port using a different off-axis parabolic mirror (Figure 6.3). Feedhorns will be used to couple the quasioptical signal into the rectangular waveguide.

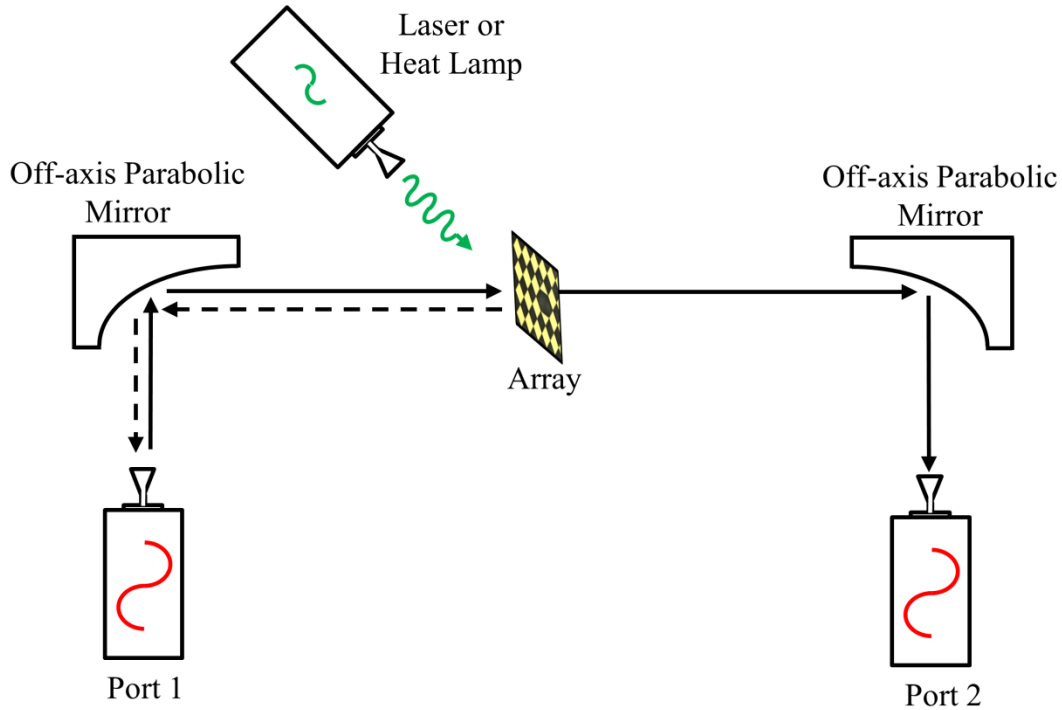


Figure 6.3: Experimental setup for measuring the  $\text{VO}_2$  – bowtie antenna array. The incident signal will be generated at port 1, focused onto the array and either reflected or transmitted depending on the state of the  $\text{VO}_2$ . The transmitted signal will be detected at port 2. The  $\text{VO}_2$  IMT will be induced by a heat lamp or an optical laser signal.

## 6.4 Future Research Summary

A few suggestions for future research directly related to the material in this dissertation have been presented. There are many additional potential that could be developed at the University of Virginia. These include a terahertz mixer, bolometric detector, or novel tunable and broadband circuitry. As the quality and understanding of  $\text{VO}_2$  increases, its applications show a lot of promise in many areas of research.

- [1] W. Shockley, "Research and investigation of inverse epitaxial uhf power transistors," Wright-Patterson Air Force Base, Ohio, Tech. Rep., September, 1964.
- [2] G. Reeves and H. B. Harrison, "Obtaining the specific contact resistance from transmission line model measurements," *Electron Device Letters, IEEE*, vol. 3, no. 5, pp. 111–113, 1982.
- [3] H. Berger, "Models for contacts to planar devices," *Solid-State Electron.*, vol. 15, no. 2, pp. 145 – 158, 1972.
- [4] G. S. Marlow and M. B. Das, "The effects of contact size and non-zero metal resistance on the determination of specific contact resistance," *Solid-State Electronics*, vol. 25, no. 2, pp. 91 – 94, 1982.
- [5] K. Martens, I. P. Radu, S. Mertens, X. Shi, L. Nyns, S. Cosemans, P. Favia, H. Bender, T. Conard, M. Schaekers, S. De Gendt, V. Afanas'ev, J. A. Kittl, M. Heyns, and M. Jurczak, "The VO<sub>2</sub> interface, the metal-insulator transition tunnel junction, and the metal-insulator transition switch on-off resistance," *Journal of Applied Physics*, vol. 112, no. 12, p. 124501, 2012.
- [6] R. Williams, *Modern GaAs Processing Methods*, 2nd ed. Boston: Artech House, 1990.
- [7] H. Wang, X. Yi, and S. Chen, "Low temperature fabrication of vanadium oxide films for uncooled bolometric detectors," *Infrared Physics & Technology*, vol. 47, no. 3, pp. 273 – 277, 2006.
- [8] M. Seo, J. Kyoung, H. Park, S. Koo, H. Kim, H. Bernien, B. J. Kim, J. H. Choe, Y. H. Ahn, H.-T. Kim, N. Park, Q.-H. Park, K. Ahn, and D.-S. Kim, "Active terahertz nanoantennas based on VO<sub>2</sub> phase transition," *Nano Letters*, vol. 10, no. 6, pp. 2064–2068, 2010.
- [9] J. Kyoung, M. Seo, H. Park, S. Koo, H. Kim, Y. Park, B.-J. Kim, K. Ahn, N. Park, H.-T. Kim, and D.-S. Kim, "Giant nonlinear response of terahertz nanoresonators on VO<sub>2</sub> thin film," *Opt. Express*, vol. 18, no. 16, pp. 16452–16459, Aug 2010.

## Appendix A: Permanent Damage to VO<sub>2</sub> Devices

While making dc measurements, many observations about the VO<sub>2</sub> and the measurement technique were made. The VO<sub>2</sub> devices were shown to need protection from the sudden increase in voltage at the transition. Damage to the devices from continuing to increase the bias well past the IMT was observed. Lastly, evidence indicating a need for VO<sub>2</sub> device training is presented. In this appendix, some observations and hypotheses regarding damage to the VO<sub>2</sub> film during measurements are discussed; however, these hypotheses were not tested.

### A.1 Permanent Film Damage and Device Length

While measuring the contact resistance devices, several permanent changes to the film were observed. In some cases, the formation of a filament that does not return to the semiconducting state when the bias is removed could be seen (Figure A.1). The size and severity of the damage increased as the distance between the contact pads increased (Figure A.2a). The switching current bias for the longer devices is lower so in a constant range measurement sweep, the difference between the end current of the sweep and the transition current increases as separation distance increases (Figure A.2b). When the device is not measured far above the current transition, the damage is less noticeable or non-existent.

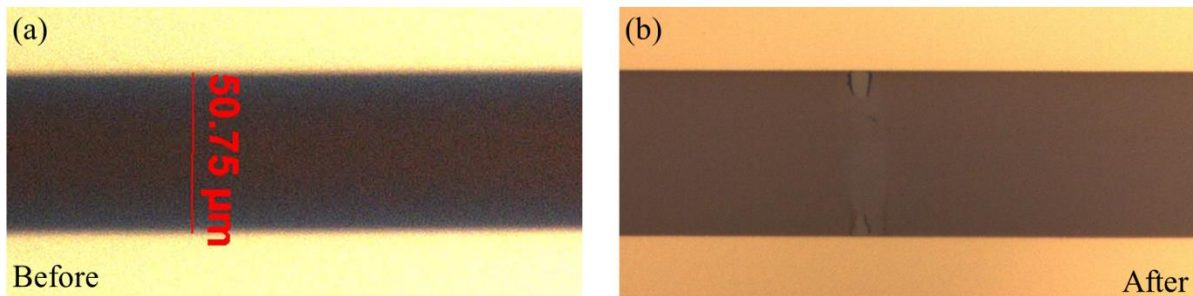


Figure A.1: Permanent filament formation in a VO<sub>2</sub> film. (a) The region before measurements and (b) the same region after measurement.

Alternatively, the devices with a longer separation length have a higher resistance. If resistive heating is playing a role, it is reasonable to conceive that the longer films heat more. It has been shown that the surface of  $\text{VO}_2$  can partially remain in the metallic state after returning to room temperature when it heated above  $152^\circ\text{C}$  as a result of oxygen depletion. At  $252^\circ\text{C}$ , the bulk material is permanently altered. The change in the resistivity at MIT is reduced, the MIT is not as sharp, and the transition temperature is reduced by  $30^\circ\text{C}$ . The crystalline structure is degraded and the surface becomes nearly completely metal. The changes to the bulk material are a result of oxygen loss and effusion along grain boundaries [1]. It is suspected that the local heating in the  $\text{VO}_2$  devices is sufficient to induce some of these effects.

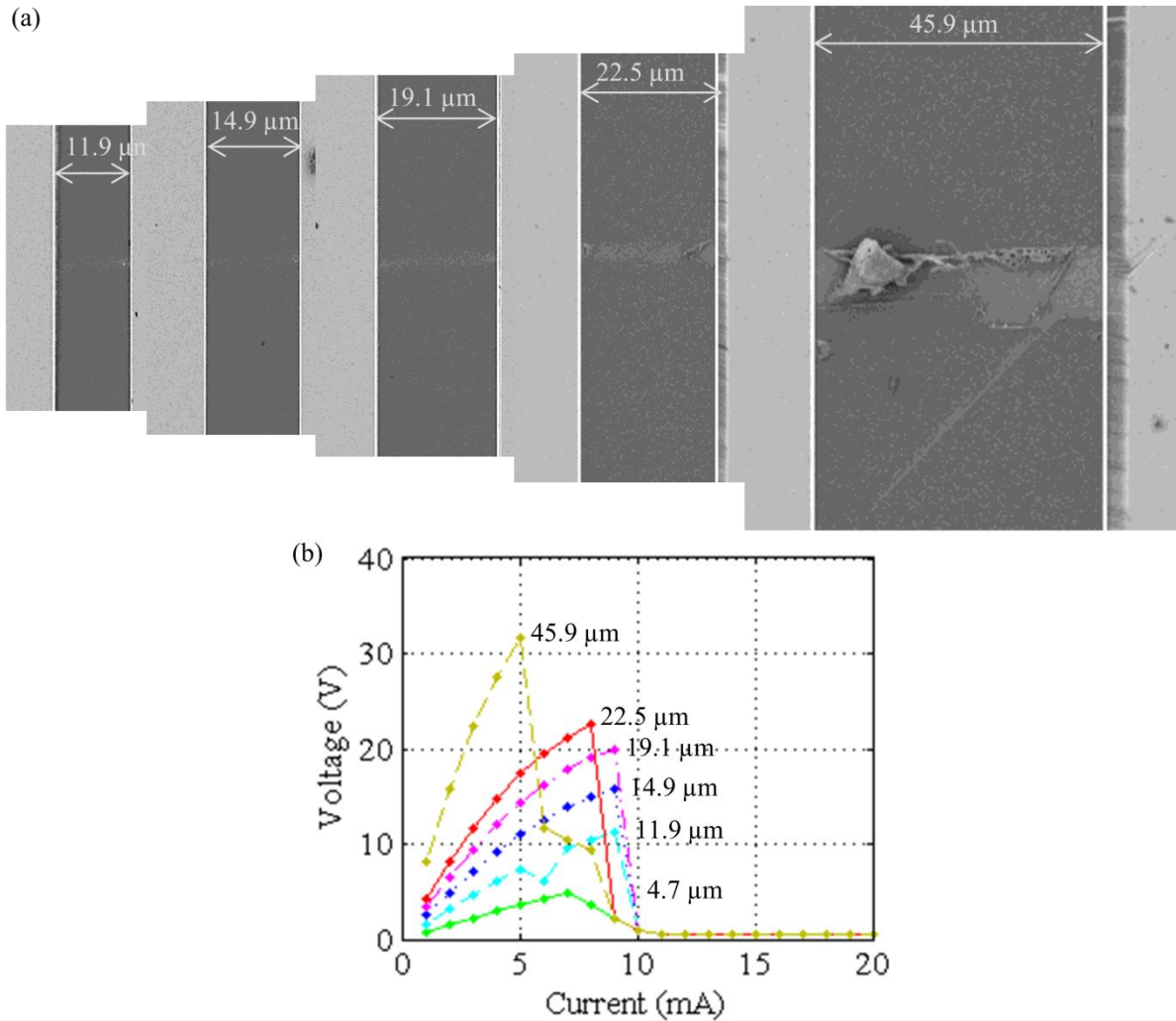
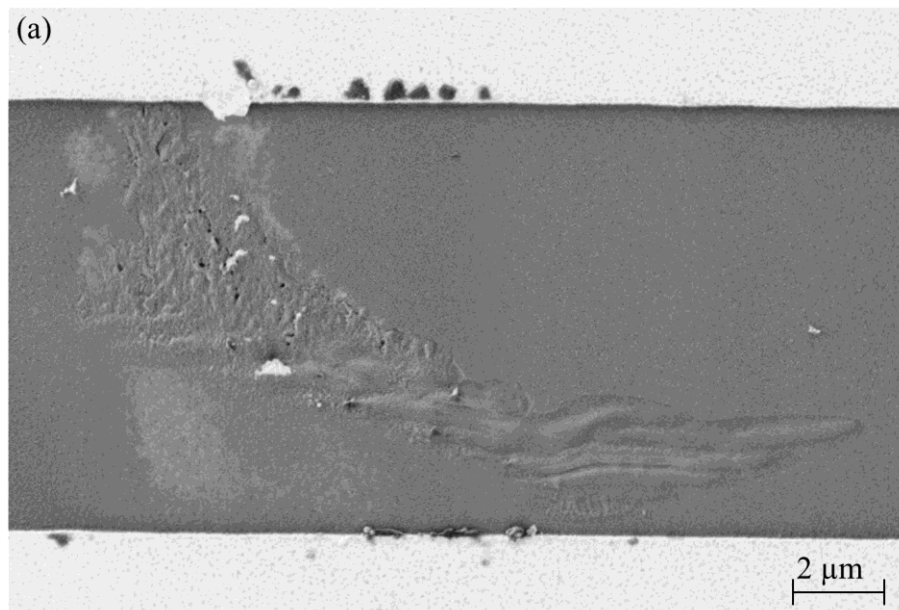


Figure A.2: (a) Post-measurement SEM showing permanent and destructive filament formation. (b) The corresponding IV measurement. The further past transition bias a given separation distance is measured, the more destruction to the material. The  $4.67\ \mu\text{m}$  device had a visible contact edge irregularity and was discounted from the measurements.

## A.2 Appearance of VO<sub>2</sub> Films Permanently Altered during Measurements

The VO<sub>2</sub> films could also be permanently destroyed or “blow” during a measurement. Filaments formation has been observed during the current driven VO<sub>2</sub> IMT [2]. When a metallic filament in the VO<sub>2</sub> film forms between the contacts, the current preferentially flows through the lower resistance region. In some cases, this causes the VO<sub>2</sub> film to be destroyed and the device to behave unexpectedly or become an open circuit. In post-mortem SEM images, the VO<sub>2</sub> can appear to be rippled or starting to delaminate from the substrate. The gold at the edge of the contact can appear darker at the edge of the damage than further from it. In other devices, the gold at the edge of the contacts appears to have melted. Gold droplets are seen condensed on the contact pads in a pattern that radiates from a crater at the contact edge.





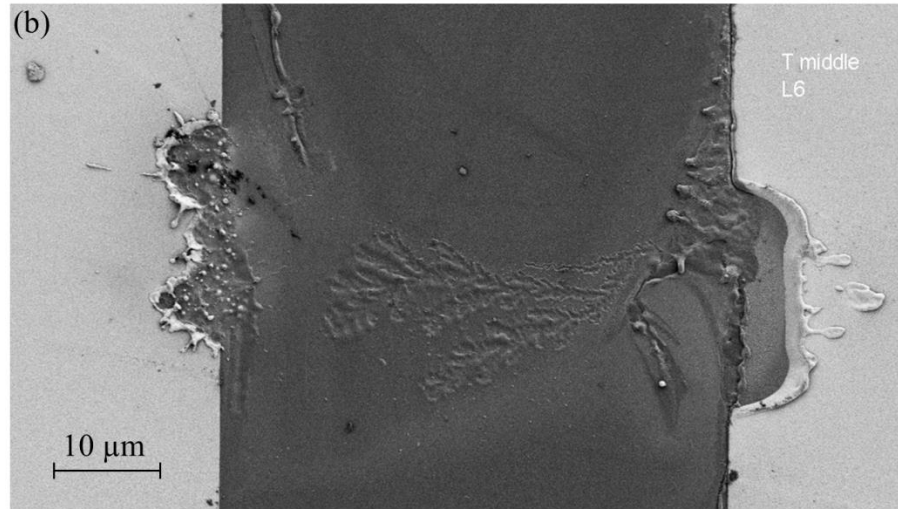


Figure A.3: Damage to VO<sub>2</sub> films during measurement – post-mortem SEM images. (a) The VO<sub>2</sub> film appears rippled and like it may be starting to delaminate from the film. (b) Destruction of the VO<sub>2</sub> film and the gold at the contact pad edges.

Another device appeared to have a line that remained metallic parallel to the contact edge and several damaged filaments perpendicular to the edges. The VO<sub>2</sub> appears to be peeling off from the substrate and curling along the edges of multiple filaments.

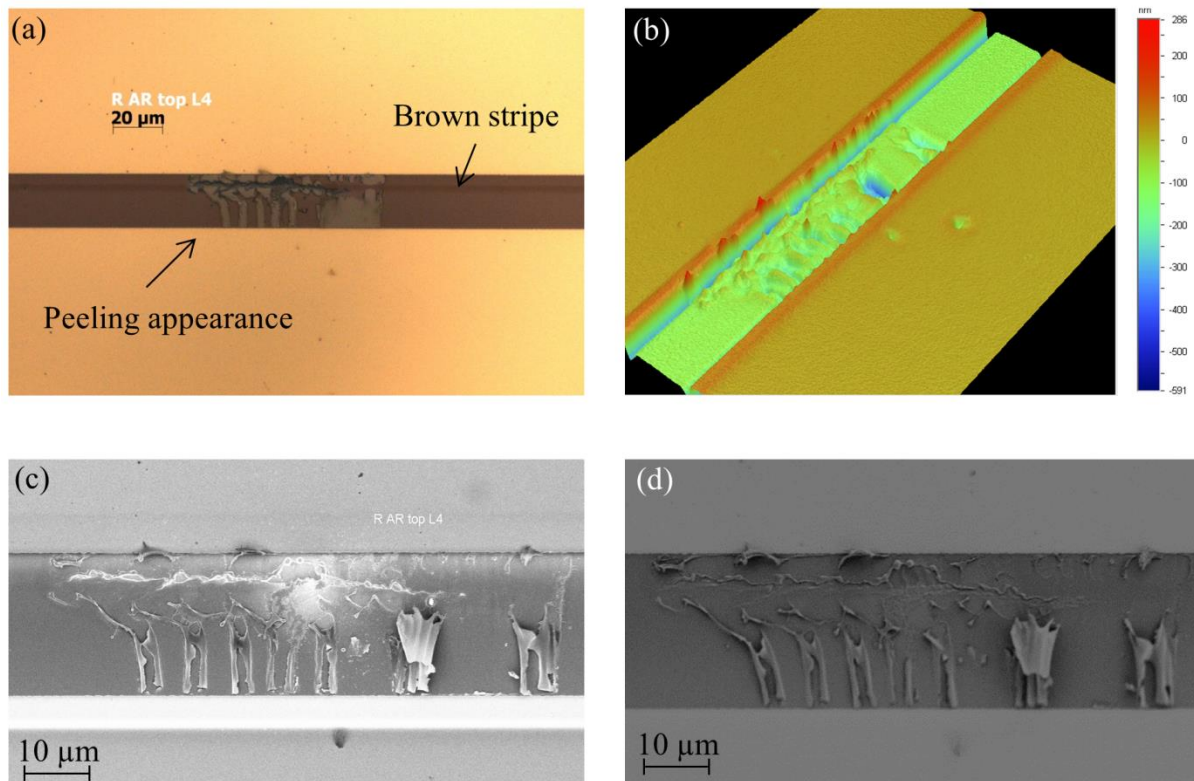


Figure A.4: Another type of damage to the VO<sub>2</sub>. (a) An optical microstrip showing a dark brown stripe parallel to the contact pad. (b) An optical profilometer indicating changes in height (or index of refraction) on the VO<sub>2</sub> surface. (c) In-lens and (d) SE2 SEM images showing what appears to be VO<sub>2</sub> peeling and curling.

In some cases, the destruction that occurred at transition was complete and catastrophic (Figure A.5). The sudden drop in resistance caused a surge in power through the device similar to that of an electrostatic discharge (ESD) event. In both this situation and an ESD event, not only was the  $\text{VO}_2$  destroyed but an area well into the contact pad was peeled away, cratered, and had been melted and the droplets condensed. In these cases, a spark could easily be seen in a low power microscope and thus the timing could be correlated with the transition. This type of destruction could widely be avoided by adding a 1.2 k $\Omega$  resistor between the current output on the Keithley 267 and the probe tip.

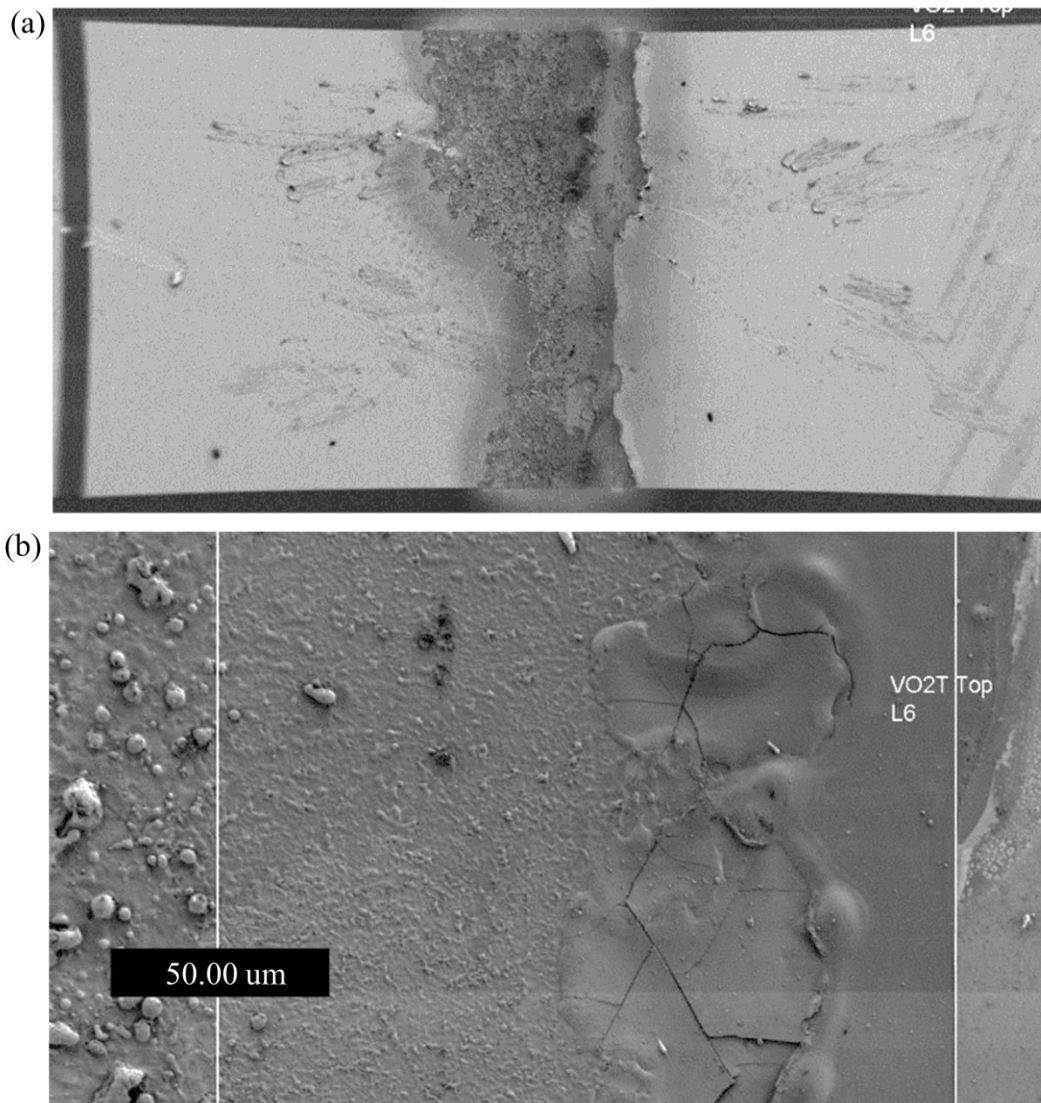


Figure A.5: (a) A low magnification version of a completely destroyed device. For scale, each contact pad is 500 x 500  $\mu\text{m}$ . (b) The film morphology and gold droplets after the destruction of the device. The white lines indicate the edges of the contact pad. On the far right, the contact pad can be seen with some damage. Moving toward the left, some  $\text{VO}_2$  appears fractures then there is a region that may or may not still contain  $\text{VO}_2$ . Finally on the far left, condensed droplets can be seen where the edge of the contact pad should be located.

### A.3 The Effect of Edge Defects

The shape and severity of the destruction of VO<sub>2</sub> devices was not consistent. In some cases, the existence or shape of the destruction can be traced back to defects at the edge of the contact pad on one or both sides of the device. In one case, there was a flaw in the gold contact pad near its edge, most likely caused by debris on the wafer during evaporation. The current density along the corners of the flaked area was most likely higher than other areas causing the VO<sub>2</sub> in that region to transition prior to other regions. When this occurred, the current spread through the VO<sub>2</sub> much like lightening and caused permanent damage to the VO<sub>2</sub> film (Figure A.6).

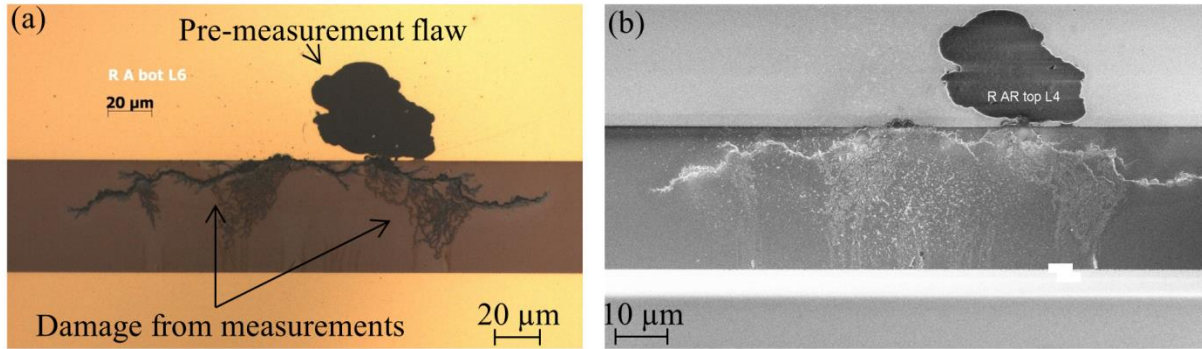


Figure A.6: Destruction caused by a fabrication flaw, in this case a chipped off piece of gold on the edge of the contact pad.

### A.4 VO<sub>2</sub> Device Training

Early in this research, it was observed that the first measurement made on device was very different from the subsequent measurements. This virgin curve transitioned at a lower current value (critical current) and had a much higher voltage directly prior to transitioning (Figure A.7). These results indicated that VO<sub>2</sub> devices require a training sweep. Until the VO<sub>2</sub> was electrically transitioned for the first time, the measurements were repeatable indicating that there is a permanent change to the VO<sub>2</sub> during the first transition that affects the IV characteristics. A need for training has also been observed by other researchers [3]. This may be

related to permanent changes to the  $\text{VO}_2$  film as a result of local heating; however, this hypothesis was not tested.

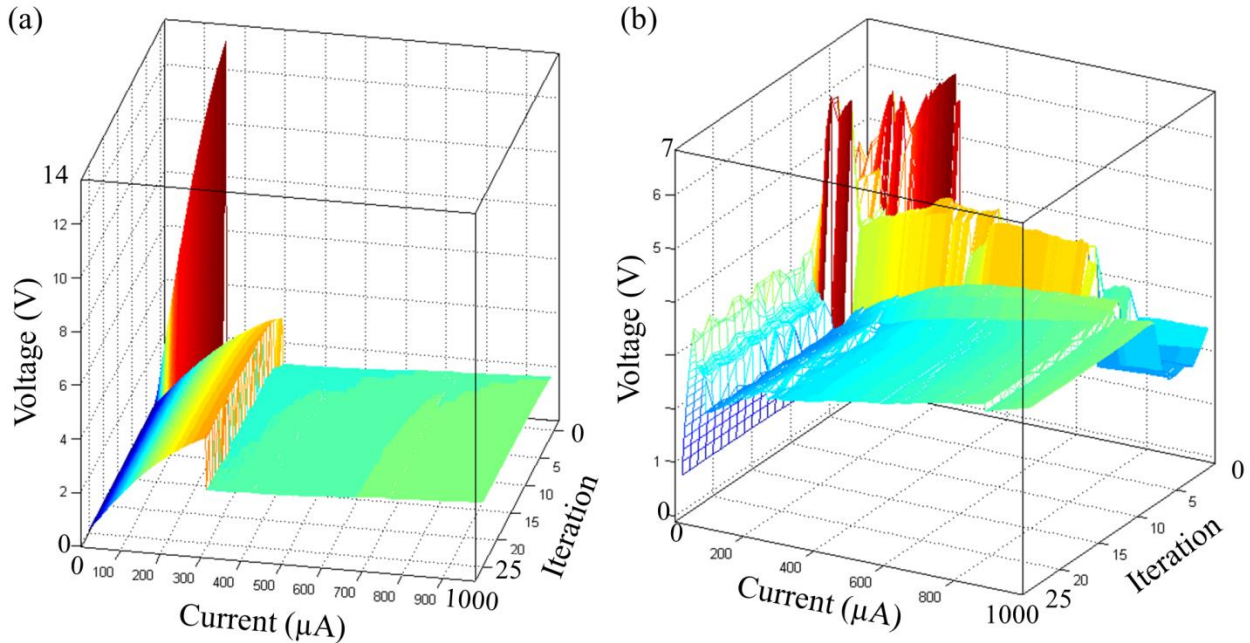


Figure A.7: Training a  $\text{VO}_2$  device. A device was swept 25 times in a row without lifting the probes or changing the sweep parameters using (a) a pulsed linear stair current source and (b) a continuous linear stair current source. It can be seen that both devices changed after the first sweep. In the case of (a), it only took one sweep to train the device while (b) took about 10 sweeps and was still inconsistent after 25 sweeps.

## A.5 Conclusions

The sweep parameters when making  $\text{VO}_2$  measurements need to be carefully monitored. Continuing to increase the bias well into the metallic state can cause the  $\text{VO}_2$  to be destroyed. Additionally, defects at the edge of the  $\text{VO}_2$  to gold interface (such as the edge of the contact pads or the end of a signal line) can cause the fields to be concentrated and the  $\text{VO}_2$  to be damaged at that location. A 1.2 k $\Omega$  resistor along the high current line in four-point measurements is highly recommended to help protect your device when the voltage suddenly increases as a result of the  $\text{VO}_2$  IMT.

- [1] W. Yin, K. G. West, J. W. Lu, Y. Pei, S. A. Wolf, P. Reinke, and Y. Sun, "The metal-insulator transition in vanadium dioxide: a view at bulk and surface contributions for thin films and the effect of annealing," *Journal of Applied Physics*, vol. 105, no. 11, p. 114322, 2009.
- [2] K. Okimura, N. Ezreena, Y. Sasakawa, and J. Sakai, "Electric-field-induced multistep resistance switching in planar VO<sub>2</sub>/c-Al<sub>2</sub>O<sub>3</sub> structure," *Japanese Journal of Applied Physics*, vol. 48, no. 6, p. 065003, 2009.
- [3] J. Kim, C. Ko, A. Frenzel, S. Ramanathan, and J. E. Hoffman, "Nanoscale imaging and control of resistance switching in VO<sub>2</sub> at room temperature," *Applied Physics Letters*, vol. 96, no. 21, p. 213106, 2010.

## Appendix B: MatLab Code for Calculating Contact Resistance

The MatLab program and functions used to calculate the contact resistance are presented. The description for each section of code is shown in the comments, which are denoted by “%”. There are two variables necessary for this program. The first variable is a structure containing the current-voltage data for each separation length of the contact resistance device. Each field in the structure corresponds to a single length labeled “*L1*”, “*L2*”, etc. The measurement data for a given length is contained in that field where column one is the current and column two is the voltage. The second variable, *gaplengths*, is an array of the separation lengths where row one is the length of “*L1*”, row two is “*L2*”, etc. If the data for a given length is not available, the cell in the *gaplengths* variable corresponding to that gap number will be ignored as long as the data is not contained in the device data structure. For example, if the 3<sup>rd</sup> gap was bad (ie – measured as an open circuit), *devdata.L3* should not exist but its length should still be in the *gaplengths* variable (or the 3<sup>rd</sup> cell should be empty).

### B.1 Main program: “Iterative\_x.m”

```
%% Script description

% Find the contact resistance, sub- and inter- contact pad sheet resistance,
% transfer length, and specific contact resistance at multiple power
% densities.
%
% This script sweeps through a variety of effective x lengths used for
% calculating power densities to find the value that yields the smallest
% range of y-intercept.
%
% Resistance values for each length are pulled from the raw data using
% sweep of constant power densities where PD = IV/(hw(L+2x)).
%
% The RL data for each PD is least squares fit with a line. The y-intercept
% (b) is found for each PD.
%
% The mean and standard deviation is calculated for that set of lines.
% The mean(b) and stdev(b) values are saved as a function of length x.
% The x value with the smallest stdev is chosen as "best".
%
```



```

% The "best" length x is then used to regrab the RL data and calculated
% the contact resistance, sub- and inter- contact pad sheet resistance,
% transfer length, and specific contact resistance for each power.
% The results are plotted.
%
% All distance units are microns

%% Script setup
% Items that you change (like you would for a function input)
devname = 'RARbot'; %device name (for titling)

devdata = eval(devname); % get data for variable with the device name

gaplength = gaplengths; %separation lengths
h = 0.084; %VO2 thickness
numsteps = 100; %number of steps (# power densities to use)

overlap = 50; %maximum effective x to try

%% widths from variablenames if applicable
w_ind = devname(end-2);
switch w_ind
    case 'S'
        w = widths(1);
    case 'M'
        w=widths(2);
    case 'L'
        w=widths(3);
    otherwise
        w = 500; %default width
        display ('width not known, set to 500um')
end
clear w_ind

fldnms = char(fieldnames(devdata));
gaps = gaplength(str2num(fldnms(:,end))); %#ok<ST2NM>

%% Sweep range
x = 0:overlap/numsteps:overlap;

%% Calculate the mean and stdev for each y-intercept
% Preallocate variables for speed
meanb = zeros(size(x));
maxb = zeros(size(x));
minb = zeros(size(x));
rangeb = zeros(size(x));

for ix = 1:length(x)

    %maximum possible PD for a given x for each L
    Pmx = zeros(1,length(fldnms));
    Pmn = zeros(1,length(fldnms));
    Psz = zeros(1,length(fldnms));
    for iPmax = 1:length(fldnms)

```

```

tmp = char(fldnms);
L=gaplength(str2double(tmp(iPmax,end)));

eval(['I = devdata.' char(fldnms(iPmax,:)) '(:,1);']);
eval(['V = devdata.' char(fldnms(iPmax,:)) '(:,2);']);

Pmx(iPmax) = max((10^6*V.*I)/(h*w*L+2*h*w*x(ix)));
Pmn(iPmax) = min((10^6*V.*I)/(h*w*L+2*h*w*x(ix)));
Psz(iPmax) = size(I,1); %gets # of datapoints

clear I V tmp L;
end %iPmax

Pmax = min(Pmx); %selects the highest power that is in all L sweeps
Pmin = max(Pmn); %selects the lowest power that is in all L sweeps
Psize = min(Psz);

Pstep = (Pmax-Pmin)/(Psize*0.5); % # powerpoints = 50% # datapoints
powerarray = Pmin+Pstep:Pstep:Pmax-Pstep;

clear Pmx Pmn Psz iPmax;

%Get the RL data for a specific power density
RLdata = RLfrompower(devdata, gaps, x(ix), powerarray, w, h);
[~, b] = findmb(RLdata);

% Save the mean and range in an array where each array slot corresponds
% to a single x value
meanb(ix) = mean(b);
rangeb(ix) = max(b)-min(b);
maxb(ix) = max(b);
minb(ix) = min(b);

%save b if the new range is smaller
if (max(b)-min(b)) <= min(rangeb(1:ix))
    RLdata_best = RLdata;
    Bestx = x(ix);
    Bestrange = max(b)-min(b);
    Bestb = mean(b);
    Bestpowerarray = powerarray;
end %if

clear RLdata b;
end %ix

RLname = sprintf('%s%s', devname, 'RLdata_iterx');
eval([RLname ' = RLdata_best;']);

clear ix RLname

%% Calculate values for each power
values = RLcalcs(RLdata_best, w, Bestx);

```



```

n = size(values,2);

% In array form
results.Rc = cell2mat(values(4,2:n));
results.Rsh = cell2mat(values(5,2:n));
results.Rsk = cell2mat(values(6,2:n));
results.rc = cell2mat(values(7,2:n));
results.PD = Bestpowerarray;
results.bestx = Bestx;
results.bestb = Bestb;
results.beststdev = Bestrange;

resname = sprintf('%s%s', devname, 'results_iterx');
eval([resname ' = results;']);

% In mean/std form
final.bestx = Bestx;
final.bestrangle = Bestrange;
final.Rc = mean(results.Rc);
final.RcStd = std(results.Rc);
final.rcdiff = mean(results.rc);
final.rcStd = std(results.rc);
final.Rsk = mean(results.Rsk);
final.RskStd = std(results.Rsk);
final.Rsh = mean(results.Rsh);
final.rcsame = (final.Rsh)*w^2; %for Rsk = Rsh

clear resname values n

%% Plot raw data
%plots power density on the IV data
PDonIV(RLdata_best, devname, devdata, gaps);

%% Plot the x vs mean, max, and min y-intercepts w/ best x marked

bestxplot = figure;
set(bestxplot, 'name', strcat('meanbVSx', devname), 'numbertitle', 'off');

hold all;

X = [transpose(x), fliplr(transpose(x))];
Y=[minb, fliplr(maxb)];
fill(X,Y, 'y')
plot(x, meanb, 'k', x, maxb, 'k', x, minb, 'k')
plot(bestx, bestb, 'dr')

set(gca, 'xlim', [0 overlap]);

xlabel('Effective x (\mu)');
ylabel('Y-intercept [ \Omega]');

```

```

%% Results
%results
display(final);

finname = sprintf('%s%s', devname, 'meanvals_iterx');
eval([finname ' = final;']);

clear finname

%% Cleanup
clear BestPmax Bestb Bestpower Beststd BestA
clear Rsh_PDcoeff Rshfitvals bestxplot
clear power r2 stdb x
clear final results
clear Re d devdata devname fldnms gaps gaplength h w
clear A area numsteps overlap
clear RLdata_best
clear iPmin powerarray
clear Pstep Psize Powerplotstep Pmin Pmax
clear Bestpowerarray errplot Bestx errfill

```

## B.2 Function: “RLfromPower.m”

```

%% Function description
% This function uses a constant power density ( $PD = IV / (h(w*L+2A))$ ) to
% find the resistance value for each length

% Inputs
% devdata = the datafile name
% gaplength = the gaplengths for that device
% power = power density to use for selecting data in  $\mu W/\mu m^3$ 
% w = width of the contact pad
% h = thickness of the VO2

% Output
% RLdata is a structure where each field corresponds to a power density

function[RLdata] = RLfrompower(devdata, gaplength, x, power, w, h)
%#ok<STOUT>

%% Setup

lengthskey = char(fieldnames(devdata));
lengthskey = str2num(lengthskey(:,end)); %#ok<ST2NM>

%R(length(lengthskey))=zeros;
%% Scroll through powers
for p = 1:length(power)

    % Find the resistance when the power is closest to the desired value

```

```

for i = 1:length(lengthskey)

    eval(['I = devdata.L' int2str(lengthskey(i)) '(:,1);']);
    eval(['V = devdata.L' int2str(lengthskey(i)) '(:,2);']);

    L(i) = gaplength(i);
    P = (10^6*V.*I)/(h*w*L(i)+2*h*w*x);

    %Find index number for the power value closest to input value
    [~, idx] = min(abs(P-power(p)));

    Icare(i) = I(idx);
    Vcare(i) = V(idx);
    R(i)=V(idx)/I(idx);

    clear I V
end

    eval(['RLdata.P' int2str(power(p)*1000) 'nW = transpose([L; R; Icare;
Vcare]);']);

    clear P L R idx i flag
end

end %end function

```

### B.3 Function: “RLcalcs.m”

```

%% Calculates Rc, Rsh, Rsk, Lt, and rc based on Reeves and Harrison, 1982.

% Inputs:
% RLdata - the device data stored in a structure where each field is one
% set of data
% w & d - width and length of contact pad in um

% Output:
% values - a matrix of the calculated values where each column corresponds
% to a single field in RLdata

%% Start code
function[values] = RLcalcs(RLdata, w, d)

structurekey = fieldnames(RLdata);

values(:,1) = {'Fieldname'; 'm (Ohms/um)'; 'b (um)';...
'R_c (Ohms)'; 'R_sh (Ohms/sq)'; 'R_sk (Ohms/sq)'; 'r_c (um*cm^2)'};

```

```

for idx = 1:length(structurekey)

    eval(['RL = RLdata.' char(structurekey(idx)) ';'']);
    L=RL(:,1); %#ok<NODEF>
    R=RL(:,2);

    fitcoeff = polyfit(L,R,1);

    %Calculate contact resistance, etc
    m=fitcoeff(1,1); %slope
    b=fitcoeff(1,2); %intercept

    %contact resistance
    R_c=b/2; %[Ohms]

    %Sheet resistance between pads
    R_sh = m * w; %ohms/sq

    %Transfer length
    %L_t = d/(acosh(R_c/Re)); %Distance from edge of pad where current
    becomes 1/e.

    %Sheet resistance under pad
    R_sk = b*w/(2*d);

    %Specific contact resistance [ohms-cm^2 by convention]
    r_c = R_sk * (d*10^-4) ^ 2; %ohms-cm^2

    format shortEng;

    %Save calculations in a variable to write to excel
    values(:,idx+1) = {char(structurekey(idx)); m; b; R_c; R_sh; R_sk; r_c};

end

```

## B.4 Function: “RLplot.m”

```

%% This function plots RLdata where L is column 1 and R is column 2

%% Inputs
% RLdata - the device data stored in a structure where each field is one
% set of data
% devname - device name used for the titles etc

%% Code start
function[] = RLplot(RLdata, devname,varargin)

```

```

%% Start script

switch nargin
    case 2
        sk = fieldnames(RLdata);
        linestyleord(1:length(sk),1) = cellstr('-');
    case 3
        nplot = str2double(varargin(1));
        sk = fieldnames(RLdata);
        step = floor(length(sk)/nplot);

        %take every n'th dataset from the RL structure
        for n=1:nplot
            eval(['RLdatatmp.' char(sk(step*n))...
                '= RLdata.' char(sk(step*n)) ';' ]);
        end

        clear RLdata;
        RLdata = RLdatatmp; %save the smaller dataset to original variable
        clear RLdatatmp sk;
        sk = fieldnames(RLdata); %update fieldnames

        for lso = 1:length(sk)
            if rem(lso,4) == 1
                linestyleord(lso,1) = cellstr('-');
            elseif rem(lso,4) == 2
                linestyleord(lso,1) = cellstr('--');
            elseif rem(lso,4) == 3
                linestyleord(lso,1) = cellstr(':');
            elseif rem(lso,4) == 0
                linestyleord(lso,1) = cellstr('-.');
            end
        end

        otherwise
            error('Invalid number of inputs');
end %end switch

%Color order
numpowers = length(sk);
switch numpowers
    case 1
        clrmap = [0 0 0];
    case 2
        clrmap = [0 0 1; 1 0 0];
    case 3
        clrmap = [0 0 1; 1 0 0; 0 1 0];
    otherwise
        clrmap = colormap(varycolor(numpowers)); %sets line color order
end

```

```

%repeat each color for data + fit
cmap = zeros(2*numpowers,3);
for iCmap = 1:numpowers

    cmap(2*iCmap-1,:) = clrcmap(iCmap,:);
    cmap(2*iCmap,:) = clrcmap(iCmap,:);

end

%Sets generic axis properties
figure('name',strcat('RLplot',devname),'numbertitle','off');
axes('ColorOrder',cmap);
%axes('FontSize',12,'FontName','Times New Roman','ColorOrder',cmap);
%axes('FontSize',20,'FontName','Times New Roman'); %If use default colors
grid on;
hold all;
box on;

%Makes a title from a plot name
titlename = sprintf('%s %s', devname, 'RL');
%title(titlename, 'FontSize', 24, 'FontName', 'Times New Roman');

%Gets the data from the structure field
lgdarr = zeros(length(sk),1); %array for the legend
for i = 1:length(sk)

    eval(['RL = RLdata.' char(sk(i)) ';' ]);
    L=RL(:,1); %ok<NODEF>
    R=RL(:,2)/1000;

    % Least squared linear fit to data
    x=0:5:25;
    fitcoeff = polyfit(L,R,1);
    fiteqn = polyval(fitcoeff,x);

    %Plot data
    plot(L,R,'x',x,fiteqn,char(linestyleord(i)),'LineWidth',1.5);

    %Write the string that will become the legend
    tmplgd = char(sk(i));
    lgdarr(i) = str2double(tmplgd(2:end-2))/1000;

    legendstr(2*i-1,1) = cellstr(sprintf('%0.3f %s', lgdarr(i),
'\muW/\mum^3')); %ok<AGROW>
    legendstr(2*i,1) = cellstr(sprintf('%s %0.3f %s %0.3f', 'y =', ...
fitcoeff(1,1), 'x +', fitcoeff(1,2))); %ok<AGROW>

end

% Limits, labels, and title
xlim([0 25]);
ylim([0 6]);
set(gca,'xtick',0:5:25,'ytick',0:1:6);

```

```

xlabel('Length (\mu)');
ylabel('Resistance (k\Omega)');

%% to legend or not to legend?
if numpowers <= 3
    legend(legendstr, 'Location', 'NorthWest');

elseif (3 < numpowers) && (numpowers < 10)
    legend(legendstr, 'Location', 'EastOutside');

else
    %if there are over 10 lines, a colorbar is used for the legend
    cbar = [lgdarr(1), lgdarr(ceil(1*(length(lgdarr))/4)), ...
            lgdarr(ceil(2*(length(lgdarr))/4)), ...
            lgdarr(ceil(3*(length(lgdarr))/4)), lgdarr(length(lgdarr))];

    caxis([lgdarr(1) lgdarr(i)]); %sets the range of values the colors are
mapped onto

    colormap(cmap);
    clrbar = colorbar('Ylim', [lgdarr(1) lgdarr(i)], ...
        'YLimMode', 'manual', ...
        'YTick', cbar, 'YTickLabel', cbar);

    xlabel(clrbar, '\muW/\mu^3');
end

%% end function
end

```

## Appendix C: Fabrication Recipe

This appendix provides a sample fabrication recipe for non-passivated VO<sub>2</sub> devices. It includes some changes designed to minimize exposure to suspect chemicals and processes (liftoff, March O<sub>2</sub> plasma clean). The same recipe is used for the contact resistance structures and the terahertz switches.

VO<sub>2</sub> RF mask processing sheet –

Etch VO<sub>2</sub> before metal lithography

VO<sub>2</sub> wafer ID (from Lin):

VO<sub>2</sub> thickness:

VO<sub>2</sub> wafer ID (from me):

- 1) Inspect film
- 2) Spin clean – Isopropyl alcohol, d-lim, methanol, 20s each, no swab
- 3) VO<sub>2</sub> width lithography – MJB4
  - a) HMDS – 5 – 8 minutes
  - b) Spin: AZ4110 30 sec, 4krpm
  - c) Bake: 110-120 °C 1 min
  - d) Align
  - e) Expose: 30 sec CP (275W) on MJB4 (50s on EVG)
  - f) Develop: AZ400K:H<sub>2</sub>O 1:4 ~ 72 sec (\_\_\_\_\_ sec)
- 4) Lithography height: \_\_\_\_\_nm
- 5) Etch VO<sub>2</sub> - Trion
  - a) File name: “Amber”
  - b) P = 30 mTorr
  - c) ICP = 50 W
  - d) RIE = 20 W
  - e) SF6 = 4 sccm



- f) Ar = 40 sccm
  - g) O<sub>2</sub> = 4 sccm
  - h) DC = -5
  - i) t = 3 minutes
- 6) Lithography height: \_\_\_\_\_nm
- 7) Remove resist
- a) 10 min March O<sub>2</sub> Plasma @ 120 W to remove baked on resist
  - b) Acetone spin clean with swab
  - c) Methanol spin clean to remove film
  - d) DI water rinse, N<sub>2</sub> dry
- 8) Metal lithography - MJB4
- a) HMDS – 5 – 8 minutes
  - b) Spin: nLOF2020, 30 sec, 4krpm
  - c) Bake 120 °C, 1 minute
  - d) Align
  - e) Expose: 20 sec, MJB4. Settings: CP 275W
  - f) Post-bake: 110 °C 1 min
  - g) Develop: 300MIF ~ \_\_\_\_\_ sec (1min)
- 9) Evaporate metals
- a) Ti: 100 Å @ 1 Å/s
  - b) Au: 1500 Å @ 3 Å/s
- 10) Liftoff – NMP @ 80 °C
- a) 20 minutes in NMP
  - b) Swab in ethylene-glycol
  - c) 5 minutes in NMP
  - d) Swab in e-glycol
  - e) Rinse in DI wafer
- 11) Inspect with microscope
- 12) Image and SEM